FINAL REPORT

EMI Modeling for UXO Detection and Discrimination Underwater

SERDP Project MR-1632

DECEMBER 2011

Dr. Fridon Shubitidze
Thayer School of Engineering, Dartmouth College

SERDP
DOD ▪ EPA ▪ DOE

Table of contents

List of figures

List of acronyms

2D	Two-Dimensional
3D	Three-Dimensional
ASWF	Angular spheroidal wave function
BOR	Body of Revolution
BUD	Berkeley UXO Discriminator
CRREL	Cold Regions Research and Engineering Laboratory
DE	Differential evolution
DoD	United States Department of Defense
DOE	United States Department of Energy
EM	Electromagnetic
EM-63	A time-domain EMI sensor developed by Geonics, Inc.
EMI	Electromagnetic induction frequency regime
EMSG	Electromagnetic Sensing Group at Dartmouth College
ERDC	Engineer Research and Development Center
ESTCP	Environmental Security Technology Certification Program
FD	Frequency Domain; Finite differences
GEM-3	A frequency-domain EMI sensor developed by Geophex, Inc.
GEM-3D+	A vector version of the GEM-3
GSEA	Generalized standardized excitation approach
HAP	A method to estimate the location and orientation of a target employing the magnetic field H, the vector potential A, and the magnetic scalar potential ψ (Psi)
HEAT	High Explosive Anti-Tank
JD	Joint diagonalization
LS	Least-squares method
MAS	Method of Auxiliary Sources
MAS-TSA	Method of Auxiliary Sources, supplemented with the Thin Skin Approximation for high frequencies
MM	MetalMapper or Munitions Management
MPV	Man Portable Vector time-domain sensor, developed by CRREL and G&G Sciences, Inc.
MQS	Magnetoquasistatic approximation
MR	Munitions response
MRSON	Munitions response statement of need
MSR	Multistatic response matrix
NRL	Naval Research Laboratory
NSMC	Normalized surface magnetic charge model (forerunner of NSMS)
NSMS	Normalized surface magnetic source model
ONVMS	Orthonormalized volume magnetic source model
PCA	Principal component analysis
PSTD	Pseudospectral time-domain method

ROC	Receiver operating characteristic
RSWF	Radial spheroidal wave function
Rx	Receiver
SEA	Standardized excitation approach
SEED	SERDP Exploratory Development Program
SERDP	Strategic Environmental Research and Development Program
SIBC	Surface impedance boundary condition
SNR	Signal-to-noise ratio
SON	Statement of need
SPIE	The International Society for Optical Engineering
SVD	Singular value decomposition
SWF	Spheroidal wave function
TD	Time domain
TEMTADS	Time-domain Electro-Magnetic Towed Array Detection System
TOI	Target of interest
TSA	Thin skin approximation
Tx	Transmitter
UW	Underwater
USACE	U.S. Army Corps of Engineers
UXO	Unexploded ordnance
VSWF	Vector spheroidal wave function

Acknowledgments

The Principal Investigator, Dr. Fridon Shubitidze of Dartmouth College, conceived, implemented, and tested most of the approaches presented in this report. He developed the MAS code for UW targets, incorporated the surface impedance boundary condition, and implemented the Debye relation model to understand UW EMI phenomena.

Dr. Juan Pablo Fernández of Dartmouth College extended the analytic solution for the EMI response of a sphere to incorporate seawater-like conducting embedding media, nonuniform excitations, and multi-layered objects. He provided a thorough analysis of the physics of EMI scattering off spherical targets.

Dr. Alex Bijamov of Dartmouth College implemented the three-dimensional MAS code for conducting rough surfaces and conducted EMI field scattering studies for various rough surfaces at different frequencies.

Dr. Benjamin Barrowes of USA ERDC-CRREL adapted an analytical model of EMI scattering from UW spheroidal targets using a vector wave approach.

Funding for this project was provided by the Strategic Environmental Research and Development Program Office. We wish to express our sincere appreciation to Dr. Jeffrey Marqusee, Dr. Anne Andrews, Dr. Herb Nelson, and staff of the SERDP Office for providing support and funding for this project.

Abstract

The research described in this report was conducted in fulfillment of Project MR-1632, "EMI modeling for UXO detection and discrimination underwater," submitted to the Strategic Environmental Research and Development Program (SERDP) in response to the Munitions Management Statement of Need SERDP SON # 08-02 "Detection and Disposal of Underwater Military Munitions."

The primary objectives of Project MM-1632 were to 1) extend EMI forward models in an effort to understand how marine environments affect the performance of EMI sensors, 2) study EMI phenomena from highly conducting and permeable metallic objects in underwater environments, and 3) investigate the impact of the electromagnetic parameters of water (e.g., its conductivity or conductivity gradient) on the ability to discriminate UXO from non-UXO items. The Method of Auxiliary Sources was adapted for scenarios involving metallic objects placed in heterogeneous conducting media such as seawater. The contribution of the electric field was computed accurately using a surface impedance boundary condition that relates the tangential components of the electric and magnetic fields at frequencies such that the skin depth is small. Numerical experiments were conducted for both homogeneous and heterogeneous UXO-like objects subjected to frequency- or time-domain illumination. The near and far EMI fields and induced eddy-current distributions were calculated to illustrate the underlying physics of EMI scattering phenomena in aqueous environments. The coupling effects between an object and its surrounding conductive medium were analyzed and demonstrated at high frequencies (or early times for time-domain sensors). We investigated the performance in UW environments of current frequency- and time-domain state-of-the-art EMI sensors. We analyzed the EMI scattering due to highly conducting and permeable heterogeneous objects placed underwater and interrogated by the electromagnetic fields of the EM-63 and TEMTADS sensors. We found that marine environments have negligible effects on the performance of next-generation EMI sensors, which operate from 100 μs (10 kHz) to 25 ms (40 Hz). Similar effects were observed for inversion schemes like the generalized standardized excitation approach, the orthonormalized volume magnetic source model, joint diagonalization data preprocessing, etc. We showed that currently available EMI sensors and signal-processing approaches could be used to detect and discriminate submerged metallic targets. We studied ultrawideband EMI field scattering from heterogeneous conducting and permeable rough surfaces; these investigations were carried out using the MAS supplemented by a surface impedance boundary condition. We modeled current EMI sensors and used the models to illuminate objects placed in free space and conducting host media at various locations and orientations. Our studies demonstrated that rough conducting surfaces have a negligible effect on the EMI responses of highly conducting and permeable metallic objects at low frequencies (<15 kHz); at high frequencies, however, we found that the effect is not negligible. We employed the Debye dielectric relaxation model for salt water and implemented it within our MAS-based numerical code to investigate how dielectric relaxation and EMI response vary as functions of temperature and salinity. Closed-form solutions were developed for spherical and spheroidal geometries. All of our studies show that marine environments have a negligible effect on the EMI response of an object that can be detected by current EMI sensors.

1 Introduction

There are approximately one million acres of underwater lands at Department of Defense (DoD) and Department of Energy (DOE) sites that are highly contaminated with unexploded ordnance (UXO). Detecting and disposing of underwater military munitions is more expensive than excavating the same targets on land. Therefore, innovative detection and discrimination systems are required that can reliably discriminate between hazardous UXO and innocuous items with false-alarm rates as low as possible. Recently, electromagnetic induction (EMI) sensing has been considered as a potential candidate for underwater detection. In order to explore the potential of various EMI sensing technologies for underwater detection and discrimination, with the aim of achieving a high (~100%) probability of detection and distinguishing UXO from non-UXO items accurately and reliably, it is necessary first to investigate in detail the underlying physics of electromagnetic (EM) scattering phenomena in underwater environments and to determine the noise level due to the marine environment in underwater UXO discrimination studies.

Marine environments tend to exhibit several electrically different layers ("pancakes") because of salt intrusions, haline fronts in shallow areas like river estuaries, and bottom layers. Salt intrusions and fingers as well as haline fronts are typical of the coastal ocean and result in high salinity gradients. The EMI field thus behaves in a marine environment much as it does in a layered medium. Strong vertical gradients of salinity may increase the false-alarm ratio and reduce the effectiveness of the detection and discrimination process. Consequently, seafloor haline structures must be modeled accurately using realistic values of temperature and salinity, and their effects suppressed during both wide-area assessment and detailed surveys. This can be achieved by using an accurate 3D numerical code, such as the combined method of auxiliary sources/surface impedance boundary condition approximation (MAS/SIBC), the pseudospectral time-domain technique, finite element methods or other approaches.

The primary goals of Project MM-1632 were (1) to extend EMI forward models in an effort to understand how sea water affects the performance of EMI sensors, (2) to study EMI phenomena from highly conducting and permeable metallic objects in underwater environments, and (3) to investigate what impact the electromagnetic parameters of water (*e.g.*, its conductivity or conductivity gradient) have on the ability to discriminate UXO from non-UXO items. Specifically, the objectives of the proposed work were as follows:

1. Extend full EMI forward models, such as the Method of Auxiliary Sources (MAS), to understand how marine environments change EMI sensor performance and associated processing approaches for detecting highly conducting and permeable metallic objects underwater.
2. Investigate the underlying physics of EMI scattering phenomena for metallic objects placed inside a conducting medium. Assess under what conditions (i.e., at what conductivity or conductivity gradient) the noise due to the underwater environment becomes non-negligible compared to the response of the object.
3. Assess how the EMI signals from targets are distorted by marine environments composed of several electrically conductive layers, by haline fronts in shallow areas, by bottom layers, and by sensor motion and fluctuations. Also investigate the impact of these distortions on the ability of discrimination algorithms to distinguish UXO from non-UXO items.
4. Evaluate the conditions under which our modified forward models are useful for discrimination in underwater environments. These modified forward models include the simple dipole model, the Generalized Standardized Excitation Approach (GSEA), and the Normalized Surface Magnetic Source (NSMS) model.

This report is structured as follows:

Chapter 2 starts by outlining the theoretical basis of the MAS for underwater EMI scattering problems and goes on to describe the mathematical formulation and the numerical implementation of the 3D MAS for rough surfaces, multi-layered objects, and heterogeneous structures placed in vacuum and in a conducting medium. We then outline the surface impedance boundary condition that supplements the MAS for a proper treatment of submerged metallic targets and present a model of the dielectric permittivity of salt water that incorporates its dependence on frequency, temperature and salinity. We finish by describing a simple approach for estimating the location, orientation, and magnetic polarization of an underwater target, extend the generalized standardized excitation approach (GSEA) for underwater environments, and present the model we use to simulate surface of the water.

Chapter 3 validates our numerical code and tests its accuracy by comparing its predictions to analytic and experimental data. We investigate the effects on EMI measurements of a rough water/air interface. We show how both sensors and targets couple to the embedding conducting medium in both frequency and time domains. We show eddy-current distributions and analyze in detail the near field, both electric and magnetic, for rough surfaces, homogeneous targets, and multi-layered structures. We demonstrate how the EMI response of a spheroidal target in an aqueous environment varies as a function of frequency, salinity and temperature using values appropriate for salt water. We wrap up by presenting some inversions starting from EMI data.

Chapter 4 illustrates analytical treatments for spherical and spheroidal targets. Spheres of arbitrary electromagnetic properties embedded in media of finite conductivity are subjected to uniform and dipolar excitation; in particular, we present results for scenarios mimicking monostatic measurements. We also present the solution for two-layer system consisting of sphere surrounded by a nonconducting shell and embedded in seawater. We present the analytic solution for the EMI responses of prolate and oblate spheroids is extended to underwater-like media.

Chapter 5 describes our main conclusions.

2 The Method of Auxiliary Sources for assessing EMI noise due to a marine environment

Modern EMI digital geophysical technologies such as magnetic and time- and frequency-domain sensors [1-6] have been used effectively to characterize potentially harmful subsurface munitions on dry land [1-21]. However, by estimation there may be as many as one million acres of formerly used military underwater land contaminated with hazardous UXO [22-25]. Underwater environments, unlike dry soil, are electrically conducting and heterogeneous. This can significantly affect the performance of established and emerging land-based EMI sensing technologies [22-26], since the electrical conductivity of water is much higher than the conductivity of soil. An object's underwater EM response should be less than its response in dry soil because water absorbs EM energy much faster than dry soil, particularly at frequencies at the high end of the EMI spectrum (>200kHz), where skin effects are significant. Here we employ the generalized MAS/SIBC technique to illustrate these physical phenomena and to understand low-frequency electromagnetic scattering phenomena from highly conducting and permeable metallic objects embedded in marine environments.

The Method of Auxiliary Sources (MAS) is a numerical technique originally designed for solving various electromagnetic radiation and scattering problems. The MAS is robust, easy to implement, and accurate, and has been used to investigate waveguide structures, antennas, scattering, electromagnetic wave propagation in complex media, etc. It has also been employed successfully in the analysis of low-frequency electromagnetic induction scattering phenomena [20, 26-29]. In the MAS, boundary value problems are solved numerically by representing the electromagnetic fields in each domain of the structure under investigation by a finite linear combination of analytical solutions of the relevant field equations, corresponding to sources situated at some distance away from the boundaries of each domain. The "auxiliary sources" producing these analytical solutions are chosen to be elementary dipoles/charges located on fictitious auxiliary surfaces that usually conform to the actual surface(s) of the structure. In practice, at least as the method is realized here, we only require points on the auxiliary and actual surfaces; thus we do not need to the detailed mesh structures required by other methods.

The two auxiliary surfaces are set up inside and outside the scattering object. The fields outside of the structure are considered to originate from a set of auxiliary magnetic charges placed inside the object, while the fields inside the object are taken to arise from a set of auxiliary magnetic dipoles placed outside. The interior and exterior fields thus constructed are required to obey Maxwell's boundary conditions—the continuity of the tangential magnetic field components and the jump condition for the normal magnetic field components—as evaluated at arrays of selected points on the physical surface(s) of the structure. This results in a matrix equation in which the amplitudes of the auxiliary sources are the unknowns to be determined. Once these amplitudes are found the solution is complete: the electromagnetic field—as well as any quantity related to it—can easily be computed throughout the computational space.

The MAS formulation we present here offers a number of advantages. It is no longer necessary to perform integrations to generate an algebraic system. Field singularities at source locations need not be confronted directly, since the auxiliary surfaces containing the sources are separated from the physical surface where the conditions are evaluated. In the simplest MAS formulation no discretization of either the surfaces or volumes of interest is required; all we need to know are the locations of the observation (testing) points on the real surface and the locations of the sources on the auxiliary surfaces. In this report we wish to generalize the MAS solution we have developed elsewhere [26-29] and investigate the wideband EMI response of highly conducting and permeable objects—such as UXO, which typically contain ferrous metal—placed in a conductive background.

EMI scattering responses are usually expressed in terms of the induction number $\chi \sim a/\delta$, where δ [m] is the skin depth and a [m] is a characteristic dimension of the object. It is well established that the

electromagnetic field inside a conductor decays over distances of the order of the skin depth. This reduces the efficiency and accuracy of the MAS at high induction numbers due to singularities that appear in the scattering matrix. To overcome this problem, a combined MAS-thin skin approximation (MAS-TSA) [26, 29] based on the divergence-free Maxwell's equation for the magnetic field was developed and used to solve a variety of EMI problems from the magnetostatic regime up to 1 MHz for land-based UXO detection and discrimination. The TSA assumption, however, is found to break down when targets are placed in conducting media because satisfaction of the divergence-free equation is not sufficient to guarantee that all necessary boundary conditions for electric and magnetic fields are obeyed. We have overcome this difficulty by employing the surface impedance boundary condition (SIBC).The SIBC is based on the fact that the electromagnetic fields and currents within the conductor are confined to a very thin surface layer. The model assumes that the EM field decays exponentially within a metallic object. Within the conductor specific components of the field are related by Maxwell's equations.

The current state of the art advanced EMI methods and next generation EMI sensors to detect land-based UXO involve high-quality discrimination procedures that can reliably distinguish the UXO from other, non-UXO items (clutter). In order to adapt the existing detection and discrimination methods for underwater environments it is necessary first to study in great detail the underlying physics of diffusion and interaction of low frequency electromagnetic waves in marine environments. This knowledge can then be applied to the development of new sensors with improved detection capabilities or extension of current advanced sensors for underwater environment.

In a typical land-based UXO detection scenario the target area is irradiated by a short pulse of low-frequency electromagnetic waves produced by an antenna located above the area of interest. While diffusing through the soil the electromagnetic pulse excites electric current in the metallic objects such as UXO or any other pieces of clutter buried in the ground. After that, when the source excitation has been depleted, the underground objects that have acquired a magnetic dipole moment start serving as new sources of EM fields. These fields are then detected by the sensor array located above the ground and further processed to detect the position, orientation and type of the objects underground. Recent UXO discrimination studies showed that next generation EMI sensors, which consist of multiple transmitters and receivers and do not require local positioning system, provide excellent classification results for land based UXO problem.

In case of underwater UXO detection it might be useful to use similar techniques with the sensor array either above or below the ocean level, though several factors specific to oceanic environments are to be taken into account (Figure 2-1).

First of all, due to the conductive properties of saline environments, the coupling between the conductive object and the surrounding medium has to be taken into account [25]. This coupling is higher at higher frequencies and needs to be studied in detail to be properly accounted for during the UXO detection process. Furthermore, unlike in land-based environments the water surface is in constant motion, with surface waves continually changing the boundary between the air and the conductive water. Additionally, vertical salinity gradients are often present in ocean and sea waters. These gradients change the character of EM wave diffusion and can affect the accuracy of target detection. Finally, the seafloor structure should be taken into account (and its effect suppressed) during UXO detection and discrimination.

This section focuses on: the MAS method developments and implantations for UW high conducting and permeable metallic objects; skin effect approximation in EMI frequency regime; inverse scattering algorithms for estimating UW targets intrinsic and extrinsic parameters; the water surface numerical modeling.

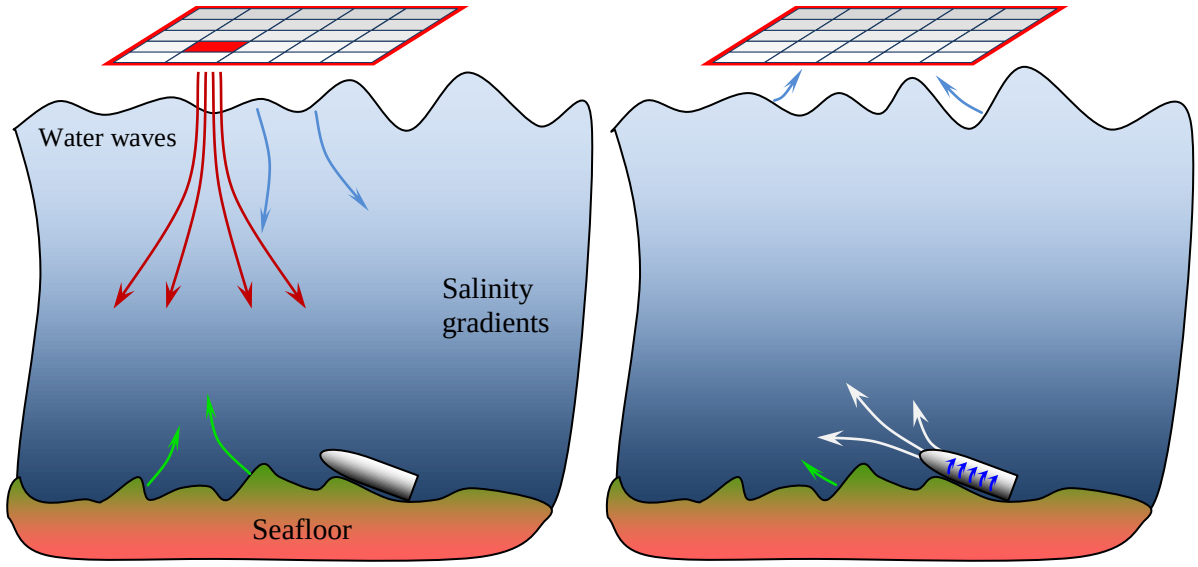

Figure 2-1: Underwater UXO detection scenario.
(Left) A source array sends out a short pulse of low-frequency EM waves. The waves are scattered on the water surface, pass through vertical salinity gradients, scatter on the seabed surface and excite electric currents inside the conducting body of the UXO. (Right) UXO currents emit secondary EM waves, which are detected by the sensor array after passing through the water.

2.1 The 3D MAS

The MAS is a robust, easy to implement, and accurate numerical technique developed for solving a large range of electromagnetic radiation and scattering problems. Previously the MAS has been successfully applied to the investigation of antennas, waveguide structures, complex media, etc. One of the advantages of the MAS over finite-element methods is that it requires no knowledge of the detailed mesh structure of the modeled objects. The boundary-value problems are solved numerically by representing the electromagnetic field in each domain of the structures of interest by means of a finite linear combination of analytical solutions of the relevant field equations. These solutions correspond to the fields created by auxiliary EM field sources, which are usually chosen to be elementary dipoles (or charges) located on fictitious surfaces that conform to the actual boundaries of the structure of interest (Figure 2-2).

For every physical boundary in the problem of interest there are two layers of auxiliary sources: the inner layer of sources, which describes the EM fields outside of this boundary, and the outer layer that describes the fields in the space confined by this boundary. Therefore, at any location $\mathbf{r}$ in space the electric and magnetic fields can be represented as a superposition of fields created by the independent EM field sources and the auxiliary sources:

$$\mathbf{E}(\mathbf{r}) = \mathbf{E}_{\text{source}}(\mathbf{r}) + \sum_n A_n \mathbf{G}_E(\mathbf{r}, \mathbf{r}_n \mid \tau_n) \tag{1}$$

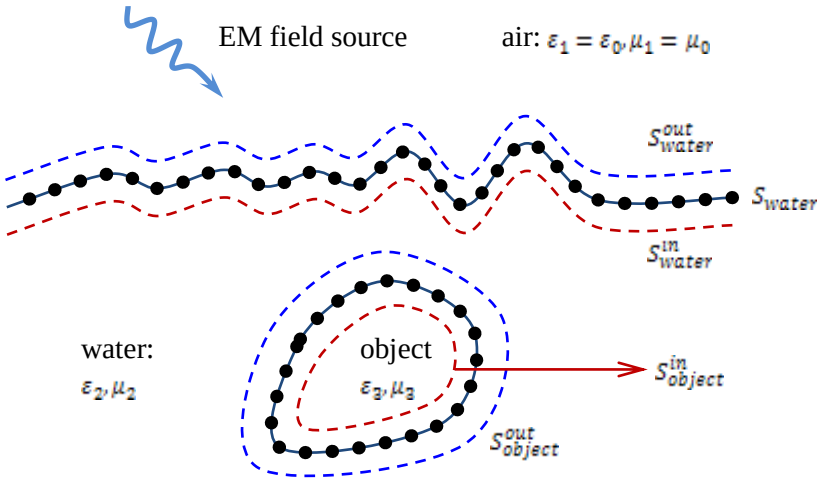

Figure 2-2: The MAS applied to the underwater detection problem.
For every boundary between domains with different physical properties (air-water interface, object surface), a set of auxiliary surfaces is defined which are conformal to it. EM fields in air are created by the external EM field source and the auxiliary sources located at the surface $S_{\text{object}}^{\text{in}}$. *The fields inside water are described as the superposition of fields created by sources located at* $S_{\text{water}}^{\text{out}}$ *and* $S_{\text{object}}^{\text{in}}$. *Finally, the fields inside the object are represented by the auxiliary sources on* $S_{\text{object}}^{\text{out}}$.

$$\mathbf{H}(\mathbf{r}) = \mathbf{H}_{\text{source}}(\mathbf{r}) + \sum_n A_n \mathbf{G}_H(\mathbf{r}, \mathbf{r}_n \mid \tau_n) \tag{2}$$

where $\mathbf{G}_E(\mathbf{r}, \mathbf{r}_n \mid \tau_n)$ and $\mathbf{G}_H(\mathbf{r}, \mathbf{r}_n \mid \tau_n)$ are respectively the electric and magnetic fields created by a unit auxiliary source located at $\mathbf{r}_n$ and oriented along the surface tangent τ_n, while $\{A_n\}$ are the unknown amplitudes of the auxiliary sources. The summation is performed over all auxiliary sources *external* to the current domain. The only constraint placed on the fields is that they satisfy the boundary conditions for Maxwell's equations,

$$\hat{\mathbf{n}} \times \mathbf{E}_{\text{in}} = \hat{\mathbf{n}} \times \mathbf{E}_{\text{out}} \quad \text{and} \quad \hat{\mathbf{n}} \times \mathbf{H}_{\text{in}} = \hat{\mathbf{n}} \times \mathbf{H}_{\text{out}} \tag{3}$$

which can be evaluated at a finite number of collocation points across the object boundaries(with $\hat{\mathbf{n}}$ a unit vector normal to the surface), leading to a system of linear equations binding together the amplitudes of the auxiliary sources $\{A_n\}$. The scattering problem is solved once these amplitudes are found, since any other EM parameter of interest can be determined from the EM fields expressed using (1). This scheme also provides an easy way of monitoring the accuracy of the solution by observing the boundary condition mismatch in the areas between the collocation points.

In this chapter, the 3-dimensional MAS in low-frequency regime (*f*=1 Hz -1 MHz) was used to evaluate the distribution of the magnetic field in space both above and below the ocean surface as a function of its geometry. The auxiliary sources were chosen to be magnetic dipoles, oriented tangentially to the ocean surface, with the electric and magnetic fields given by:

$$\mathbf{G}_E = -\frac{jk_o\eta_o e^{-j(\omega t - \mathbf{k}\cdot\mathbf{r})}}{4\pi\mu_o}\left(\frac{1}{r^2} - \frac{jk}{r}\right)(\mathbf{r} \times \mathbf{p}), \tag{4}$$

$$\mathbf{G}_H = \frac{e^{-j(\omega t - \mathbf{k}\cdot\mathbf{r})}}{4\pi\mu r^3}\left(\left(\frac{3\mathbf{r}(\mathbf{r}\cdot\mathbf{p})}{r^2} - \mathbf{p}\right)(1 - jkr) - k^2\mathbf{r}\times(\mathbf{r}\times\mathbf{p})\right) \quad (5)$$

where the wavenumber $k = k_o\sqrt{\varepsilon_c\mu} = (\omega/c)\sqrt{\varepsilon_c\mu}$ (c being the vacuum speed of light), $\mathbf{r}$ is the radius-vector from the source to the observation point, and $\mathbf{p}$ is the complex amplitude and orientation vector of the dipole, and permeability $\mu=\mu_o\mu_r$. The complex dielectric constant for the conducting marine environment can be expressed as $\varepsilon_c = \varepsilon + j\sigma/\omega$; and $\varepsilon = \varepsilon_0\varepsilon_r$ where $\omega = 2\pi f$ is the angular frequency. Assuming the saline water to be a good conductor in the selected frequency regime ($\sigma = 4$ S/m), the real part $\varepsilon_0\varepsilon_r$ of dielectric constant can be ignored since $\sigma/\omega >> \varepsilon_r\varepsilon_0$. The relative magnetic permeability was assumed to be unity: $\mu_r = 1$.

2.2 MAS for multi-layer objects

Here we summarize the formulation of the MAS for underwater environments so as to provide an understanding of the new implementations described in the next section. We assume that a conducting, possibly permeable, and possibly hollow metallic object is placed in a transmitted time-harmonic primary magnetic field $\mathbf{H}^{pr}(\mathbf{r})$ (A/m). (In all expressions below the harmonic time dependence $e^{j\omega t}$ is assumed and its expression suppressed). The basic configuration is illustrated in Figure 2-3.

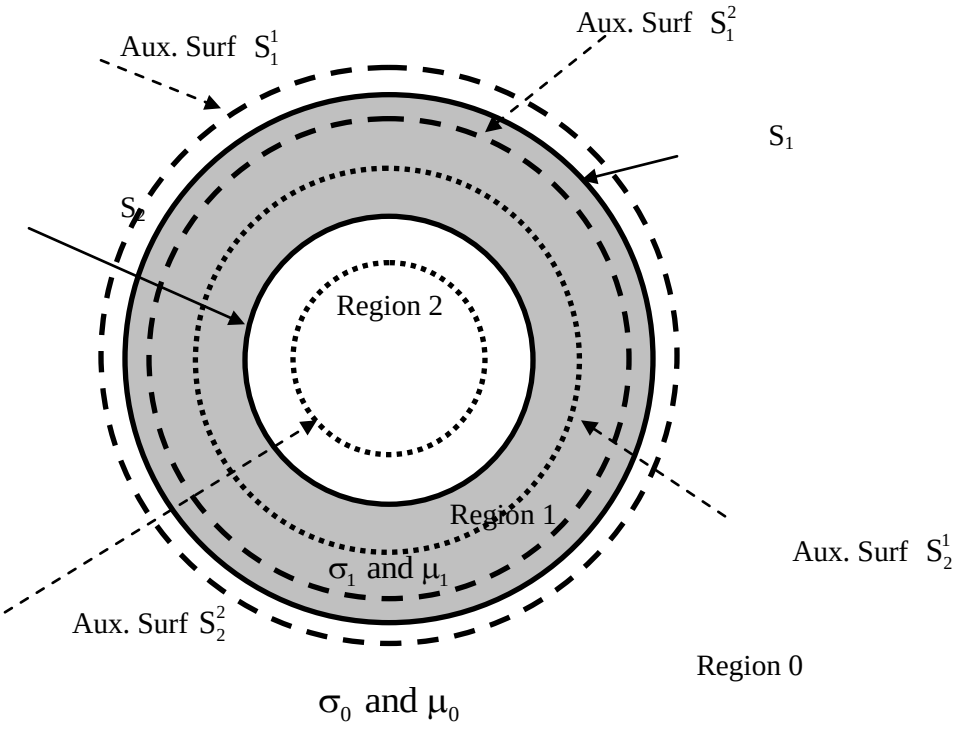

Figure 2-3: MAS diagram for a layered scattering object.
Each i^{th} region is surrounded by a real surface S_i, which in turn is surrounded by the auxiliary surface S_i^1. Interior to S_i is the auxiliary surface S_i^2.

In the external zeroth region (V_0), the complete field consists of $\mathbf{H}^{pr}$ plus a scattered field $\mathbf{H}^{sc}$ (A/m). Forced by the primary field, electromagnetic activity penetrates the object to some degree and induces electric currents inside it. The induced currents and, in the case of permeable materials, molecular polarization produce a scattered ("secondary") field outside the object. Our problem is to determine the

secondary magnetic field. It is well established that, in the materials we consider in the EMI frequency band, displacement currents $\partial \mathbf{D}/\partial t$ are negligible in comparison to conduction currents, where **D** is the electric displacement (Coulombs/m^2). In this sense the fields are magnetoquasistatic (MQS). The electromagnetic field satisfies the vector Helmholtz equation,

$$(\nabla^2 + k^2)\mathbf{H} = 0\,, \tag{6}$$

and can be expressed in terms of vector source intensity **P** ($\mathrm{A}\cdot\mathrm{sec}/\mathrm{m}^2$) distributed over the auxiliary surfaces.

$$\mathbf{H}(\mathbf{r}) = (k^2 + \nabla\nabla\cdot)\int_{S_a} \frac{\mathbf{P}(\mathbf{r}')e^{-jkR}}{4\pi\mu R}\,ds', \qquad S_a = S_1^2 + S_2^1, \quad \mathbf{r}' \in S_a\,, \ \mathbf{r} \in V_1\ . \tag{7}$$

Note that the differentiations in (6) and (7) are performed relative to the observation point coordinate **r**. The source distribution **P** consists of magnetic surface current elements, located *outside* Region 1, taken to be tangential to the surfaces on which they lie. Thus only two independent components of **P** are to be determined. Also, as previously noted, continuous sheets of current may offer some computational advantages and are used where indicated below. However, in the formulation presented in this section we restrict ourselves to infinitesimally concentrated sources: that is, **P** consists of a set of point magnetic dipoles ($\mathbf{P}_n$), each located at some chosen $\mathbf{r}_n'$ on its respective auxiliary surface. With these delta function source distributions, the integrals in (7) are simply equal to the integrands evaluated at R= $|\mathbf{r} - \mathbf{r}_n'|$, with sources equal to $\mathbf{P}_n$, respectively. For an appropriate selection of source coefficients, (7) tend to the exact solutions as $N \to \infty$.

The final system of algebraic equations is obtained by enforcing the standard normal and tangential magnetic field boundary conditions at points spread over all (internal and external) *physical* surfaces. The number of collocation points is the same as the number of unknown ($\mathbf{P}_n$) elements, so the system is closed, being neither under- nor over-determined. More points may be chosen if one wishes to pursue an optimized solution in the least-squares sense, but we did not find that to be necessary here.

2.3 MAS for a heterogeneous target

We now extend the MAS to treat heterogeneous targets. Beyond its efficiency and accuracy, the MAS approach recommends itself here because source singularities are displaced from the physical surfaces over which the boundary conditions are enforced. As we shall see below, this means that when two physical surfaces are very near one another, the singularities on one do not complicate calculations on the other.

To begin, consider a heterogeneous object containing distinct, homogeneous, highly conducting and permeable sections, $\mathrm{l} = 1,2,...,N_{\mathrm{sec}}$, where N_{sec} is the number of sections. Each section is characterized by relative permeability $\mu_{\ell,\mathrm{r}}$ and conductivity $\sigma_{\ell,\mathrm{r}}$ [S/m]. The region external to the object is Region 0, and the region internal to each section is Region ℓ The object's surrounding surface *S* can be expressed as $S = \Sigma_{\mathrm{l}=1}^{N_{\mathrm{l}}} S_{\mathrm{l}}$, where S_{l} is the surface of the ℓ-th section, excluding common boundaries between nearby sections. The common surface between ℓ-th and $\mathrm{l}+1$-th sections is $S_{\mathrm{l},\mathrm{l}+1}$. The unit normal vector $\hat{\mathbf{n}}_\ell$

points outward from the boundary S_{l} lying between Region 0 and the ℓ-th section and $\hat{\mathbf{n}}_{\ell,\ell+1}$ on $S_{\mathrm{l},\mathrm{l}+1}$ points from Section $\mathrm{l}+1$ to Section ℓ (Figure 2-4).

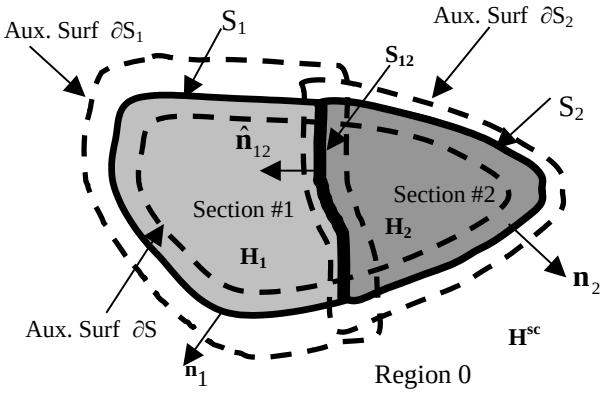

Figure 2-4: MAS diagram for a heterogeneous object.

Again, the target is illuminated with a time-varying primary electromagnetic field that penetrates it to some degree, inducing currents within and producing a secondary/scattered field outside. In the magneto-quasi-static regime considered here, displacement currents $\partial\mathbf{D}/\partial t$ can be neglected in comparison with conduction currents $\sigma_\ell \mathbf{E}_\ell$ [26]. The electromagnetic fields inside of each section of the metallic object are governed by the Helmholtz equation within each homogeneous sub-region, as opposed to the original "double curl" equation.

The boundary conditions on each surface of and within the object are the continuity of the tangential components of $\mathbf{H}$ and of the normal components of $\mathbf{B}$. Namely,

$$\text{on surface } S_{\mathrm{l}}:\ \hat{\boldsymbol{\xi}}_{1,\ell}(\mathbf{r})\cdot\left[\mathbf{H}^{\mathrm{sc}}(\mathbf{r})+\mathbf{H}^{\mathrm{pr}}(\mathbf{r})\right]-\hat{\boldsymbol{\xi}}_{2,\ell}(\mathbf{r})\cdot\mathbf{H}_\ell(\mathbf{r})=0\,, \tag{8}$$

$$\text{on surface } S_{\mathrm{l},\mathrm{l}+1}:\ \hat{\boldsymbol{\eta}}_{1,\ell}(\mathbf{r})\cdot\mathbf{H}_\ell(\mathbf{r})-\hat{\boldsymbol{\eta}}_{2,\ell}(\mathbf{r})\cdot\mathbf{H}_{\ell+1}(\mathbf{r})=0\,, \tag{9}$$

where each $\hat{\boldsymbol{\xi}}_{\mathrm{i},\ell}(\mathbf{r})$ and $\hat{\boldsymbol{\eta}}_{i,\ell}(\mathbf{r})$ vector consists of two independent tangential and one normal vector at each point on the S_{l} and $S_{\mathrm{l},\mathrm{l}+1}$ surfaces. In the case of the tangential vectors, $\hat{\boldsymbol{\xi}}_{2,\ell}(\mathbf{r}) = \hat{\boldsymbol{\xi}}_{1,\ell}(\mathbf{r})$, $\hat{\eta}_{2,\ell}=\hat{\eta}_{1,\ell}$, while for the normal case $\hat{\boldsymbol{\xi}}_{2,\ell}(\mathbf{r}) = \mu_{\ell,\mathrm{r}}\hat{\boldsymbol{\xi}}_{1,\ell}(\mathbf{r})$, $\mu_{\ell,\mathrm{r}}\hat{\eta}_{1,\ell}=\mu_{\ell+1,\mathrm{r}}\hat{\eta}_{2,\ell}$. The $\mathbf{H}^{\mathrm{sc}}(\mathbf{r})$ are scattered magnetic fields and they are simulated using auxiliary magnetic charges placed on auxiliary surfaces ∂S [19-20, 26]. We emphasize that these auxiliary surfaces ∂S are enclosed by the physical surfaces $S=\sum_{\mathrm{l}=1}^{N_{\mathrm{sec}}} S_{\mathrm{l}}$ and assume that the auxiliary charges radiate as if in an unbounded free space with the characteristics of Region 0, giving rise to the secondary field $\mathbf{H}^{\mathrm{sc}}(\mathbf{r})$. Similarly, $\mathbf{H}_{\mathrm{l}}(\mathbf{r})$ is produced by auxiliary magnetic dipoles placed on the external auxiliary surface ∂S_ℓ and assumed to radiate in unbounded homogeneous space filled with ℓ-th target's material properties [26]. By applying boundary conditions (8) and (9) at

given points, the result is a linear system of equations in which the amplitudes of the auxiliary sources can be determined. A more explicit form of the $\mathbf{H}_{\text{l}}(\mathbf{r})$ magnetic field is presented in [26].

The formulation is designed for an arbitrary primary field. In some of the cases investigated below, we specialize $\mathbf{H}^{\text{pr}}$ to represent the primary field transmitted by a sensor containing transmitting coils. Figure 2-5 shows the configuration one of such sensor, which is intended to be similar to that employed in the UWB GEM-3 sensor. The currents in these loops circulate in opposite directions and are scaled so that their respective primary fields cancel at their common center, where a receiving coil is located. The transmitter loops are idealized as infinitely thin line sources of radii a_1 and a_2 through which currents I_1 and $I_2 = -I_1\, a_2/a_1$ flow. The complete primary field produced at any observation point $\mathbf{r}$ by the two loops together is determined simply from the Biot-Savart law,

$$\mathbf{H}(\mathbf{r}) = \frac{1}{4\pi}\sum_{i=1}^{N_1}\frac{I_1[\Delta\ell_{1,i}\times\mathbf{R}_{1,i}]}{R_{1,i}^3} + \frac{1}{4\pi}\sum_{i=1}^{N_2}\frac{I_2[\Delta\ell_{2,i}\times\mathbf{R}_{2,i}]}{R_{2,i}^3}, \tag{10}$$

where, for the j^{th} transmitter loop, $R_{j,i} = |\mathbf{r} - \mathbf{r}'_{j,i}|$, $\mathbf{r}'_{j,i}$ is the location of the i^{th} current element, and $\Delta\mathbf{l}_{j,i}$ is the tangential length vector for the i^{th} subsection of the loop. The same procedures are valid for calculating the primary electromagnetic fields for an arbitrary shape transmitter coil.

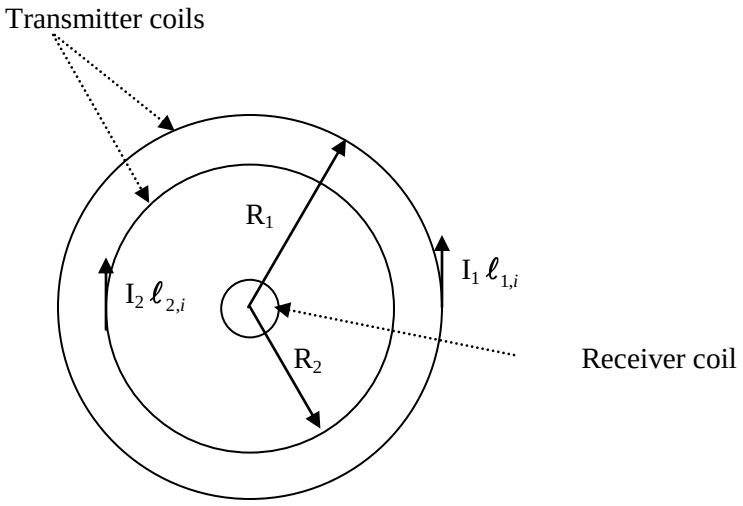

Figure 2-5: Loop geometry of antenna.

2.4 Numerical implementation of the MAS for EMI problems in free space

In the ensuing analysis we consider that the surface of the body is smooth. One can see in Figure 2-2, which shows a schematic diagram of the geometry of the problem, that there are two auxiliary surfaces and that these are positioned inside and outside the physical surface ∂D of the target. The real (physical) surface ∂D is divided into M subsurfaces. For each m^{th} subsurface, a location point $\mathbf{r}_m$, the surface normal there $\hat{\mathbf{n}}_m$, and the surface tangential vectors $\hat{\mathbf{s}}_m$ and $\hat{\mathbf{t}}_m$ are determined using $\hat{\mathbf{n}}_m = [\hat{\mathbf{t}}_m \times \hat{\mathbf{s}}_m]$. Similarly, ∂D_1 is divided into a finite number N of subsurfaces. The secondary field in region 1 due to the target will be generated by N magnetic point charges, $\{Q_n\}$, $n = 1, 2, 3, ..., N$, placed on the surface ∂D_1 at the points $\mathbf{r}_{1n}$. We emphasize that this auxiliary surface is enclosed by the physical

surface ∂D and these charges $\{Q_n\}$ radiate as if in an unbounded free space, giving rise to the secondary field $\mathbf{H}_1^{sc}$. The total field in Region 1, external to the target, is simply the sum of the primary and secondary fields $\mathbf{H}^{pr} + \mathbf{H}_1^{sc}$ where the latter may be represented at point $\mathbf{r}_m$ as

$$\mathbf{H}_1^{sc}(\mathbf{r}_m) = \sum_{n=1}^{N} \mathbf{G}_Q(m,n) = \sum_{n=1}^{N} \frac{Q_n}{4\pi\mu_0} \frac{(\mathbf{r}_m - \mathbf{r}_{1n})}{|\mathbf{r}_m - \mathbf{r}_{1n}|^3}, \quad \text{with } \mathbf{r}_m \in \partial D \text{ and } \mathbf{r}_{1n} \in \partial D_1, \tag{11}$$

where $\mathbf{G}_Q(m,n)$, the magnetic field due to a magnetic charge source Q_n placed at point $\mathbf{r}_{1n}$ and evaluated at $\mathbf{r}_m$ is obtained by taking the gradient of a scalar potential satisfying Poisson's equation.

The induced field $\mathbf{H}_2$ inside the target is assumed to be generated by a finite set of N point vector magnetic dipole sources, $\mathbf{P}_n$, $n = 1, 2, 3, ..., N$, distributed over the surface ∂D_2, which also encloses the target. These dipole sources are assumed to radiate in an unbounded homogeneous space filled with the target's material properties; the induced $\mathbf{H}_2$ field at point $\mathbf{r}_m$ can be given as

$$\mathbf{H}_2(\mathbf{r}_m) = \sum_{n=1}^{N} \mathbf{G}_p(m,n) = \sum_{n=1}^{N} [\mathbf{P}_n \cdot F_1(r_{mn}) + (\mathbf{r}_m - \mathbf{r}_{2n}) \cdot F_2(r_{mn}) \cdot (\mathbf{P}_n \cdot (\mathbf{r}_m - \mathbf{r}_{2n}))], \tag{12}$$

where $\mathbf{P}_n$ represents a magnetic dipole moment arbitrarily oriented in the global Cartesian XYZ coordinate system, $\mathbf{r}_{2n}$ is the radius vector of the n^{th} magnetic dipole source in the global coordinate system, and the functions F_1 and F_2 are given by:

$$F_1(r_{mn}) = \frac{-1 - jkr_{mn} + k^2 r_{mn}^2}{4\pi\mu r_{mn}^2} e^{-jkr_{mn}} \quad \text{and} \quad F_2(r_{mn}) = \frac{3 + j3kr_{mn} - k^2 r_{mn}^2}{4\pi\mu r_{mn}^5} e^{-jkr_{mn}} \quad \text{with} \quad r_{mn} = |\mathbf{r}_m - \mathbf{r}_{2n}|. \tag{13}$$

The auxiliary surface ∂D_2 is divided into *N* subsurfaces, and on each subsurface one can define an orthogonal local coordinate system, $\hat{\mathbf{n}}_{2n}, \hat{\mathbf{t}}_{2n}, \hat{\mathbf{s}}_{2n}$, the first unit vector being normal and the other two tangential to the surface. The relation between the local and the global coordinate systems is given by

$$\hat{\mathbf{t}}_{2n} = T_{2n}^x \hat{\mathbf{x}} + T_{2n}^y \hat{\mathbf{y}} + T_{2n}^z \hat{\mathbf{z}}, \tag{14}$$

$$\hat{\mathbf{s}}_{2n} = S_{2n}^x \hat{\mathbf{x}} + S_{2n}^y \hat{\mathbf{y}} + S_{2n}^z \hat{\mathbf{z}}, \tag{15}$$

$$\hat{\mathbf{n}}_{2n} = N_{2n}^x \hat{\mathbf{x}} + N_{2n}^y \hat{\mathbf{y}} + N_{2n}^z \hat{\mathbf{z}}, \tag{16}$$

where $\hat{\mathbf{x}}$, $\hat{\mathbf{y}}$, and $\hat{\mathbf{z}}$ represent the unit vectors of the global coordinate system. According to the demands of the problem, we may reduce the number of unknowns by specifying in the local coordinate system a set of magnetic dipole moments, each of which has only two independent components along the tangential directions $\hat{\mathbf{t}}_{2n}$ and $\hat{\mathbf{s}}_{2n}$. In doing so, we rely on the directional diversity over space of the fields emanating from a set of point dipoles to provide a sufficient basis for all directional components on the real surface. Thus based on relations (14) and (15) between local and global coordinate systems, we can write the unknown vector $\mathbf{P}_n$ in the global coordinate system as

$$\mathbf{P}_n = P_n^t \hat{\mathbf{t}}_{2n} + P_n^s \hat{\mathbf{s}}_{2n}, \tag{17}$$

with unknown coefficients P_n^t and P_n^s. Substituting (17) into (12) provides an expression for the magnetic field in region 2 at a point $\mathbf{r}_m$:

$$\mathbf{H}_2(\mathbf{r}_m) \;=\; \sum_{n=1}^{N_2}[\mathbf{G}_P^t(m,n)+\mathbf{G}_P^s(m,n)]\,,\mathbf{r}_m \in \partial D\,, \tag{18}$$

where $\mathbf{G}_P^t(m,n)$ is the magnetic field at point $\mathbf{r}_m$ due to a dipole source P_n^t located at $\mathbf{r}_{2n}$ and oriented in the $\hat{\mathbf{t}}_{2n}$ direction,

$$\mathbf{G}_P^t(m,n) = P_n^t\left[\hat{\mathbf{t}}_{2n}F_1\left(r_{mn}\right)+\left(\mathbf{r}_m-\mathbf{r}_{2n}\right)F_2\left(r_{mn}\right)\left\{\hat{\mathbf{t}}_{2n}\cdot\left(\mathbf{r}_m-\mathbf{r}_{2n}\right)\right\}\right] \;\text{ with }\; \mathbf{r}_{2n}\in\partial D_2\,, \tag{19}$$

and $\mathbf{G}_P^s(m,n)$ is expressed analogously, with $\hat{\mathbf{s}}_{2\mathrm{n}}$ in place of $\hat{\mathbf{t}}_{2n}$. Altogether, the magnetic field expressions (11) and (12) in the respective regions have three sets of unknown scalar coefficients; a set of N coefficients, $\{Q_n\}$, $\{P_n^t\}$, and $\{P_n^s\}$, $n=1,2,3,...,N$.

Continuity of tangential components of magnetic field and normal components of magnetic flux density vector is enforced at points $\mathbf{r}_m$, m = 1, 2, …, M, distributed over the physical boundary ∂D. This provides a sufficient number of independent linear equations to determine the unknown sets of coefficients, assuming that $M \geq N$. For the inequality we must apply some sort of error minimization scheme to identify the desired coefficients. For the equality, used in all examples here, the algebraic system can be inverted uniquely and is obtained by substituting the explicit field expressions (11) and (12) into the boundary conditions, arranged in the form

$$\begin{aligned}
\hat{\mathbf{t}}_m\cdot\{\,\mathbf{H}_1^{\mathrm{sc}}(\mathbf{r}_m)-\mathbf{H}_2(\mathbf{r}_m) &= \quad \mathbf{H}^{\mathrm{pr}}(\mathbf{r}_m)\,\}\\
\hat{\mathbf{s}}_m\cdot\{\,\mathbf{H}_1^{\mathrm{sc}}(\mathbf{r}_m)-\mathbf{H}_2(\mathbf{r}_m) &= \quad \mathbf{H}^{\mathrm{pr}}(\mathbf{r}_m)\,\}\\
\hat{\mathbf{n}}_m\cdot\{\,\mu_0\mathbf{H}_1^{\mathrm{sc}}(\mathbf{r}_m)-\mu\mathbf{H}_2(\mathbf{r}_m) &= \mu_0\mathbf{H}^{\mathrm{pr}}(\mathbf{r}_m)\,\}
\end{aligned} \tag{20}$$

for each $\mathbf{r}_m\in\partial D$, $m=1,2,3,...,M$. Once the unknown coefficients of the auxiliary sources are obtained, the approximate field can be evaluated easily in either region by simple summation of the source influences, *i.e.* using (11) or (12) with an arbitrary $\mathbf{r}$ in place of $\mathbf{r}_m$.

2.5 Numerical implementation of the MAS for EMI problems in conducting media

In the underwater EMI problem one enforces the continuity of tangential components of magnetic and electric fields across the two object/water interfaces $\sum_1$ and $\sum_2$ at m = 1, 2, …, M points on each. As in the free-space problem, this provides a sufficient number of independent linear equations to determine the sets of unknown coefficients corresponding to the strengths of the interior and exterior distributed magnetic dipoles. Again, for the inequality we must apply some sort of error minimization scheme to identify the desired coefficients. For the equality, used in all examples here, the algebraic system can be inverted uniquely and is obtained once again by substituting the field expressions into the boundary conditions, which are now arranged as

$$\begin{aligned}
\hat{\mathbf{t}}_m \cdot \{\, \mathbf{H_1}(\mathbf{r}_m) - \mathbf{H}_2(\mathbf{r}_m) = \mathbf{H}^{\mathrm{pr}}(\mathbf{r}_m) \,\} \\
\hat{\mathbf{s}}_m \cdot \{\, \mathbf{H_1}(\mathbf{r}_m) - \mathbf{H}_2(\mathbf{r}_m) = \mathbf{H}^{\mathrm{pr}}(\mathbf{r}_m) \,\} \\
\hat{\mathbf{t}}_m \cdot \{\, \mathbf{E_1}(\mathbf{r}_m) - \mathbf{E}_2(\mathbf{r}_m) = \mathbf{E}^{\mathrm{pr}}(\mathbf{r}_m) \,\} \\
\hat{\mathbf{s}}_m \cdot \{\, \mathbf{E_1}(\mathbf{r}_m) - \mathbf{E}_2(\mathbf{r}_m) = \mathbf{E}^{\mathrm{pr}}(\mathbf{r}_m) \,\}
\end{aligned} \tag{21}$$

applied for each $\mathbf{r}_m \in \sum_1$ and $\sum_2$, $m = 1, 2, 3, ..., M$.

For the electric field we have

$$\mathbf{E}(\mathbf{r}_m) = \sum_{n=1}^{N_2} [\mathbf{Ge}_P^t(m,n) + \mathbf{Ge}_P^s(m,n)] \tag{22}$$

where

$$\begin{aligned}
\mathbf{Ge}_P^t(\mathbf{r}) &= -\frac{j\omega}{4\pi R_{mn}} \mathrm{e}^{jkr} \left(\frac{1}{R_{mn}^2} - \frac{jk}{R_{mn}} \right) (\hat{\mathbf{t}}_m \times (\mathbf{r}_m - \mathbf{r}_{\lambda n})), \quad \lambda = 1 \text{ or } 2, \\
\mathbf{Ge}_P^s(\mathbf{r}) &= -\frac{j\omega}{4\pi R_{mn}} \mathrm{e}^{jkr} \left(\frac{1}{R_{mn}^2} - \frac{jk}{R_{mn}} \right) (\hat{\mathbf{s}}_m \times (\mathbf{r}_m - \mathbf{r}_{\lambda n})), \quad \mathrm{R}_{mn} = |\mathbf{r}_m - \mathbf{r}_{\lambda n}|.
\end{aligned} \tag{23}$$

Also, $\mathbf{H_1}(\mathbf{r}_m)$ is the scattered magnetic field in Region 1 produced by magnetic charges distributed inside the object and radiating in a space filled with the electromagnetic parameters of Region 1. Once the coefficients of the auxiliary magnetic dipole sources are obtained it is easy to evaluate the approximate electric and magnetic fields in either region by simply summing the source influences.

2.6 Formulation for bodies of revolution

Many UXO and objects handily representative of UXO can be modeled as bodies of revolution (BOR). While a BOR is ultimately three-dimensional and produces 3D scattered fields, its rotational symmetry reduces the computational problem to 2D. Details of typical BOR formulations for other techniques, such as MoM, appear in the references [30-34]. Here we indicate only the particular expressions needed in terms of auxiliary sources.

Consider a conducting and permeable BOR formed by rotating a generating line about the *z*-axis of a Cartesian coordinate system and placed in a time-harmonic primary magnetic field (which need not itself be rotationally symmetric). The azimuthal dependence of the fields is expressed via a Fourier series, whose modes $\exp(jL\phi)$ are used to include all rotational variation. Since the azimuthal field variation is analytically accounted for, no boundary condition matching points are distributed in the azimuthal $\hat{\boldsymbol{\varphi}}$ direction. The resulting sets of simultaneous equations may be represented in matrix form as

$$[Z^L][I^L] = [V^L] \quad \text{for} \quad L = 0, \pm 1, \pm 2, \pm 3, \cdots \tag{24}$$

where $[Z^L]$ is the impedance matrix for the *L*-th Fourier mode, I^L is a column vector containing the unknown amplitude of the auxiliary sources for the *L*-th Fourier mode, and $[V^L]$ is the driving vector for the *L*-th Fourier mode.

The generating line is divided into segments by *M* points. With reference to the conventional cylindrical coordinate system $(\rho, \varphi, \mathrm{z})$, a unit vector $\hat{\mathbf{t}}$ is defined tangentially along the curve such that

$\hat{\mathbf{t}} \cdot \hat{\boldsymbol{\varphi}} = 0$ and $\hat{\mathbf{n}} = \hat{\mathbf{t}} \times \hat{\boldsymbol{\varphi}}$. For each segment on the real surface an azimuthal belt (ring) is defined, and corresponding azimuthal belts of source locations are determined on the two auxiliary surfaces. The secondary fields $\mathbf{H}_1^{\text{sc}}(\mathbf{r}_m)$ and $\mathbf{H}_2(\mathbf{r}_m)$ in Regions 1 and 2, respectively, can be generated by the sources from *N* auxiliary belts through

$$\mathbf{H}_1^{\text{sc}}(\mathbf{r}_m) = \sum_{n=1}^{N} \mathbf{G}_Q^{\varphi}(m,n), \tag{25}$$

$$\mathbf{H}_2(\mathbf{r}_m) = \sum_{n=1}^{N} \mathbf{G}_P^{\varphi}(m,n), \tag{26}$$

where in (25)

$$\mathbf{G}_Q^{\varphi}(m,n) = \frac{1}{4\pi\mu_0} \sum_{i\varphi=1}^{N_\varphi(n)} \frac{Q_n(\varphi)}{|\mathbf{r}_m - \mathbf{r}_{1n,i\varphi}|} (\mathbf{r}_m - \mathbf{r}_{1n,i\varphi}) \tag{27}$$

is the scattering magnetic field in region 1 at the point $\mathbf{r}_m$ produced by a magnetic charge $Q_n(\varphi)$ distributed on the n^{th} inner auxiliary belt (ring) at $\mathbf{r}_{1n,i\varphi} = \rho_{1n}(\hat{\mathbf{x}}\cos\varphi_{i\varphi} + \hat{y}\sin\varphi_{i\varphi}) + \hat{\mathbf{z}}z_{1n}$, where ρ_{1n} is the belt's radius and $N_\varphi(n)$ is the number of azimuthal points on the belt. Similarly, in (26)

$$\mathbf{G}_P^{\varphi}(m,n) = \sum_{i\varphi=1}^{N_\varphi(n)} [\mathbf{P}_n(\varphi) \cdot F_1(r_{mn,i\varphi}) + (\mathbf{r}_m - \mathbf{r}_{2n,i\varphi}) \cdot F_2(r_{mn,i\varphi}) \cdot (\mathbf{P}_n(\varphi) \cdot (\mathbf{r}_m - \mathbf{r}_{2n,i\varphi}))] \tag{28}$$

is the induced magnetic field in region 2 produced by the magnetic dipole $\mathbf{P}_n(\varphi)$ distributed on the n^{th} outer auxiliary belt, $\mathbf{r}_{2n,i\varphi} = \rho_{2n}(\hat{\mathbf{x}}\cos\varphi_{i\varphi} + \hat{y}\sin\varphi_{i\varphi}) + \hat{\mathbf{z}}z_{2n}$ with ρ_{2n} being the belt's radius, and $r_{mn,i\varphi} = |\mathbf{r}_m - \mathbf{r}_{2n,i\varphi}|$.

For the BOR problem at hand, we include the φ dependence of $\mathbf{H}^{\text{pr}}$, $Q_n(\varphi)$ in (27) and $\mathbf{P}_n(\varphi)$ in (28) by expanding them in Fourier series in φ:

$$\mathbf{H}^{pr} = \sum_{L=0}^{\infty} (\mathbf{H}_{t,L}^{pr} \cos(L\varphi) + \mathbf{H}_{\varphi,L}^{pr} \sin(L\varphi)), \tag{29}$$

$$Q_n(\varphi) = \sum_{L=0}^{\infty} (Q_{n,L}^{t} \cos(L\varphi) + Q_{n,L}^{\varphi} \sin(L\varphi)) \tag{30}$$

$$\mathbf{P}_n(\varphi) = \sum_{L=0}^{\infty} (\mathbf{P}_{n,L}^{t} \cos(L\varphi) + \mathbf{P}_{n,L}^{\varphi} \sin(L\varphi)), \tag{31}$$

where *L* is the mode number, and $\mathbf{H}_{t,L}^{\text{pr}}$, $\mathbf{H}_{\varphi,L}^{\text{pr}}$, $\mathbf{P}_{n,L}^{t}$, $\mathbf{P}_{n.L}^{\varphi}$, $Q_{n,L}^{t}$, and $Q_{n,L}^{\varphi}$ are the Fourier coefficients. These coefficients are dependent only on ρ and *z* and according to rotational symmetry they are constant on each belt (ring).

Finally, the formulation is achieved by substituting (30) and (31) into (27) and (28), and then into (26) and (25), so that the scattered $\mathbf{H}_1^{\text{sc}}(\mathbf{r}_m)$ and induced $\mathbf{H}_2(\mathbf{r}_m)$ magnetic fields at $\mathbf{r}_m$ from all Fourier modes can be represented as

$$\mathbf{H}_1^{\mathrm{sc}}(\mathbf{r}_m) = \sum_{L=0}^{\infty}\left\{\sum_{n=1}^{N} Q_{n,L}^{t}\mathbf{G}_{1Q}^{\varphi}(m,n,L)+\sum_{n=1}^{N} Q_{n,L}^{\varphi}\mathbf{G}_{2Q}^{\varphi}(m,n,L)\right\}, \tag{32}$$

$$\mathbf{H}_2(\mathbf{r}_m) = \sum_{L=0}^{\infty}\left\{\sum_{n=1}^{N} P_{n,L}^{t}\mathbf{G}_{1P}^{\varphi}(m,n,L)+\sum_{n=1}^{N} P_{n,L}^{\varphi}\mathbf{G}_{2P}^{\varphi}(m,n,L)\right\}, \tag{33}$$

where

$$\mathbf{G}_{1Q}^{\varphi}(m,n,L)=\frac{1}{4\pi\mu_0}\sum_{i\varphi=1}^{N_\varphi(n)}\frac{\cos(L\varphi_{i\varphi})}{\left|\mathbf{r}_m-\mathbf{r}_{1n,i\varphi}\right|}(\mathbf{r}_m-\mathbf{r}_{1n,i\varphi}), \tag{34}$$

$$\mathbf{G}_{2Q}^{\varphi}(m,n,L)=\frac{1}{4\pi\mu_0}\sum_{i\varphi=1}^{N_\varphi(n)}\frac{\sin(L\varphi_{i\varphi})}{\left|\mathbf{r}_m-\mathbf{r}_{1n,i\varphi}\right|}(\mathbf{r}_m-\mathbf{r}_{1n,i\varphi}), \tag{35}$$

$$\mathbf{G}_{1P}^{\varphi}(m,n,L)=\sum_{i\varphi=1}^{N_\varphi(n)}\cos(L\varphi_{i\varphi})[\hat{\mathbf{t}}_n\cdot F_1(r_{mn,i\varphi})+(\mathbf{r}_m-\mathbf{r}_{2n,i\varphi})\cdot F_2(r_{mn,i\varphi})\cdot(\hat{\mathbf{t}}_n\cdot(\mathbf{r}_m-\mathbf{r}_{2n,i\varphi}))], \tag{36}$$

$$\mathbf{G}_{2P}^{\varphi}(m,n,L)=\sum_{i\varphi=1}^{N_\varphi(n)}\sin(L\varphi_{i\varphi})[\hat{\boldsymbol{\varphi}}_n\cdot F_1(r_{mn,i\varphi})+(\mathbf{r}_m-\mathbf{r}_{2n,i\varphi})\cdot F_2(r_{mn,i\varphi})\cdot(\hat{\boldsymbol{\varphi}}_n\cdot(\mathbf{r}_m-\mathbf{r}_{2n,i\varphi}))], \tag{37}$$

$$\varphi_{i\varphi}=\frac{2\pi}{N_\varphi(n)}i\varphi,\quad i\varphi=1,\,2,\,\ldots,\,N_\varphi(n). \tag{38}$$

When the primary field is uniformly parallel to the *z*- (symmetry-) axis, we have axial excitation and need only deal with the zeroth component: $\mathbf{H}^{\mathrm{pr}} = H_0\hat{\mathbf{z}}$ and $L = 0$. Thus only Q^t and $\mathbf{P}^t$ enter the problem, and we choose matching points $\mathbf{r}_m$ at $\phi = 0$ on the real surface. This mode permits consideration of loop sources as well as spatially uniform excitation fields. The algebraic system is provided by applying only the first and last of equations (20). For spatially uniform transverse excitation $\mathbf{H}^{\mathrm{pr}} = H_0\hat{\mathbf{x}}$ we only treat the $L = 1$ component, all of Q^t, Q^φ, $\mathbf{P}^t$, and $\mathbf{P}^\varphi$ enter the problem, and we choose matching points $\mathbf{r}_m$ at $\phi = 0$ and $\pi/2$ on the real surface. By combining axial and transverse excitation cases we can treat any orientation of the object relative to a uniform primary field. In both cases we must sum the effects of sources distributed both longitudinally (in the $\hat{\mathbf{t}}$ direction) and in the $\hat{\boldsymbol{\varphi}}$ direction, though the variation of the sources in the latter direction is simply dictated by the value of L considered.

2.7 Skin-effect approximation

We will consider the conductor of general shape shown schematically in Figure 2-6. For the purpose of visualization, this drawing may be considered the cross section of a cylindrical body. The conductor is characterized by a minimum radius of curvature $R_{\min}$ and a minimum thickness, $t_{\min}$. An electromagnetic source, external to the conductor, produces a field/current within the conductor, and it is the behavior of this field that is described by the skin effect. We assume that the electromagnetic source is time-harmonic with angular frequency ω and relate the time-varying field $\xi(t)$ to the complex vector phasor $E(\omega)$ by

$$\xi(t)=\mathrm{Re}[E(\omega)e^{j\omega t}]. \tag{39}$$

The electrical properties of the conductor are described by three simple linear constitutive parameters: the electrical conductivity σ, the permittivity ε, and the permeability μ. For the surrounding free-space, these parameters are $\sigma = 0,\ \varepsilon = \varepsilon_0,\ \mu = \mu_0$ (in SI units). The following Maxwell equations apply in both regions, the conductor and free-space, on substitution of the appropriate constitutive relations:

$$\nabla \times \mathbf{E} = -j\omega\mu\mathbf{H}, \tag{40}$$

$$\nabla \times \mathbf{H} = \sigma\mathbf{E} + j\omega\varepsilon\mathbf{E}, \tag{41}$$

$$\nabla \bullet \mathbf{E} = 0 \tag{42}$$

$$\nabla \bullet \mathbf{B} = 0. \tag{43}$$

These equations can be combined to obtain a vector Helmholtz equation for the electric or the magnetic field:

$$[\nabla^2 - j\omega\mu(\sigma + j\omega\varepsilon)]\begin{Bmatrix}\mathbf{E}\\ \mathbf{H}\end{Bmatrix} = 0\,, \text{ where } \nabla^2\mathbf{A} \equiv \nabla(\nabla \bullet \mathbf{A}) - \nabla \times (\nabla \times \mathbf{A})\,. \tag{44}$$

Our derivation will presuppose that the electromagnetic field/current within the conductor is confined to a layer of thickness Δ at the surface. Our objective is to determine the conditions under which this is indeed true and to obtain the explicit behavior of the field within this layer. We will be careful to note all assumptions made during the derivation.

Our first assumption is that we are dealing with a good conductor at the frequency of interest, and thus $\sigma / \omega\varepsilon \gg 1$, making (44) within the conductor adopt the form

$$(\nabla^2 - j\omega\mu\sigma)\begin{Bmatrix}\mathbf{E}\\ \mathbf{H}\end{Bmatrix} = 0\,. \tag{45}$$

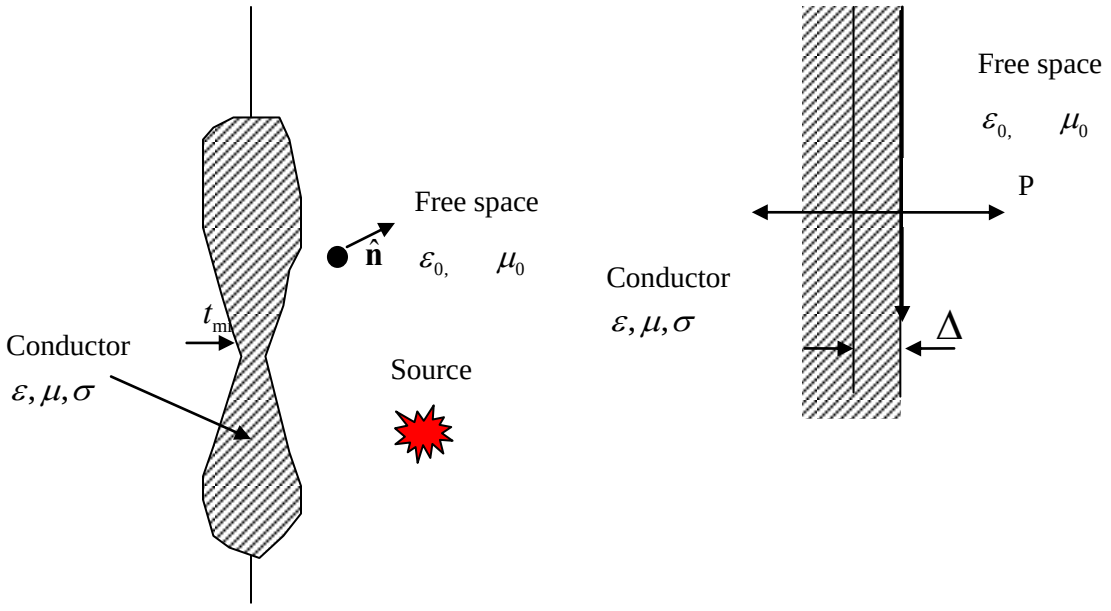

Figure 2-6: Skin effect
(Left) Schematic drawing of the skin effect for a conductor of general shape. (Right) Local Cartesian coordinate system at point P.

Now the minimum radius of curvature $R_{\min}$ is assumed to be large compared to Δ, and the minimum thickness $t_{\min}$ at least twice Δ:

$$R_{\min} \gg \Delta, \tag{46}$$

$$t_{\min} > 2\Delta. \tag{47}$$

The local region of surface surrounding a point *P* on the conductor (an area whose sides are several Δ in length) can then be considered approximately planar, and (45) can be written in terms of the local rectangular coordinates:

$$\left(\frac{\partial^2}{\partial x^2}+\frac{\partial^2}{\partial y^2}+\frac{\partial^2}{\partial z^2}-j\omega\mu\sigma\right)\begin{Bmatrix}E_i\\H_i\end{Bmatrix}=0, \tag{48}$$

where $i = x, y,$ or z.

Our final assumption involves the variation of the electromagnetic field in the directions (x,y) along the surface of the conductor. Within the conductor (the layer of thickness Δ) this variation will be assumed small compared to the variation in the normal (z-) direction; specifically,

$$\left|\frac{\partial^2 H_x}{\partial x^2}\right| \ll \left|\frac{\partial^2 H_x}{\partial z^2}\right|, \qquad \left|\frac{\partial^2 H_y}{\partial y^2}\right| \ll \left|\frac{\partial^2 H_y}{\partial z^2}\right|, \qquad \left|\frac{\partial^2 H_x}{\partial x \partial y}\right| \ll \left|\frac{\partial^2 H_x}{\partial z^2}\right|, \tag{49}$$

with similar expressions for the second partial derivatives of the components of **E**. After applying (49), the partial differential equation (48) becomes

$$\left(\frac{\partial^2}{\partial z^2}-j\omega\mu\sigma\right)\begin{Bmatrix}E_i\\H_i\end{Bmatrix}=0, \tag{50}$$

whose solution is simply

$$\begin{Bmatrix}E\\H\end{Bmatrix}=\begin{Bmatrix}E_i(z=0)\\H_i(z=0)\end{Bmatrix}e^{-(1+j)z/\delta}, \tag{51}$$

where the parameter δ is the classical skin depth:

$$\delta \equiv \sqrt{2/\omega\mu\sigma}. \tag{52}$$

We have chosen the solution to (50) that decays exponentially as we proceed into the conductor rather than the one that grows exponentially; this is in keeping with our assumption that the field is confined to a layer at the surface of the conductor. The thickness of this layer is seen to be about

$$\Delta \approx 3\delta(\exp(-3)) = 3\delta \times 4.97 \times 10^{-2}. \tag{53}$$

Within the conductor specific components of the field are related by Maxwell's equations (40)–(43); for example, a relationship between the components of **E** and **H** tangential to the surface can be established using (41) and (43). After making use of (40) in (41), the components of E tangential to the surface become

$$E_x\hat{\mathbf{x}} + E_x\hat{\mathbf{y}} = \frac{1}{\sigma}\left[\hat{\mathbf{x}}\left(\frac{\partial H_z}{\partial y} - \frac{\partial H_y}{\partial z},\right) + \hat{\mathbf{y}}\left(\frac{\partial H_x}{\partial z} - \frac{\partial H_z}{\partial x}\right)\right], \tag{54}$$

and after differentiating with respect to *z*,

$$\frac{\partial E_x}{\partial z}\hat{\mathbf{x}} + \frac{\partial E_y}{\partial z}\hat{\mathbf{y}} = \frac{1}{\sigma}\left[\hat{\mathbf{x}}\left(\frac{\partial^2 H_z}{\partial z \partial y} - \frac{\partial^2 H_y}{\partial z^2},\right) + \hat{\mathbf{y}}\left(\frac{\partial^2 H_x}{\partial z^2} - \frac{\partial H_z}{\partial z \partial x}\right)\right]. \tag{55}$$

From (43) and the constitutive relation $\mathbf{B} = \mu\mathbf{H}$ we obtain

$$\frac{\partial H_z}{\partial z} = -\frac{\partial H_x}{\partial x} - \frac{\partial H_y}{\partial y}, \tag{56}$$

which on substitution into (55) gives

$$\frac{\partial E_x}{\partial z}\hat{\mathbf{x}} + \frac{\partial E_y}{\partial z}\hat{\mathbf{y}} = \frac{1}{\sigma}\left[\hat{\mathbf{x}}\left(-\frac{\partial^2 H_z}{\partial x \partial y} - \frac{\partial^2 H_y}{\partial y^2} - \frac{\partial^2 H_y}{\partial z^2},\right) + \hat{\mathbf{y}}\left(\frac{\partial^2 H_x}{\partial z^2} + \frac{\partial^2 H_x}{\partial x^2}\frac{\partial^2 H_y}{\partial z \partial x}\right)\right]. \tag{57}$$

After applying the inequalities (46) and (47) and the explicit dependence on *z* (51), we obtain the desired relationship:

$$E_x\hat{\mathbf{x}} + E_y\hat{\mathbf{y}} = [(1+j)/\sigma\delta](H_x\hat{\mathbf{x}} - H_x\hat{\mathbf{y}}), \tag{58}$$

or

$$\mathbf{E}_t = [-(1+j)/\sigma\delta]\hat{\mathbf{z}} \times \mathbf{H}_t, \tag{59}$$

where the subscript *t* indicates the component tangential to the surface of the conductor. With $\hat{\mathbf{n}} = -\hat{\mathbf{z}}$ the outward pointing unit vector normal to the surface, $\mathbf{E}_t = -\hat{\mathbf{n}} \times (\hat{\mathbf{n}} \times \mathbf{E})$ and (59) becomes

$$\hat{\mathbf{n}} \times (\hat{\mathbf{n}} \times \mathbf{E}) = [-(1+j)/\sigma\delta]\hat{\mathbf{n}} \times \mathbf{H}. \tag{60}$$

To obtain a similar expression for $\mathbf{H}_t$, we take $\hat{\mathbf{n}} \times$ (60), which gives

$$\mathbf{H}_t = [-(1-j)\sigma\delta/2]\hat{\mathbf{z}} \times \mathbf{E}_t \tag{61}$$

or

$$\hat{\mathbf{n}} \times (\hat{\mathbf{n}} \times \mathbf{H}) = [(1-j)\sigma\delta]\hat{\mathbf{n}} \times \mathbf{E} \tag{62}$$

Let us now summarize what we have learned about the skin-effect approximation and restate the requirements for its use. When the skin-effect approximation applies, the electromagnetic field and the volume current density within the conductor are confined to a thin layer of thickness $\Delta \approx 3\delta$ at the surface of the conductor:

$$E = E(0)e^{-(1+j)w/\delta},\ H = H(0)e^{-(1+j)w/\delta},\quad J = \sigma E = J(0)e^{-(1+j)w/\delta}, \tag{63}$$

where w is the normal distance into conductor. In addition, the components of the electric and magnetic fields tangential to the surface are simply related:

$$\hat{\mathbf{n}} \times (\hat{\mathbf{n}} \times \mathbf{E}) = -Z_s\hat{\mathbf{n}} \times \mathbf{H} \tag{64}$$

or

$$\hat{\mathbf{n}} \times (\hat{\mathbf{n}} \times \mathbf{H}) = (1/Z_s)\hat{\mathbf{n}} \times \mathbf{E}, \tag{65}$$

where we have introduced the surface impedance

$$Z_s \equiv (1+j)/\sigma\delta = (1+j)\sqrt{\omega\mu/2\sigma}\,. \tag{66}$$

Since the tangential components of the field are continuous at the surface, (64) and (65) apply in free space just outside the surface of the conductor.

For the skin effect approximation to apply to the conductor of general shape:

(i) We must have a good conductor at the frequency of interest:

$$\sigma/\omega\varepsilon \gg 1\,. \tag{67}$$

When we introduce the wave number k_0 and wavelength λ_0 for free space $(k_0 = 2\pi/\lambda_0)$ and the relative permittivity $\varepsilon_r = \varepsilon/\varepsilon_0$ and permeability $\mu_r = \mu/\mu_0$ of the conductor, this inequality becomes

$$(2/\varepsilon_r\mu_r)(1/k_0\delta)^2 \gg 1 \tag{68}$$

For a good conductor, like a nonmagnetic metal, we often take $\varepsilon_r \approx 1$ and $\mu_r \approx 1$, and thus

$$2(k_0\delta)^2 = 2(\lambda_0/2\pi\delta)^2 \gg 1, \tag{69}$$

or approximately $2(k_0\delta)^{-2} \gg 1$. In other words, the free-space wavelength must be much larger than the skin depth.

(ii) The minimum radius of curvature $R_{\min}$ and the minimum thickness $t_{\min}$ of the conductor must be large compared to the skin depth:

$$R_{\min} \gg 3\delta\,, \tag{70}$$

$$t_{\min} > 6\delta\,. \tag{71}$$

(iii) Within the conductor the variation of the electromagnetic field in directions along the surface must be small compared to the variation in the normal direction (w). We can express this requirement at each regular point on the surface of the conductor as

$$\frac{\delta^2}{2}\left|\frac{\partial^2 H_u}{\partial u^2}/H_u\right|_{w=0} \ll 1, \quad \frac{\delta^2}{2}\left|\frac{\partial^2 H_v}{\partial v^2}/H_v\right|_{w=0} \ll 1, \quad \frac{\delta^2}{2}\left|\frac{\partial^2 H_u}{\partial u\partial v}/H_u\right|_{w=0} \ll 1, \quad \frac{\delta^2}{2}\left|\frac{\partial^2 H_v}{\partial u\partial v}/H_v\right|_{w=0} \ll 1, \tag{72}$$

where *u*, *v* are the rectangular coordinates on the tangent plane at the point; the *u* and *v* axes are tangent to the lines of curvature for the surface at the point. The inequalities apply to the components of **E**. The first two of these requirements involve the frequency and the material properties and geometry of the conductor. They are fairly obvious and are stated in most textbooks. The last requirement, which is seldom mentioned, involves the source of the field, specifically the distribution of the field produced at the conductor.

2.8 Seawater permittivity model

Underwater (UW) environments, unlike dry soil, are electrically conducting and heterogeneous. This can significantly affect the performance of established and emerging land-based EMI sensing technologies. The dielectric properties of seawater change with frequency, temperature, and salinity, and therefore in order to successfully utilize land-based EMI sensing technologies for UW UXO detection and discrimination it is essential to understand how the dielectric permittivity of seawater affects an object's EMI response. This requires to take into account the frequency, temperature, and salinity variation of seawater's relative permittivity in low-frequency electromagnetic scattering models and to understand

EMI scattering phenomena from highly conducting and permeable metallic objects for current state-of-the-art land-based EMI sensing technologies. There are many models for the complex permittivity of saline water that fit experimental data. The physical mechanism of the relative permittivity of dielectrics is very well documented and explained, for example by Debye [36]. Any dielectric substance placed in an electric field undergoes polarization, which involves the appearance of bound charges on the surface of the dielectric. Polarization, defined as the electric dipole moment per unit volume, may be divided into two categories: induced and orientation polarization. When an electromagnetic field is applied to a dielectric, the induced component of polarization is assumed to have no inertia and almost instantaneously attains a value $\mathbf{P}_i = \varepsilon_0(\varepsilon_\infty - 1)\mathbf{E}$, where ε_0 is the dielectric permittivity of free space, ε_∞ is the infinite-frequency relative permittivity of the dielectric, and **E** is the applied electric field. On the other hand, the orientation polarization rises exponentially to reach a maximum value of $\mathbf{P}_o = \varepsilon_0(\varepsilon_s - 1)\mathbf{E} - \varepsilon_0(\varepsilon_\infty - 1)\mathbf{E}$ as $t \to \infty$, with ε_s the static relative permittivity of the medium. Therefore, for a static electric field **E** the total polarization reaches a maximum value of $\mathbf{P}_o = \varepsilon_0(\varepsilon_s - 1)\mathbf{E}$. The time constant τ of the exponentially increasing orientation polarization is called the relaxation time. It depends on the temperature and salinity of the seawater and is independent of the nature of the electric field and of its time of application.

The dielectric polarization of seawater contains two parts: the dielectric polarization due to a displacement of bound charges and the ionic current. The ionic current is associated with the salinity of the water. However, increased conduction is not the only phenomenon that occurs when salts are dissolved in water. The ions are hydrated to varying extents, and therefore the seawater's dielectric permittivity depends on both temperature and salinity. The physical behavior could be summarized as follows: the conductivity of water increases with the addition of ions, and the increase in conductivity is approximately proportional to the number of ions. The extent of polarization due to the displacement of bound charges (*i.e.*, induced and orientation polarization) in seawater depends on its salinity due to the presence of ions. Therefore, ε_s, ε_∞, and τ are functions of the salinity. The static relative permittivity ε_s of seawater is reduced because the water molecules in the vicinity of an ion orient themselves with respect to it. The number of water molecules that orient themselves about the dissolved ions is directly proportional to the number of ions. Hence, we would expect ε_s to decrease linearly with increasing salinity. There are two commonly used frequency-domain models [37] and [38] of the permittivity of seawater. The older model [37] has been found to be more successful at reproducing water surface observations from low frequencies up to L-band frequencies [37]. According to this model, the relative permittivity of seawater at a temperature T (°C) and with salinity S (g/kg) is given by

$$\varepsilon = \varepsilon_\infty + \frac{(\varepsilon_1 - \varepsilon_\infty)}{1 - jf\,2\pi\tau} + \frac{j\sigma}{\omega\varepsilon_0}, \tag{73}$$

where ε_0 is the permittivity of free space, f is the frequency of the radiometer in Hertz, and

$$\begin{aligned}\varepsilon_1 = {} & (87.134 - 0.1949T - 0.01276T^2 + 0.0002491T^3) \\ & (1 + 1.613\times10^{-5}TS - 0.003656S + 3.21\times10^{-5}S^2 - 4.232\times10^{-7}S^3),\end{aligned} \tag{74}$$

$$\varepsilon_\infty = 4.9, \tag{75}$$

$$\begin{aligned}2\pi\tau = {} & (1.1109\times10^{-10} - 3.824\times10^{-12}T + 6.398\times10^{-14}T^2 - 5.096\times10^{-16}T^3) \\ & (1 + 2.282\times10^{-5}TS - 7.638\times10^{-4}S - 7.760\times10^{-6}S^2 + 1.105\times10^{-8}S^3),\end{aligned} \tag{76}$$

$$\sigma = S(.18252 - 0.0014619S + 2.093\times10^{-5}S^2 - 1.282\times10^{-7}S^3)$$
$$\exp((T-25)(0.02033 + 0.0001266(25-T) + 2.464\times10^{-6}(25-T)^2 \quad (77)$$
$$- S(1.849\times10^{-5} - 2.551\times10^{-7}(25-T) + 2.551\times10^{-8}(25-T)^2))).$$

2.9 Estimating a submerged object's location, orientation, and magnetic polarization from EMI data

In the low-frequency EMI regime considered here the primary magnetic field penetrates a metallic object to some (frequency-dependent) degree and induces eddy currents/magnetic dipoles within it. These induced currents and dipoles then produce a secondary or scattered field outside the object that is measured by a receiver. Using the magnetic dipole approximation we can write the magnetic field **H** and the scalar potential ψ as

$$\mathbf{H} = \frac{e^{jkR}}{4\pi R^3}\left[\left(\frac{3\mathbf{R}(\mathbf{R}\cdot\mathbf{m})}{R^2} - \mathbf{m}\right)(1 - jkR) - k^2(\mathbf{R}\times(\mathbf{R}\times\mathbf{m}))\right] \quad (78)$$

and

$$\psi = \frac{\mathbf{R}\cdot\mathbf{m}}{4\pi R^3}(1 - jkR)e^{jkR} \equiv \frac{\mathbf{R}\cdot\mathbf{m}}{R^3}G(R,k), \quad (79)$$

where k is the wave number in the surrounding medium, $\mathbf{R} = \mathbf{r} - \mathbf{r}_d$, and the vectors $\mathbf{r}$ and $\mathbf{r}_d$ are the observation point and the location of the source, which we assume to be a dipole (see Figure 2-7).

Note that, in the electromagnetic wave regime, the magnetic field (78) due to a magnetic dipole has terms that decay as R^{-1}, R^{-2}, and R^{-3}. The range $kR \gg 1$ is referred to as the far zone, and fields in this range are referred to as being in the far field. Similarly, fields in the near zone (with $kR \ll 1$) are referred to as being in the near field, while the zone $kR \approx 1$ is called the intermediate zone. Typically, UXO detection and discrimination are conducted in the near and intermediate zones during both land-based and underwater UXO cleanup. Additionally, in the EMI regime displacement currents are negligible, which means that the contribution of the k^2 term in (78) can be dropped. Under these assumptions we can take the dot product of (78) and **R** and use (79) to show that

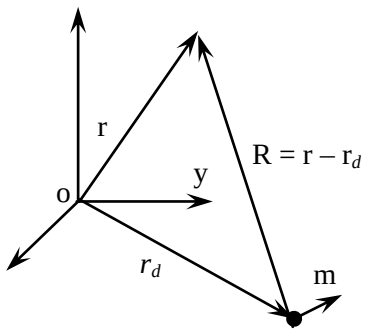

Figure 2-7: Geometry of the problem. The target is assumed to be a magnetic dipole located at r_d.

$$\mathbf{H}\cdot\mathbf{R} = \frac{1}{R^3}\left(\frac{3\mathbf{R}(\mathbf{R}\cdot\mathbf{m})}{R^2} - \mathbf{m}\right)\cdot\mathbf{R}\; G(R,k) = 2\frac{\mathbf{R}\cdot\mathbf{m}}{R^3}G(R,k) = 2\psi\,. \quad (80)$$

Recalling that $\mathbf{R} = \mathbf{r} - \mathbf{r}_d$, where $\mathbf{r}$ and $\mathbf{r}_d$ are respectively the observation point and the dipole location in the global coordinate system (see Figure 2-7), we can write (80) as

$$\mathbf{H} \cdot (\mathbf{r} - \mathbf{r}_d) = 2\psi \tag{81}$$

or

$$\mathbf{H} \cdot \mathbf{r}_d = -2\psi + \mathbf{H} \cdot \mathbf{r} \,. \tag{82}$$

If $\mathbf{r}_i$, $\mathbf{H}_i$, and ψ_i are known at several observation points $i = 1, \mathsf{K}, N$, equation (82) can be rewritten in matrix form as

$$\begin{bmatrix} H_{x,1} & H_{y,1} & H_{z,1} \\ H_{x,1} & H_{y,1} & H_{z,1} \\ \vdots & \ddots & \vdots \\ H_{x,N} & H_{y,N} & H_{z,N} \end{bmatrix} \begin{bmatrix} x_d \\ y_d \\ z_d \end{bmatrix} = \begin{bmatrix} -2\psi_1 + \mathbf{H}_1 \cdot \mathbf{r}_1 \\ -2\psi_2 + \mathbf{H}_2 \cdot \mathbf{r}_2 \\ \vdots \\ -2\psi_N + \mathbf{H}_N \cdot \mathbf{r}_N \end{bmatrix}, \tag{83}$$

allowing us to find $\mathbf{r}_d$. Under the low-frequency EMI assumption $k^2 \to 0$, (78) can be rewritten as

$$\mathbf{H}R^2 = G(R,k)\left[\left(3\mathbf{R}\psi - \mathbf{m}R^2\right)\right], \tag{84}$$

which lets us determine the induced magnetic dipole moment via

$$\mathbf{m} = \frac{R}{G(\mathrm{R})}\left(3\mathbf{R}\psi - \left[\mathbf{H}\, R^2\right]\right) \tag{85}$$

once we have determined **R** from (83). Thus the location $\mathbf{r}_d$ and the dipole moment **m** of a single isolated dipolar source can be uniquely determined from **H** and ψ. Since only **H** is a measurable quantity, the proposed formulation (82) can be rewritten in terms of the scattered magnetic field and its gradient by applying the gradient operator on both sides of (82) with respect to **r**, which reduces to

$$(\mathbf{r}_d \cdot \nabla)\mathbf{H} = 3\mathbf{H} + (\mathbf{r} \cdot \nabla)\mathbf{H} \,. \tag{86}$$

2.10 Generalized Standardized Excitation Approach for underwater EMI sensors

Recently, an SEA based on fictitious magnetic charges has been developed and applied to UXO discrimination using both frequency-domain and time-domain EMI data [17, 20-21]. In this section we present the GSEA [20], which is based on magnetic dipoles as responding sources and is thus applicable to conducting and magnetically susceptible host media, and study its time-domain version. Consider an object placed in free space and illuminated by an arbitrarily oriented, time-varying primary magnetic field. In the EMI frequency regime, displacement currents within and outside the object are assumed to be zero; i.e., both the primary and the scattered magnetic fields are irrotational. We surround the object with a fictitious spheroid, which is introduced only as a computational aid in the decomposition of the primary magnetic field into fundamental spheroidal modes. We choose prolate spheroids because they can assume the general proportions of objects of interest, such as UXO, which are typically elongated bodies of revolution (BOR). Oblate spheroids can also be used for flattened shapes. In general, the fictitious surface could be any smooth closed surface, as applicable for a related standardized source set approximation described in [17, 20-21]. On a fictitious spheroid given by $\xi = \xi_0$ [39], the primary magnetic field can be expressed as

$$\mathbf{H}^{\mathrm{pr}} = \sum_{m=0}^{\infty} \sum_{n=m}^{\infty} \sum_{p=0}^{1} b_{pmn} \mathbf{H}_{pmn}^{\mathrm{pr}} \,. \tag{87}$$

The b_{pmn} are coefficients needed to express the primary field, and the $\mathbf{H}_{pmn}^{\mathrm{pr}}$ is the *pmn* mode of the primary magnetic field component when $b_{pmn} = 1$. The spheroidal expansion coefficients b_{pmn} can be determined from the normal component of the primary magnetic field on the fictitious spheroid [20].

After the primary magnetic field is decomposed into the *pmn* spheroidal modes, the complete response of the target to each $\mathbf{H}_{\mathrm{pmn}}^{\mathrm{pr}}$ field can be obtained. Finally, the target's full response is

$$\mathbf{B}^{\mathrm{sc}}(\mathbf{r},t) \;=\; \nabla \times \sum_{m=0}^{\infty} \sum_{n=m}^{\infty} \sum_{p=0}^{1} b_{pmn} \mathbf{A}_{pmn}^{\mathrm{sc}}(\mathbf{r},t) = \nabla \times \mathbf{A}^{\mathrm{sc}}(\mathbf{r},t), \tag{88}$$

$$\mathbf{A}_{pmn}^{\mathrm{sc}}(\mathbf{r},t) = \frac{\mu_0}{4\pi} \int_{S_{\mathrm{sph}}} \frac{\mathbf{m}_{pmn}(\mathbf{r}',t) \times \mathbf{R}}{R^3} \, ds' \,, \tag{89}$$

where $\mathbf{A}_{pmn}^{\mathrm{sc}}$ is the *pmn* mode of the scattered vector potential, $\mathbf{A}^{\mathrm{sc}}(\mathbf{r},t)$ is the total scattered potential, $\mathbf{m}_{pmn}(\mathbf{r}',t)$ are the responding magnetic dipoles distributed on the fictitious spheroidal surface, **r** and **r'** are the radius vectors of the observation and source points respectively, and **R = r** – **r'**. Note that in the EMI range the secondary magnetic field is irrotational, which means that the scattered field propagates outside the object instantaneously; *i.e.*, there is no time delay in equation (88). By using the Green's function, the scattered magnetic field is approximated by the response of a set of magnetic dipoles oriented normally to the fictitious spheroidal surface:

$$\mathbf{m}_{pmn}(\mathbf{r}',t) = M_{pmn}(\mathbf{r}',t) \cdot \hat{\mathbf{n}}(\mathbf{r}') \,, \tag{90}$$

where $\hat{\mathbf{n}}(\mathbf{r}')$ is the normal unit vector at point $\mathbf{r}'$ on the spheroidal surface and the $M_{pmn}(\mathbf{r}',t)$ are the amplitudes of the responding sources. A TD sensor measures the time derivative of the magnetic flux through the receiver coil:

$$\text{Signal} = \int_{S_r} \frac{\partial \mathbf{B}^{\text{sc}}(\mathbf{r},\text{t})}{\partial t} ds' = \frac{\partial}{\partial t} \int_{S_r} \text{rot}\, \mathbf{A}^{\text{sc}}(\mathbf{r},\text{t}) ds' = \frac{\partial}{\partial t} \oint_L A_\ell^{\text{sc}}(\ell',\text{t}) d\ell' . \tag{91}$$

Inserting equations (88) and (90) into (91),

$$\text{Signal} = \oint_L \left[\sum_{m=0}^{\infty} \sum_{n=m}^{\infty} \sum_{p=0}^{1} b_{pmn} \int_{S_{sph}} \frac{\partial M_{pmn}(\mathbf{r}',t)}{\partial t} \cdot \mathbf{G}(\mathbf{r}',\mathbf{r}) ds' \right] \text{d}\ell' \tag{92}$$

is obtained, where

$$\mathbf{G}(\mathbf{r}',\mathbf{r}) = \frac{\mu_0}{4\pi} \frac{\hat{\mathbf{n}}(\mathbf{r}') \times \mathbf{R}}{R^3} \tag{93}$$

and the $\partial M_{pmn}(\mathbf{r}',t)/\partial t = M'^{pmn}(\mathbf{r}',t)$ are the time derivatives of the amplitudes of the responding magnetic dipoles that need to be determined from the measured data.

Since many if not all UXO are bodies of revolution (BOR), it is desirable to simplify equation (92) for BOR objects. After dividing the fictitious spheroid surface into *J* belts and taking into account the BOR symmetry of the object, the amplitude of the responding $M'^{pmn}(\mathbf{r}',t)$ source around the j^{th} belt can be expanded into a Fourier series with respect to the azimuthal angle φ, and equation (92) can be rewritten as

$$\text{Signal}(\mathbf{r}) = \oint_L \left[\sum_{m=0}^{\infty} \sum_{n=m}^{\infty} \sum_{j}^{J} M'^{\,mn}_{j}(\rho_j,t) \sum_{p=0}^{1} \int_{\Delta S_{\text{sph}}^{j}} (b_{0mn}\cos(m\varphi) + b_{1mn}\sin(m\varphi)) \cdot \mathbf{G}(\mathbf{r}_j',\mathbf{r}) ds' \right] \text{d}\ell' . \tag{94}$$

Finally, the EMI scattered fields from all *J* belts are set to equal the measured signal at a point $\mathbf{r}$ where the secondary field arising from the scatterer is known. For $\mathbf{r}_k$, $k = 1,2,\text{K}\,,K$ points, equation (92) leads to a linear system of equations that can be solved using a least-squares minimization algorithm.

2.11 Modeling the water surface

Two sets of simulations were conducted with the source of electromagnetic waves being (a) a square loop in *xy* plane, located above the water surface, and (b) a single *x*-oriented magnetic dipole located underwater. Qualitatively the interaction between the source fields with the rough surface does not significantly depend on the nature of the source, and, therefore, only the results corresponding to the first scenario are discussed below. The level *z* = 0.0 m was assumed to be the elevation of the unperturbed water surface.

The water surface was simulated as an interference pattern from a number of surface waves of variable amplitude, wavelength, propagation direction and phase. A flat hexagonal grid was first created to provide a uniform distribution of collocation points on the *xy*-plane, which is beneficial for numerical simulations (Figure 2-8). Then a finite set of surface waves was applied to elevate or lower the water surface, and the resulting height map was normalized to fit the predefined wave height, defined as $h = 2\max(|z(x,y)|)$.

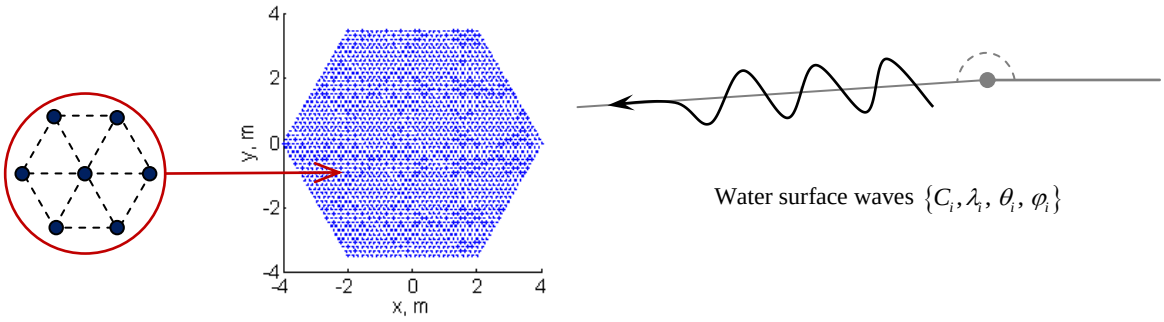

Figure 2-8: Initial flat water surface with uniformly distributed collocation points and a sample surface perturbation.

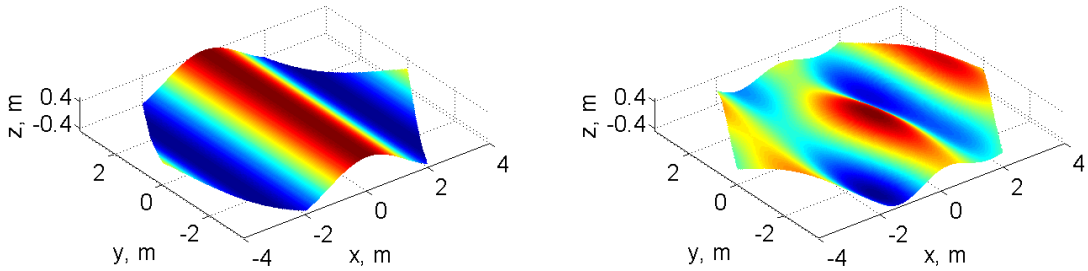

Figure 2-9: Simulated water surface in different cases.
(Left) Single cosine perturbation; (Right) Interference between three surface waves in the xy-plane having the relative amplitudes C_1=1, C_2=0.7, C_3=0.3, wavelengths of $\lambda_1 = 3$ m, $\lambda_2 = 4$ m, $\lambda_3 = 5$ m, and propagating at angles of $\theta_1 = 0°$, $\theta_2 = 30°$ and $\theta_3 = 90°$ with respect to the x-axis.

The final surfaces, shown on Figure 2-9, are given by

$$z(x,y) = \sum_{i=1}^{N} C_i \cos\left(\frac{2\pi}{\lambda} \left(x\cos\theta_i + y\sin\theta_i \right) + \varphi_i \right), \tag{95}$$

$$z(x,y) = z(x,y) \cdot \frac{h}{\max(|z(x,y)|)}. \tag{96}$$

Finally, the surface tangents $\mathbf{u}, \mathbf{v}$ (and, therefore, the normals $\mathbf{n} = \mathbf{u} \times \mathbf{v}$) for every surface collocation point were evaluated using

$$\mathbf{u} = \mathbf{e}_x \cos\left(\arctan\left(\frac{\partial z(x,y)}{\partial x} \right) \right) + \mathbf{e}_z \sin\left(\arctan\left(\frac{\partial z(x,y)}{\partial x} \right) \right), \tag{97}$$

$$\mathbf{v} = \mathbf{e}_y \cos\left(\arctan\left(\frac{\partial z(x,y)}{\partial y} \right) \right) + \mathbf{e}_z \sin\left(\arctan\left(\frac{\partial z(x,y)}{\partial y} \right) \right). \tag{98}$$

Since in the low-frequency regime the EM field wavelength is much greater than the characteristic length of the structure of interest (λ : 300 m for f ~ 1 MHz, while the water surface wave wavelength ~1 m, height ~1 m, source UXO depth ~1 m, sensor array horizontal extent ~1 × 1 m) the only guiding principle for the number of collocation points is that they should describe the water surface roughness in sufficient detail. Even though the initially uniform collocation point distribution on the water

surface is slightly perturbed by the oncoming surface waves, the resulting quasi-uniform distribution is still sufficient for effective use of the Method of Auxiliary Sources. The total number of collocation points in our simulations was on the order of 2400, with the ocean surface being a hexagonal grid having a total side length of 4 m. It was found that even for such a small lateral extent the contributions from the edges of the surface may be neglected, due to the rapid decay of the magnetic fields with distance from the source. Figure 2-9 shows sample water surface realizations in case of interference of three surface waves. The corresponding auxiliary surfaces are obtained from the final water surface by shifting along the normals at the corresponding collocation points. The auxiliary sources are then placed along the surface tangents **u, v** both under and above the water.

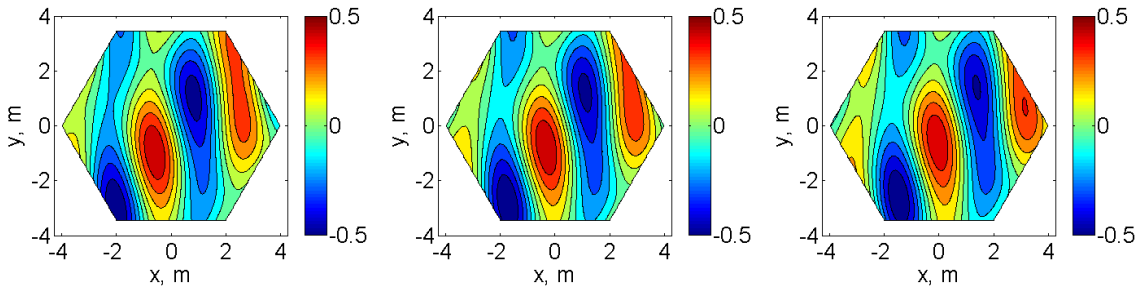

Figure 2-10: Water surface height realizations at different times.
Result of interference from the three surface waves as in Figure 2-8. The color map indicates the height in meters.

3 Numerical results

In this section we present numerical and experimental results for induced secondary magnetic fields from various objects subjected to excitation by different primary magnetic fields in both frequency and time domains. The numerical experiments are designed to demonstrate the interaction effects between a highly conducting and permeable metallic object and its surrounding conducting medium. The examples show the accuracy of the MAS and SIBC method and its considerable potential for understanding in detail the fundamental phenomenology of EMI scattering in underwater environments.

In particular, we first examine scattering from a permeable and highly conducting sphere; the computed results are compared with analytical values and experimental data. Next we consider EMI scattering from a conducting half-space, and after that we present numerical results for permeable and conducting spheroids, cylinders, and pipes. In this connection, we explore how trends in the secondary magnetic field depend on the object's elongation, electromagnetic parameters (permeability, frequency), and orientation, and on the distance between sensor and object. The method is also applied to an actual 105-mm heat-round UXO to demonstrate the effects of heterogeneity. Finally we analyze near-field distributions. Our simulations agree very well with actual GEM-3D data. Both experiment and numerical solutions show that an object's EMI signal increases at high frequencies, an increase associated with the electric field. These effects depend on the distance between the object and sensor.

3.1 MAS code validation

First the accuracy of the MAS/TSA technique is checked for a sphere placed in a conductive medium. A comparison between MAS/TSA and analytic data is shown in Figure 3-1 for a non-permeable sphere of radius a = 5 cm and conductivity $\sigma = 10^7$ S/m placed in a uniform space of conductivity 4 S/m and illuminated by a uniform time-varying primary magnetic field directed along the z-axis. Comparisons are given for two observation points (10 cm and 15 cm above the center of the sphere). The magnetic fields are normalized so their quadrature parts peak at unity. These results show that the numerical (MAS/SIBC) and analytical results are in excellent agreement, demonstrating the validity of both approaches for metallic objects placed in a conducting space. Figure 6 shows that the strong interaction between the sphere and its surrounding space occurs mostly at high frequencies. Both the inphase and the quadrature parts change as a result of the interaction: the inphase part turns toward zero and the quadrature part changes sign at high frequency as the response from the water becomes dominant. Results also show that the interaction depends on the observation point. For instance, Figure 3-1 shows that, as the observation distance from the sphere increases, the interaction between the object and the host medium shifts toward lower frequencies.

The accuracy of the MAS/SIBC code is checked again for a permeable sphere placed in conductive salt water. The numerical results are compared against actual data collected by Geophex personnel under SERDP Project MM1321. Comparisons between actual and modeled data are depicted in Figure 3-2. In panel (a) the sensor is 25 cm directly above the sphere; in panel (b) it is at the same elevation and offset 50 cm to the side.

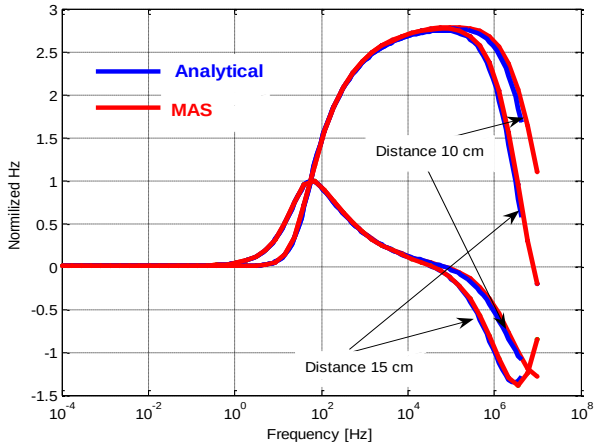

Figure 3-1: Normalized scattered magnetic field versus frequency for a sphere.

These results clearly show that the numerical (MAS/SIBC) code predicts the sphere's EMI responses very accurately for both cases, demonstrating the validity of the proposed approach for metallic objects placed in a conducting space. Figure 3-1 and Figure 3-2 shows that in general a sphere's EMI response as a function of frequency is similar for both uniform and GEM-3D-type sensor excitations. On the other hand, a glance at Figure 3-2(a) and Figure 3-2(b) reveals that the scattered EMI field from a sphere depends strongly on the lateral distance between the scatterer and the center of the GEM-3D. Again we see that there are strong interactions between the sphere and its surrounding space, occurring mostly at high frequencies. As the frequency increases beyond 10 kHz both inphase and quadrature parts increase significantly compared their free-space counterparts; the signal then changes sign and finally approaches zero. The increase in the response is associated with the electric field and will be illustrated when we look at near-field distributions; the signal's decay to zero is associated with the skin effect inside the conducting water. The signal's increase between 10 kHz and 1 MHz indicates that in this frequency range the signal-to-noise ratio is higher than for the same items in air; this fact can in principle be used to detect deep targets.

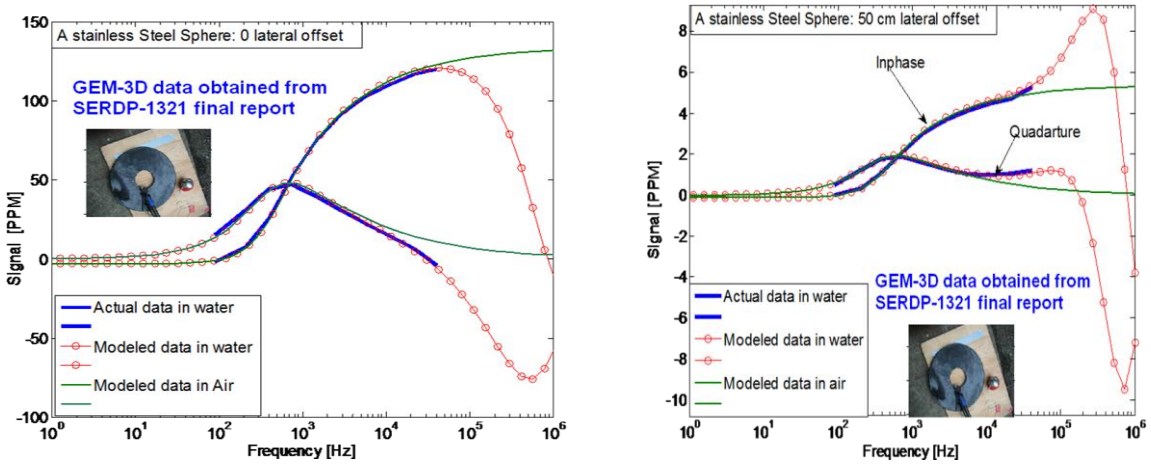

Figure 3-2: MAS/SIBC results and actual data for a sphere with the sensor at (a) zero and (b) 50-cm lateral offsets.

3.2 Effect of a water/air interface on low-frequency EMI field sensors

Here we investigate how the water/air interface changes the primary EMI field inside the conducting medium. The water is treated as a conducting half-space. The studies are done for the GEM-3D sensor placed 10 cm above the conducting half space. The GEM-3D sensor consists of two concentric transmitter loops (see cross-section in Figure 3-3). The currents in these loops circulate in opposite directions and are scaled so that the total primary field vanishes at the common center, where a receiving coil is located. The transmitter loops are idealized as infinitely thin line sources of radii a_1 and a_2 with currents $I_2 = -I_1 a_2/a_1$. We choose an observation point at the center of the sensor to demonstrate the reflection effect of a conducting half space and two observation points inside the conducting half-space to illustrate how the primary field changes within the conductive ground.

Figure 3-4 shows as a function of frequency the scattered magnetic field of a conducting half-space for different values of the conductivity. The scattered magnetic field from the conductive half-space is seen to increase at high frequencies, and as the conductivity of the medium increases the effect starts to be noticeable at lower frequencies. Similarly, Figure 3-5 shows the transmitted primary magnetic field inside the conductive half-space as a function of frequency. As the conductivity of the half-space increases the transmitted magnetic field inside the medium decreases due to the skin depth, and the absorption is much stronger as the depth increases; see Figure 3-5. In addition, the right panel of Figure 3-5 shows that the transmitted field changes sign at high frequencies, indicating that inside the conducting medium the EMI signal behaves like a wave.

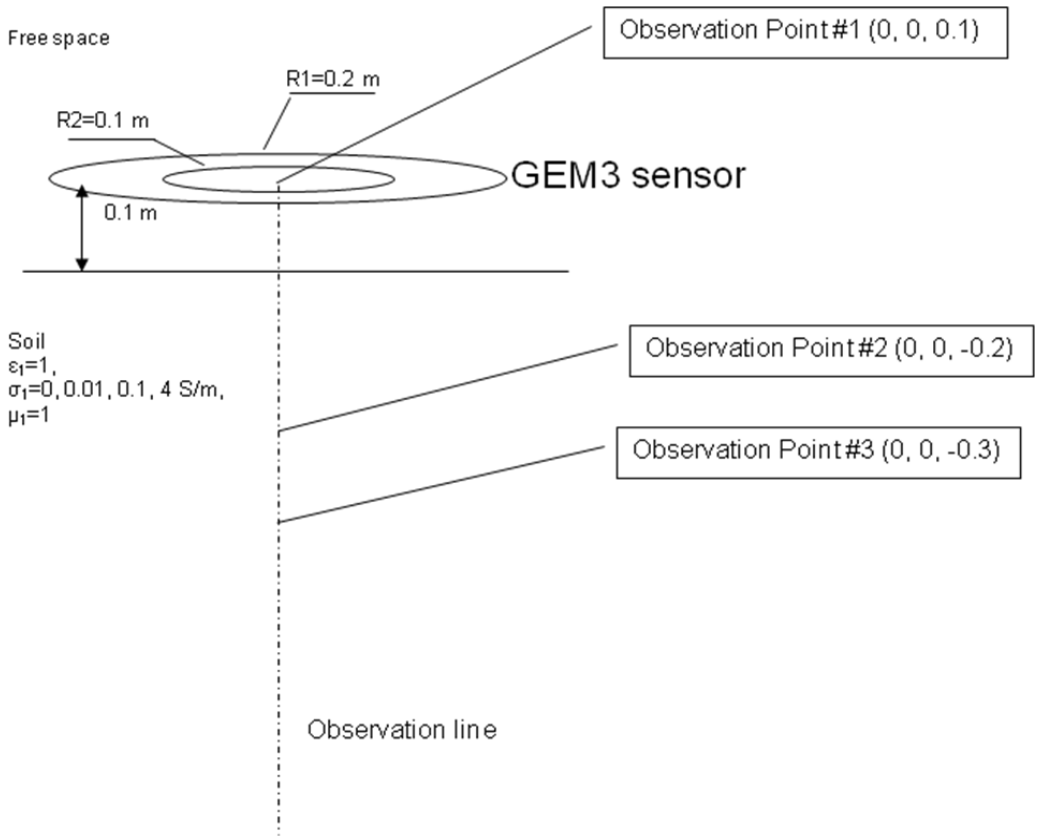

Figure 3-3: EMI reflection and refraction from the water/air interface as seen by the GEM-3D sensor.

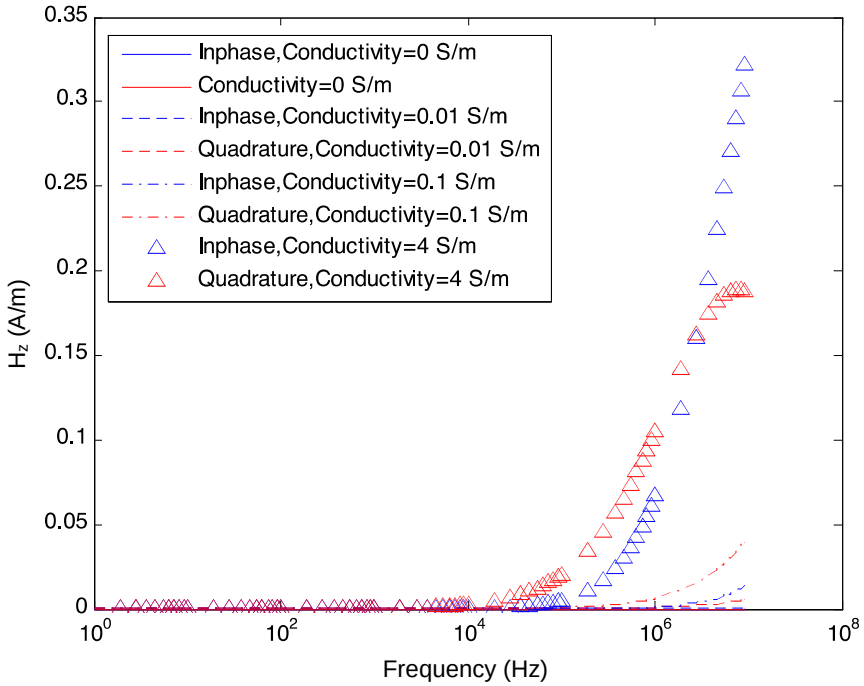

Figure 3-4: Scattered magnetic field vs. frequency for a conducting half-space illuminated by an EMI sensor.

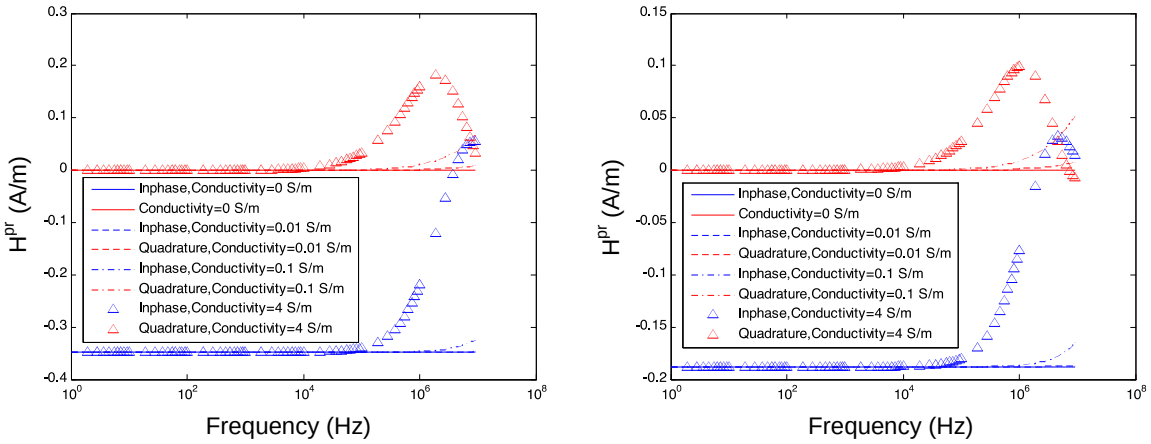

Figure 3-5: Transmitted primary magnetic field versus frequency inside the half-space for the EMI sensor at the two observation points of Figure 3-3.
(Left) Depth –0.2 m;
(Right) Depth –0.3 m.

Finally, we studied the primary magnetic field distribution inside and outside the conducting half-space at a frequency of 100 kHz. The results, depicted in Figure 3-6, show that as the conductivity increases the quadrature part of the transmitted primary magnetic field increases, whereas the inphase part does not change with conductivity at that frequency.

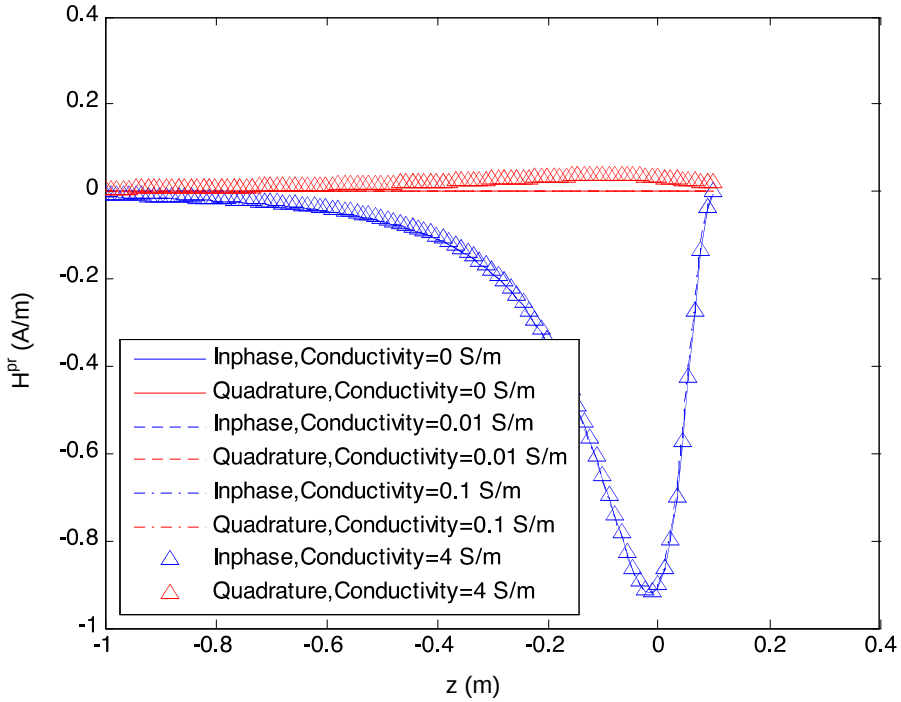

Figure 3-6: Primary magnetic field inside the conducting half-space along the line right below the sensor center for different half-space conductivities. The frequency is 100 kHz.

3.3 Interaction between the sensor and the surrounding conducting medium

Next, to illustrate the applicability of the MAS/TSA procedure for modeling state-of-the-art EMI sensors placed underwater we study the interaction between the Geophex GEM-3 frequency-domain sensor and a conductive host medium. Obviously the sensor electronics need to be protected from the water; this can be achieved by putting the sensor in a box (Figure 3-7). For this demonstration we take a box of diameter 60 cm and height 5 cm; the surrounding medium has $\mu_r = 1$ and conductivity $\sigma = 1$, 5 and 10 S/m.

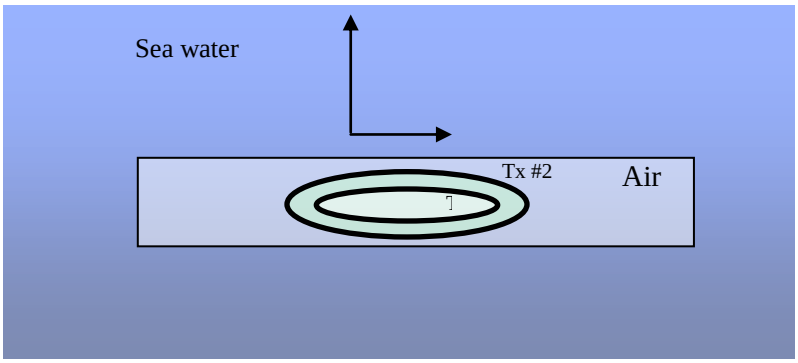

Figure 3-7: Schematic diagram on the *x*-*z* plane ($y = 0$) of the GEM-3 sensor placed under water.

The secondary magnetic fields as a function of frequency for the three different conductivities are shown in Figure 3-8 (left: inphase part; right: quadrature part). The results show that as the conductivity of the water increases the response of the surrounding medium shifts towards lower frequencies, as expected. In addition, for conducting seawater with $\sigma = 1$ S/m the frequency response of the host medium is negligible within the GEM-3 frequency range (30 Hz up to 50 kHz); however, for higher conductivities (5 and 10 S/m) the responses can be significant. This means that the surrounding medium produces additional noise that will decrease the signal-to-noise ratio and will complicate discrimination. Therefore, to improve the detection of underwater metallic objects and to better discriminate UXO from non-UXO items in marine environments using high frequency (>50 kHz) we have to take into account the interaction between the sensor and its surrounding medium.

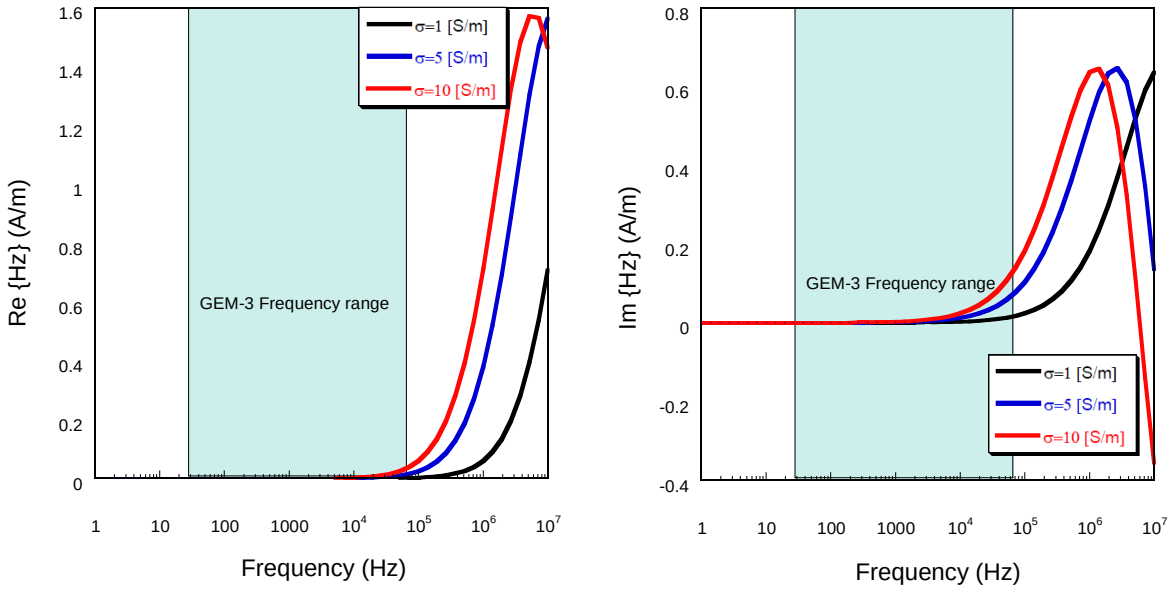

Figure 3-8: Scattered magnetic field versus frequency: (Left) Inphase part; (Right) Quadrature part.

3.4 Interaction between a metallic object and a conducting host medium: elongation and distance effects

3.4.1 A sphere

In this section we apply the MAS/SIBC to a highly conducting and permeable sphere placed in a conductive medium and illuminated with the GEM-3 sensor. Our aim is to illustrate how an underwater object's EMI response depends on the distance between sensor and object. Figure 3-9 shows the EMI response for a sphere of radius $a = 5$ cm, conductivity 4×10^6 S/m, and relative permeability 100 placed both in a uniform medium with $\sigma = 4$ S/m conductivity and in non-conductive/free space. The sensor is placed at three different locations: $L = 0$, 50, and 75 cm. The figure clearly demonstrates the existence of significant interactions between the object and the surrounding conductive medium, particularly at high frequency. In addition, the results show that this interaction depends on the distance between the object's center and the sensor. In particular, we see that when the sensor is just above the object both inphase and quadrature parts decrease after 10 kHz; on the other hand, for $L = 50$ cm and $L = 75$ cm both parts first increase and then start to decrease again. These phenomena have been observed experimentally [24].

3.4.2 A spheroid

Similar tests were done for an elongated metallic object, a prolate spheroid with major and minor axes *b* and *a*, aspect ratio *b/a*=3, and *a*=5cm. The results are depicted in Figure 3-10. In this simulation the spheroid was oriented horizontally. Overall, the results for the spheroid are similar to those for the sphere; however, the interaction effect when the spheroid is under the GEM-3 with L_y = 75 cm is much more significant, compared to the free-space EMI response, than that for the case with L_x= 75 cm. This result illustrates that there is a significant orientation effect in underwater environments at high frequencies that has to be taken into account during sensor development and when performing UXO discrimination.

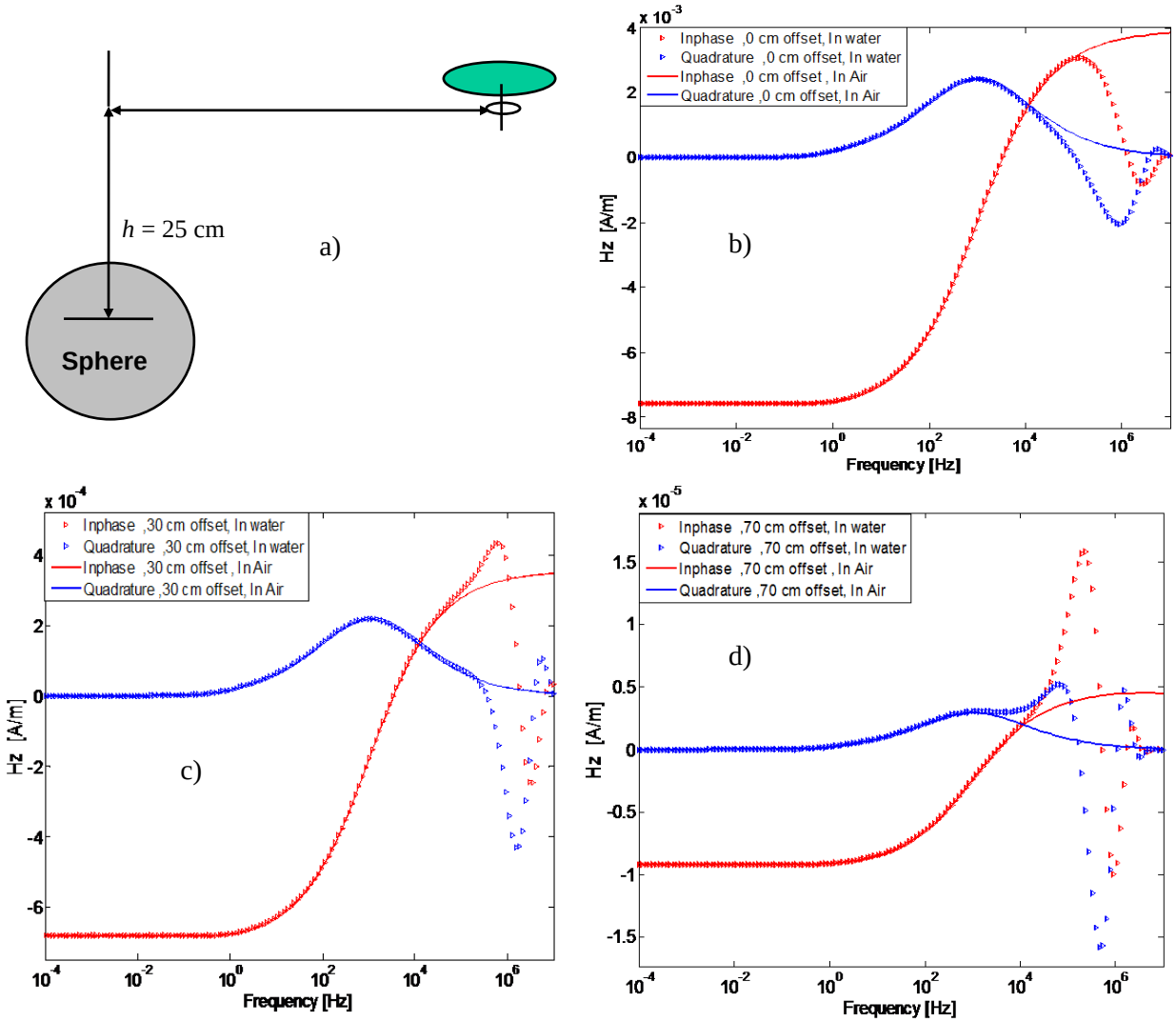

Figure 3-9: Scattering from a highly conducting and permeable sphere. b, c, d) EMI responses of the sphere illuminated by the GEM-3 sensor placed at different locations: L = 0, 30 and 70 cm.

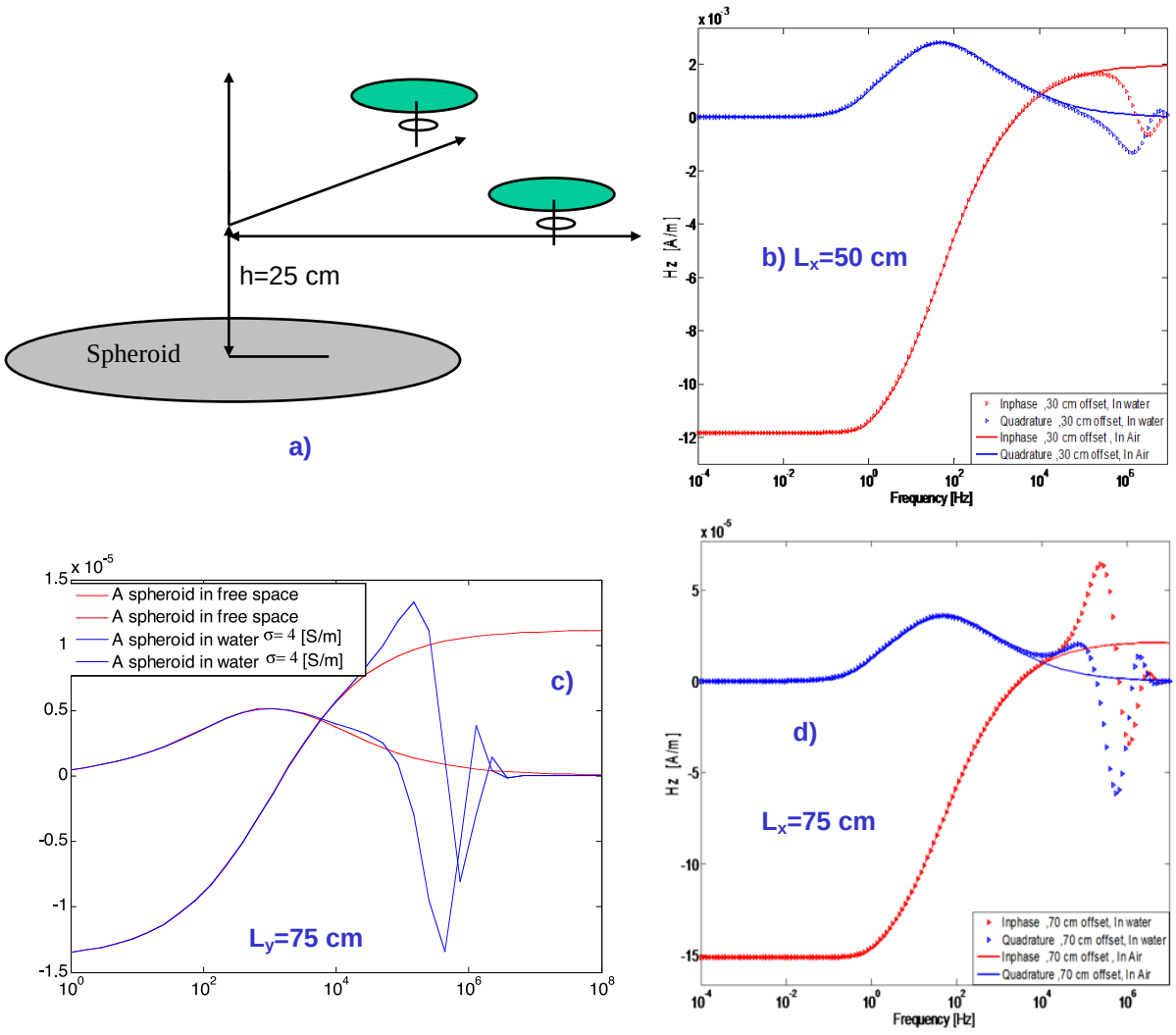

Figure 3-10: EMI response of a prolate spheroid with conductivity 4×10^6 S/m and permeability $\mu_r = 100$ illuminated with the GEM-3 sensor when placed at three locations: b) ($L_x = 50$ cm, $L_y = 0$), d) ($L_x = 75$ cm, $L_y = 0$), c) ($L_x = 0$, $L_y = 75$cm).

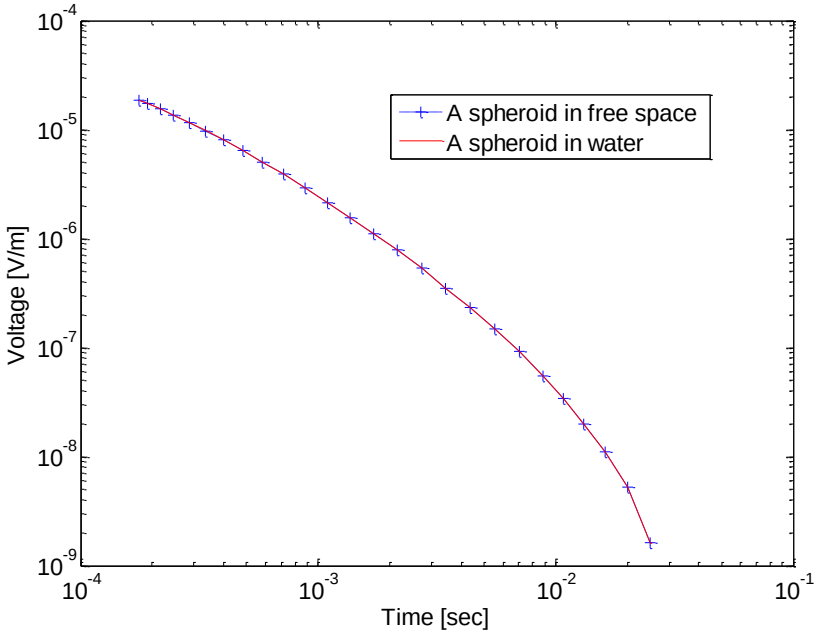

Figure 3-11: Time-domain EMI response of a prolate spheroid with conductivity 4×10^6 S/m and permeability 100, illuminated with the EM-63 sensor placed at location L_y = 75 cm.

3.5 Time-domain analysis inside

We now investigate time-domain EM scattering by considering a spheroid subject to excitation by the Geonics EM-63 sensor [3]. The sensor consists of a 1 m × 1 m square transmitter loop and two receiver loops: (1) a main receiver loop 0.5 m × 0.5 m in size whose center coincides with the center of the transmitter coil, and (2) a receiver loop of the same size located 60 cm above the main receiver coil. These receivers accurately measure the complete transient response over a wide dynamic range of time from 180 μs to 25 ms.

The MAS/SIBC can produce a target's ultra-wideband frequency response, and therefore a frequency-domain signal determined with our method can be used directly to obtain an object's TD EMI response via the convolution theorem. It is not necessary to recalculate the amplitudes of the responding sources. Given a general current waveform $I(t)$ flowing in a transmitter loop we get the following time-dependent induced voltage in the receiver:

$$\frac{dB}{dt} = -\int_0^t A'(t-\tau) I'(\tau)\, d\tau - A(0) I'(t) - A'(t) I(0)\,, \tag{96}$$

where $A(t)$ represents an object's impulse response and the prime denotes the derivative with respect to the time t. Equation (96) represents the TD response of an object to a general excitation current $I(t)$.

As an example we calculate time-domain data for the horizontal spheroid described above buried at a depth 25 cm below the sensor. The sensor's center is offset 75 cm from the spheroid's center. The EMI responses are calculated for the spheroid placed in free space and in a uniform conductive medium. Figure 3-11 compares the two EMI responses over the EM-63 time window, which ranges from 180 μs to 25 ms; the two are seen to be virtually the same. On the other hand, Figure 3-12 compares the impulse responses of a sphere over a wider time range, and Figure 3-13 does the same for a spheroid. The calculated impulse responses for these targets over a wider time frame exhibit substantial differences for

sensors at different lateral offsets, particularly at early times (which cannot be readily reached by current sensors).

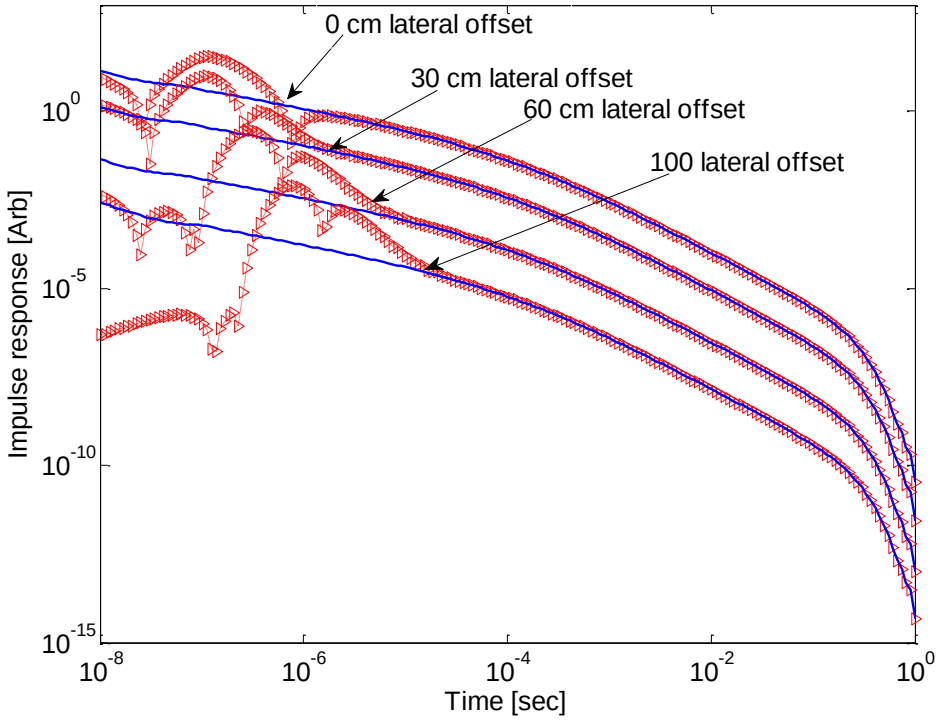

Figure 3-12: Impulse EMI response of a sphere with conductivity 4×10^6 S/m and relative permeability 100, illuminated with the EM-63 time-domain sensor placed at different locations. Blue lines: the sphere is located in the free space; red dot/triangular lines: the sphere is placed in 4 S/m conducting space.

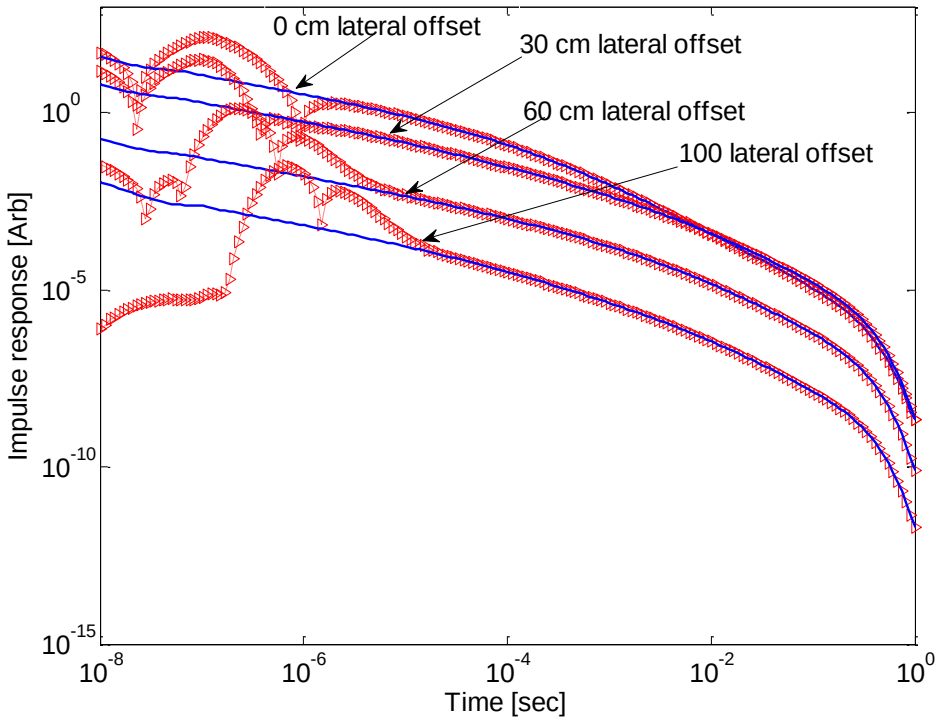

Figure 3-13: Impulse EMI response of a prolate spheroid with conductivity 4×10^6 S/m and permeability 100, illuminated with the EM-63 time-domain sensor placed at different locations. Blue lines: the spheroid is located in the free space; red dot/triangular lines: the spheroid is placed in 4 S/m conducting space.

3.6 EMI scattering from a UXO

Most if not all UXO are heterogeneous objects consisting of different metallic sections. In order to better understand EMI scattering of realistic objects in UW environments, in this section we consider an actual 105-mm heat-round UXO. We first infer the object's electromagnetic parameters from actual EMI data and then use those to calculate EMI responses over a wideband frequency regime. The results are shown in Figure 3-14. The object was illuminated with a GEM-3D sensor placed at $L_x = -75$ and $L_x = 75$ cm. The object's EMI responses are seen to be significantly different for the two sensor placements; moreover, the underwater signal increases significantly at high frequency in comparison to its free-space equivalent. The frequency responses of both inphase and quadrature parts rise significantly when the object is placed in a conductive medium. Overall, the details of this change may provide clues to both target heterogeneity and aspect ratio during UW detection and discrimination. More detailed examination of the peaks and curves that characterize these signals at high frequency—e.g., in terms of width and symmetry of the peak—may also provide information on details of target structure.

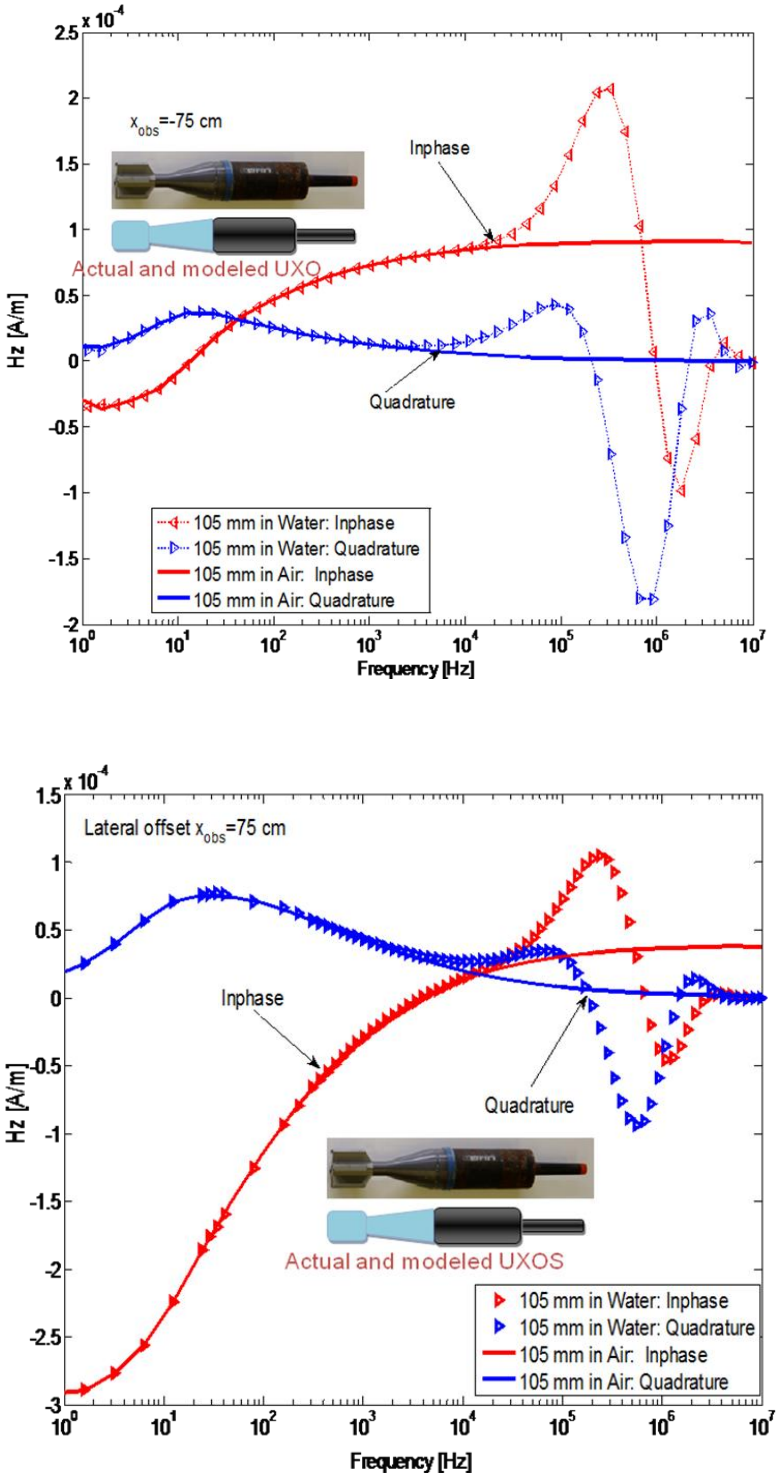

Figure 3-14: EMI response for a 105-mm UXO.
The object consists of four different metallic parts. The conductivity and magnetic permeability of each part were determined from measured data using an nonlinear inverse scattering algorithm based on the MAS.

3.7 EMI responses from hollow objects: thickness effects

We present another example that illustrates the effect of an object's thickness. In particular, in this section we study the EMI response from highly conducting and permeable pipes, which are filled with water and have different wall thicknesses. The pipe, with inner diameter 5 cm, length 5.7 cm, conductivity $\sigma = 4 \times 10^6$ S/m and permeability μ_r = 100, is placed under the primary field of the GEM-3D sensor (Figure 3-15(a)). The other panels depict the scattered magnetic field as a function of frequency when the pipe is placed in free space and inside the conductive space. The results illustrate the strong high-frequency coupling between the conducting host medium and the pipe and how this interaction depends on the pipe's wall thickness.

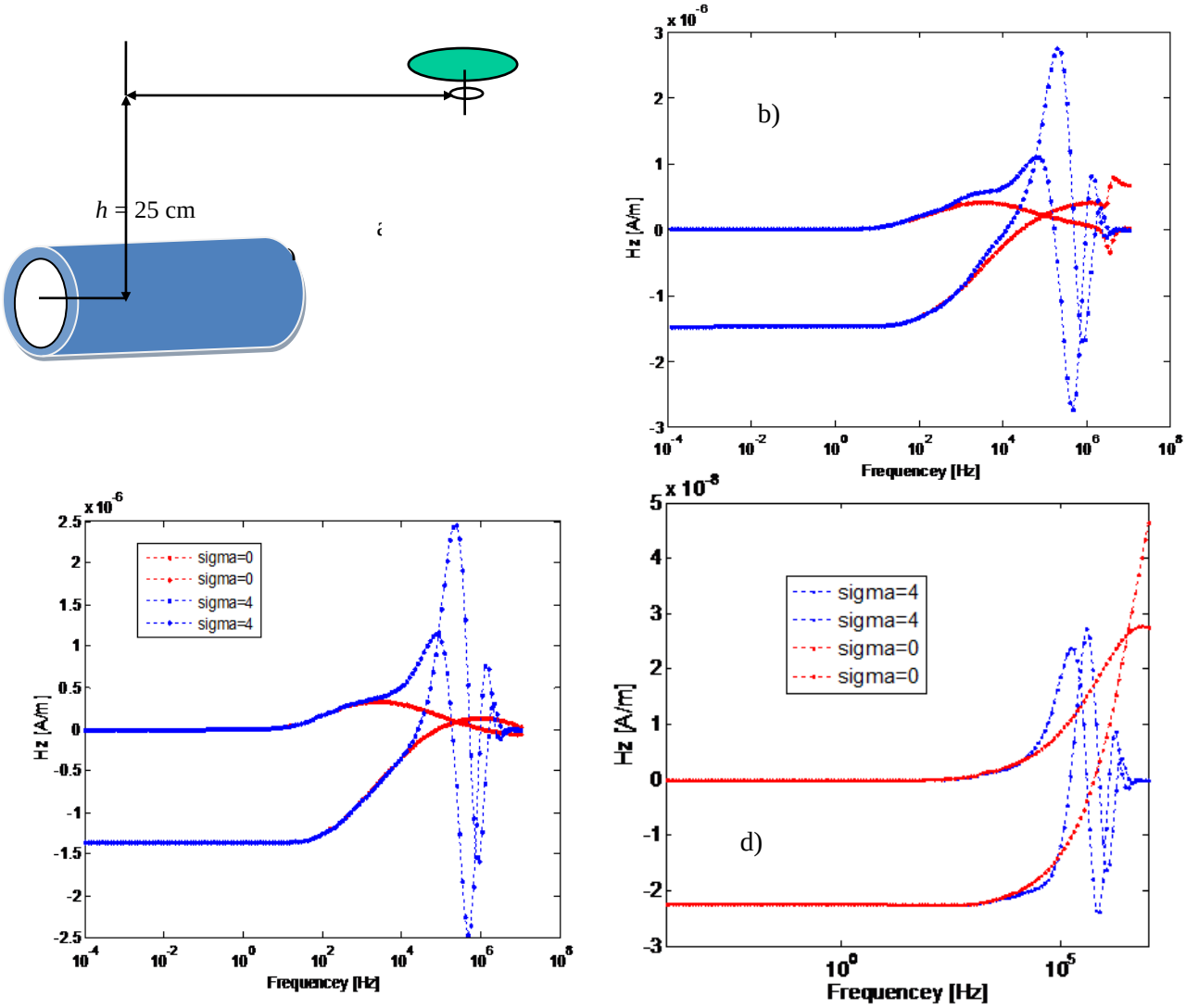

Figure 3-15: Scattering from a highly conducting and permeable pipe with 5 cm inner diameter and 5.7 cm length. The pipe is illuminated by the GEM-3D sensor placed at L_x=75cm. Pipe thicknesses are b) 10 mm, c) 5 mm, and d) 1 mm.

3.8 Eddy-current analysis

In order to understand the underlying physics of EMI scattering phenomena inside a conducting medium, here we investigate the distribution of eddy currents for a sphere under the GEM-3D primary field at a frequency of 20 kHz. The sensor is placed 25 cm above and 60 cm (and 75 cm) to the side of the sphere's center (see Figure 3-9). The sphere has conductivity 4×10^6 S/m and relative permeability 100. We used the full MAS technique to investigate the field distribution inside and outside the sphere. We needed 150 auxiliary sources along the generating arc and performed the simulation using the azimuthal modes with $m = 0, 1, ..., 5$ (see the section on BOR implementation). Figure 3-16 shows the eddy-current distributions inside and outside the sphere when it is placed in free space and within a conducting medium. We see that in both cases the eddy current distributions are the same. In the EMI frequency regime the induced current density is a divergenceless quantity, and therefore its normal component is continuous across a boundary. This indicates that the contribution from surface eddy currents dominates the scattered EM field.

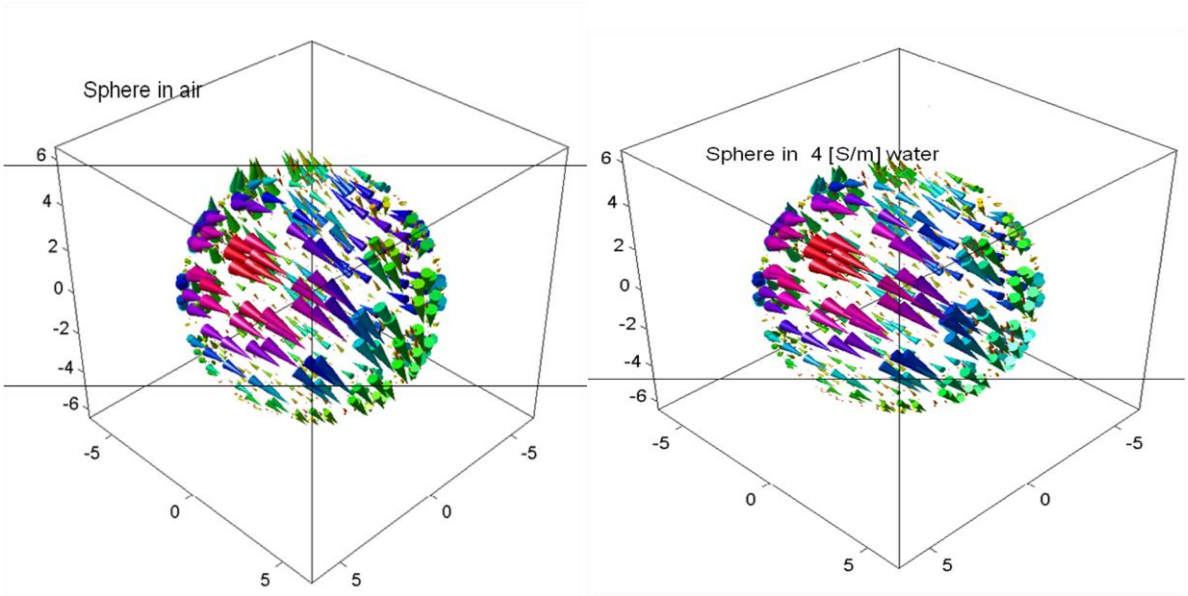

Figure 3-16: Induced eddy-current distributions inside and outside a sphere placed in air (Left) and within a 4-S/m conducting space (Right).
The distributions are computed using the full MAS at a frequency of 20 kHz.

3.9 Near-field analysis

In this section we present a near-field analysis to provide an understanding of the interaction phenomena between a metallic object and its surrounding conducting host medium. Figure 3-17, Figure 3-18 and Figure 3-19 show the real and imaginary parts of the total field distributions at frequency 20 kHz inside and outside a highly conducting and permeable sphere (Figure 3-17: E_y; Figure 3-17: H_x; Figure 3-18: H_z). The EM and geometric parameters are the same as for Figure 3-10. The sphere is illuminated by the primary magnetic field of the GEM-3D sensor. The results show that when the sphere is placed in free space the real part of the total electric field and the imaginary parts of the magnetic-field components are less significant than when the sphere is placed inside a conducting medium. This is because inside the conducting medium the electric and magnetic fields are comparable and behave like an EM wave. The primary electric and magnetic fields contribute equally to the scattered EM response. Thus as the frequency increases the EMI scattering becomes progressively more like EM wave phenomena, and the scatterer's EMI response increases. These results also show that as the sensor is offset laterally the

electric field illuminates the entire object and induces all components. This could explain why a lateral offset creates bigger EMI responses.

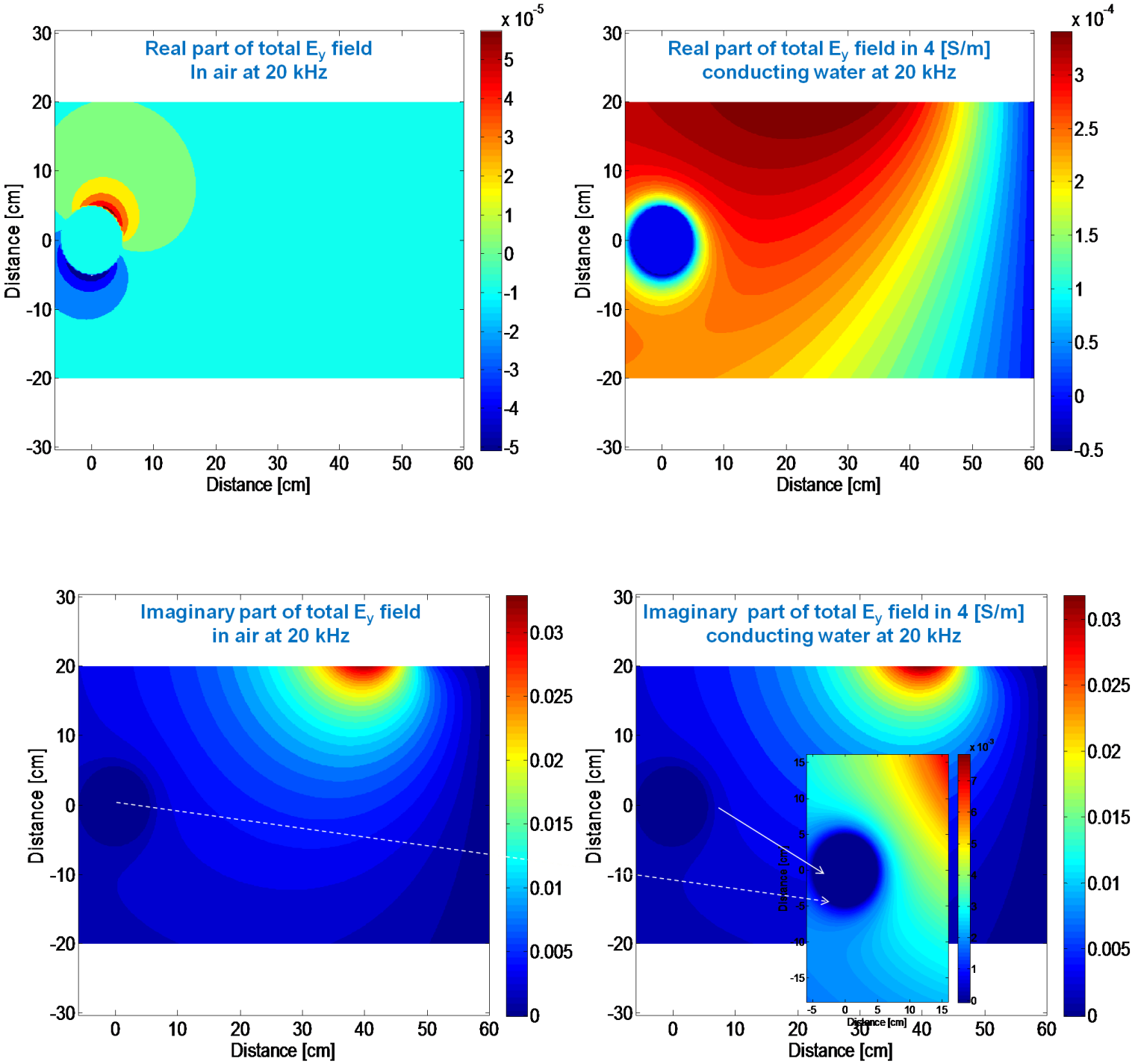

Figure 3-17: Total E_y electric field distributions inside and outside a sphere of radius 5 cm placed in air (left column) and in conducting water (right column).
(Top: inphase part; bottom: quadrature part.) The sphere is illuminated with a GEM-3D sensor placed 25 cm above and 60 cm to the side of the sphere's center.

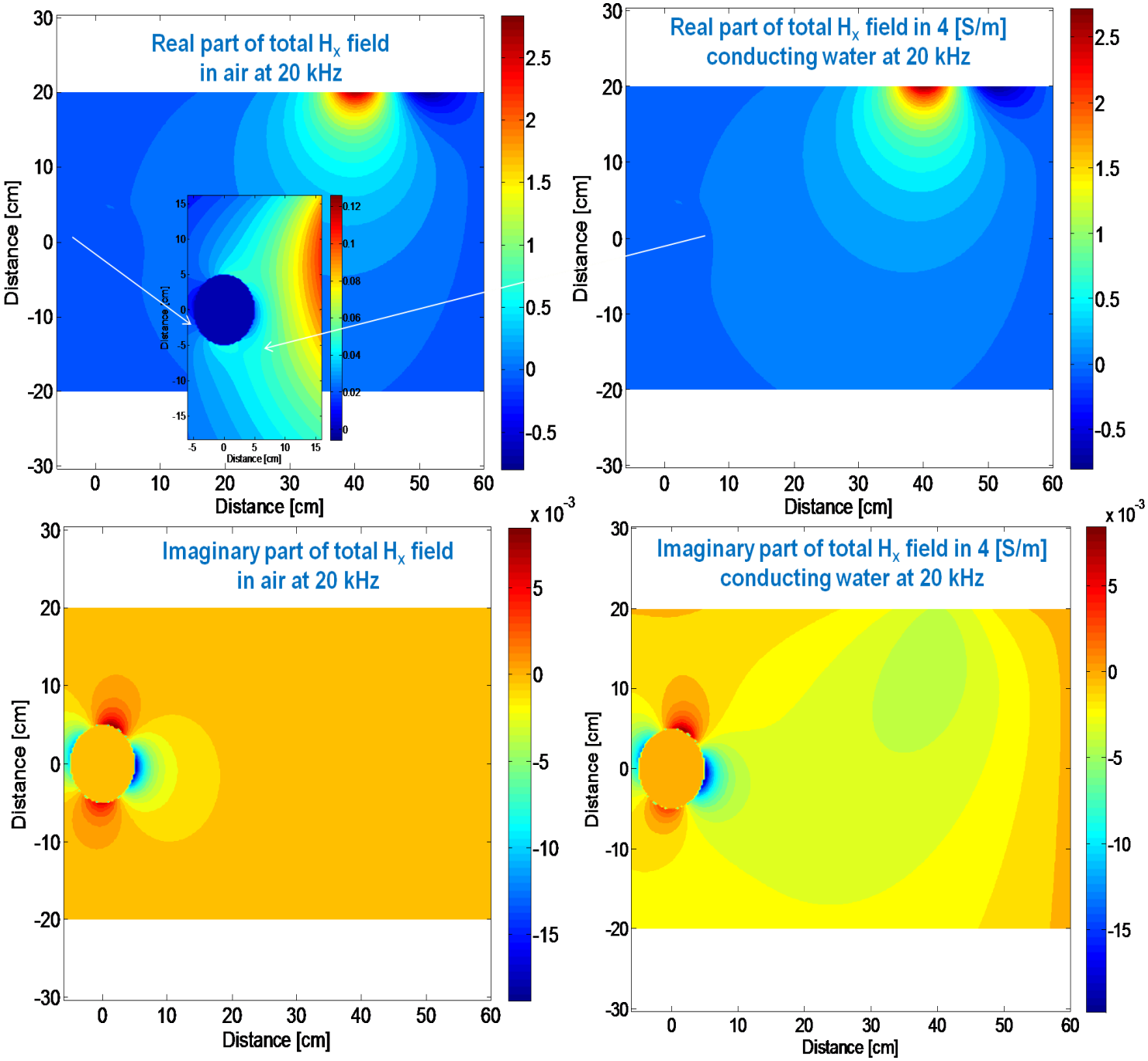

Figure 3-18: Total H_x magnetic field distributions inside and outside a sphere of radius 5 cm placed in air (left column) and in conducting water (right column).
(Top: inphase part; bottom: quadrature part.) The sphere is illuminated with a GEM-3D sensor placed 25 cm above and 60 cm to the side of the sphere's center.

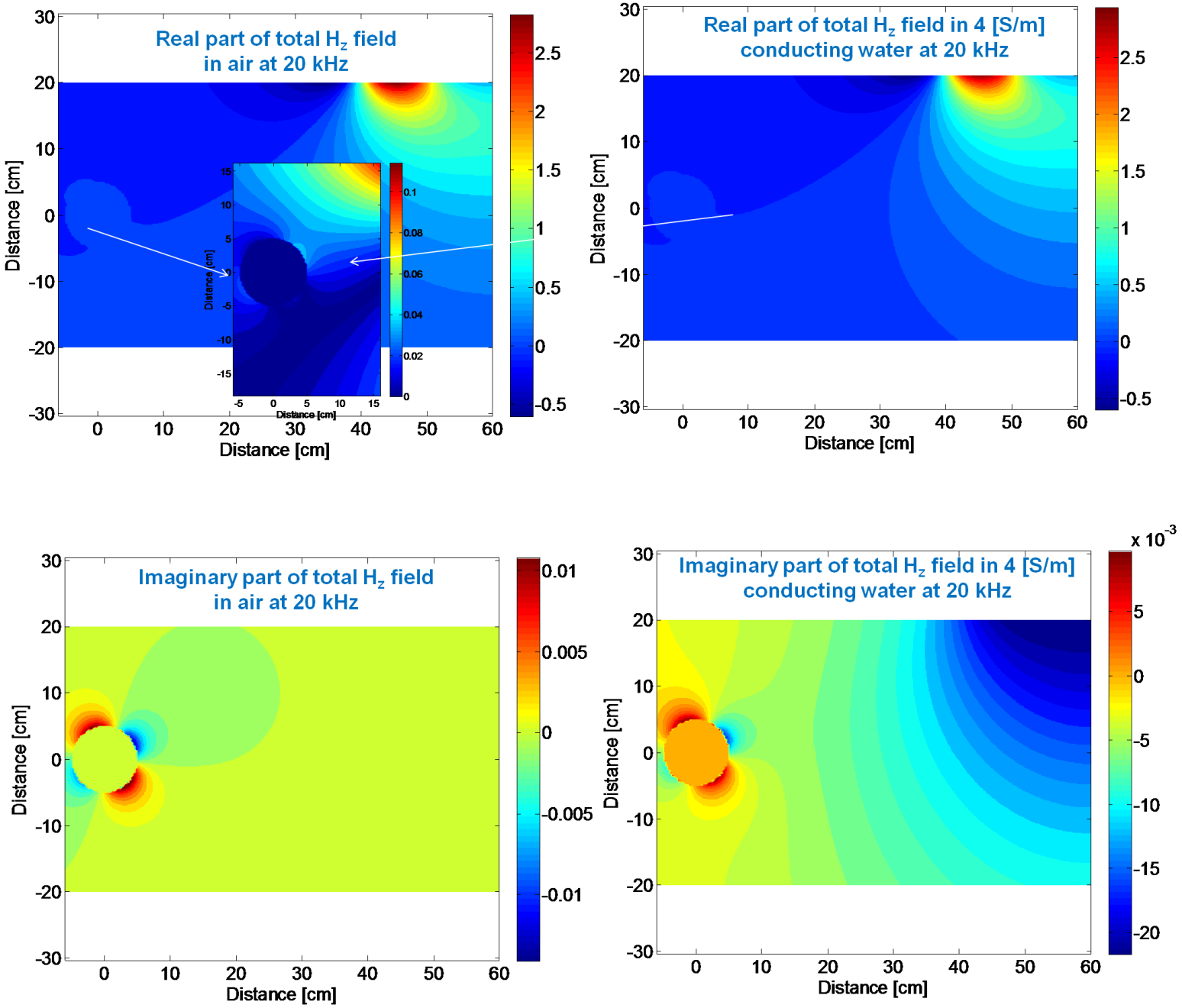

Figure 3-19: Total H_z magnetic field distributions inside and outside a sphere of radius 5 cm placed in air (left column) and in conducting water (right column).
(Top: inphase part; bottom: quadrature part.) The sphere is illuminated with a GEM-3D sensor placed 25 cm above and 60 cm to the side of the sphere's center.

3.10 Surface roughness effects

3.10.1 Code validation

The accuracy of the MAS simulations can be controlled by observing the mismatch of the tangential components of magnetic fields in the areas between the collocation points on the surface of water (or any other object of interest present in the problem), where the boundary conditions were not enforced. Figure 3-20 at left shows a typical mismatch in our simulations, observed on the sample geometry depicted on the right panel of Figure 3-20. The mismatch is less that 1% of the actual values of tangential magnetic fields on the water surface.

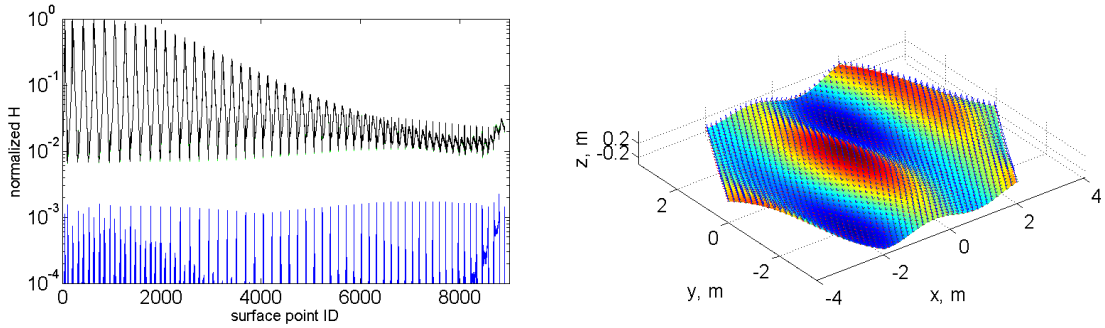

Figure 3-20: MAS boundary conditions and geometry.
(Left) The (obscured) green and black curves show the normalized tangential components of the magnetic fields below and above the water surface respectively, while blue curves show the mismatch. The mismatch is several orders of magnitude lower that the values of the fields. (Right) Water surface geometry with surface normals at collocation points. The mismatch is also tested between the collocation points, where it is highest.

3.10.2 Field distributions

Although the surface waves perturb the magnetic field distributions at low altitudes and depths, the impact of these perturbations is decaying with distance. The left-hand panel (A) of Figure 3-21 shows the total magnetic field distributions in the *xy* plane at depth of 2 m under the unperturbed surface. The source of the magnetic field is a square current loop located 1 m above the water and the frequency $f = 100$ Hz (qualitative results presented below are similar within the entire frequency range of interest from 1 Hz to 1 MHz). The right-hand panel (B) of Figure 3-21 shows the total magnetic field distribution at the same location when the water surface is perturbed by a cosine wave propagating in the *x*-direction. The height of the surface wave is 1 m ($z \in [-0.5, 05.]$) and the wavelength is 5 m. Even though the amplitude of the water surface wave is quite high and comparable to the distances between the field source and sensors, the field distribution does not change significantly. Figure 3-22 shows the difference between magnetic fields across the sensor for flat (unperturbed) and rough (perturbed) water surfaces. The character of this difference depends on the water surface geometry, while the magnitude of the H-field perturbation is small compared to the field value itself. For example, the difference between the magnetic fields for flat and rough surfaces, in a case with multiple waves shaping the water surface, is pictured on Figure 3-24. In this case the distribution is asymmetric, since the source of the perturbations—the water surface—is asymmetric as well. As before, however, the magnitude of the perturbations introduced by the rough water surface is decaying with depth (Figure 3-24). It is also worth noting that the precise character of H-field perturbation decay in the *yz* plane is different for different water surface perturbation realizations. Since the net magnetic field perturbation is small, the actual H-field distributions are similar for both flat and rough water surfaces even in cases of multiple surface waves causing the perturbation (Figure 3-23).

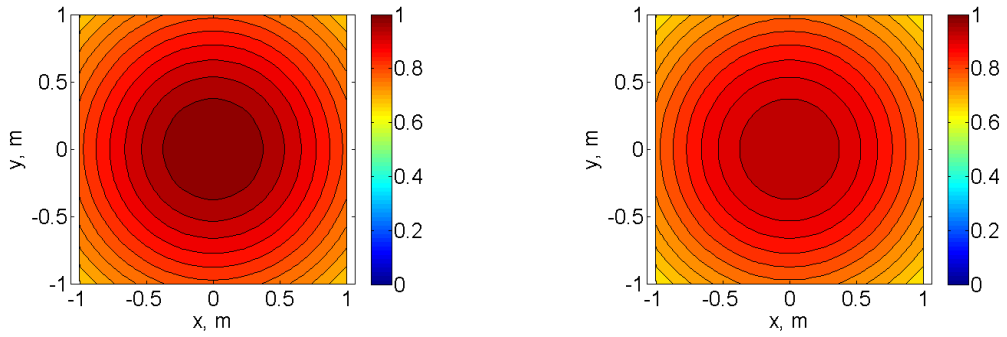

Figure 3-21 H-field distribution at depth 2 m below the (A) unperturbed water surface; (B) surface perturbed by a single cosine wave with wavelength of 5 m and height of 1 m. Fields normalized to their maximal value in the unperturbed case.

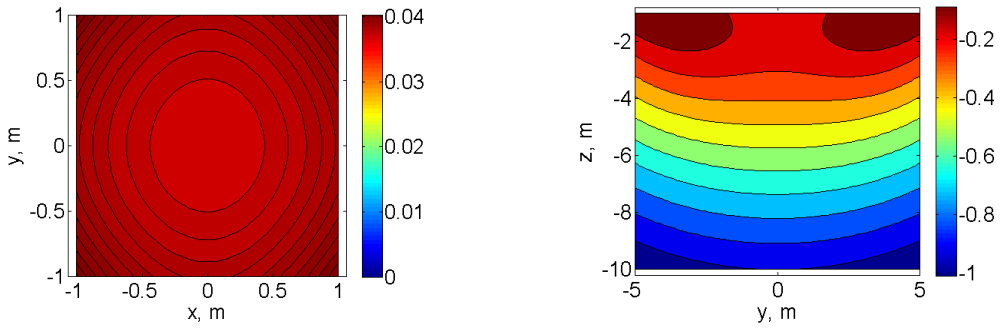

Figure 3-22 (A) Difference between magnetic H field distributions on the *xy*-plane 2 meters below the surface in cases of unperturbed and perturbed water surfaces (normalized to the maximal field value in unperturbed case). (B) Difference between magnetic H field distributions on the *xz*-plane in cases of unperturbed and perturbed water surfaces (normalized by the maximal value of the difference close to the water surface, log10 scale).
The perturbation is a single cosine wave with wavelength 5 m and height 1 m.

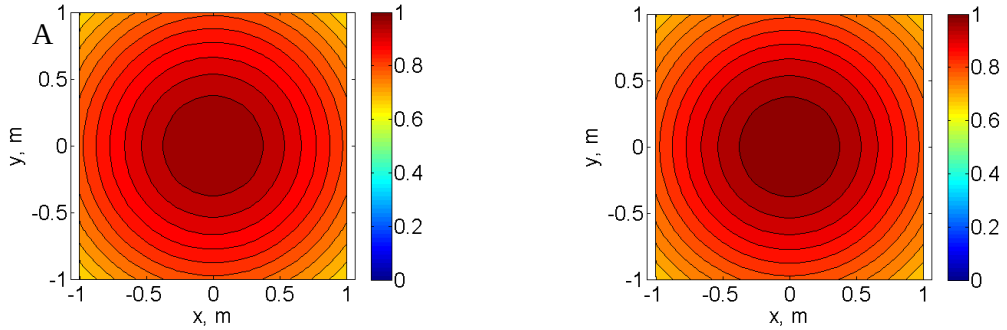

Figure 3-23 H-field distribution at depth 2 m below the (A) unperturbed water surface; (B) surface perturbed by multiple waves (Figure 2-8). Fields normalized to their maximal value in the unperturbed case.

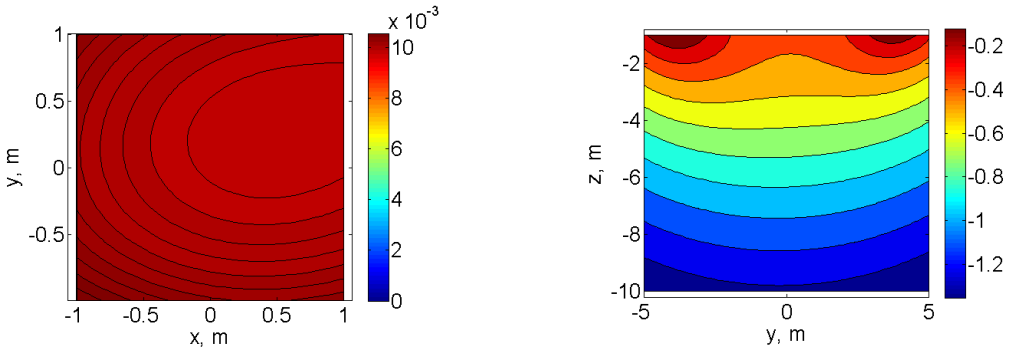

Figure 3-24 (A) Difference between magnetic H field distributions on the *xy*-plane 2 m below the surface in cases of unperturbed and perturbed water surfaces (normalized to the maximal field value in unperturbed case). (B) Difference between magnetic H field distributions on the *xz*-plane in cases of unperturbed and perturbed water surfaces (normalized by the maximal value of the difference close to the water surface, log10 scale).
The perturbation corresponds to multiple propagating surface water waves as in Figure 2-8.

3.11 EMI scattering for multilayer structures

Using the MAS formalism it is also possible to study the interaction between conducting objects (UXO) and the surrounding saline water (conducting environment). Figure 3-25A shows the geometry of the system, with a solid conducting sphere and its surrounding medium. As seen on Figure 3-25 (B) there is quite a significant interaction at high frequencies between the object and surrounding water (both inphase and quadrature components of magnetic fields are different in cases of air and water host media). However, it turns out, that the presence of even a thin layer of insulator can significantly reduce the interaction between the UXO and surrounding saline environment (Figure 3-26 A). If the outer shell is conductive, however, the interaction increases (Figure 3-26 B), which indicates that it is caused by the interaction of electric currents inside the object and the surrounding medium. These results are important because they help shed light on the underlying physics of underwater UXO detection and discrimination processes. With time, the conducting surface of an UXO object may become covered by insulating materials (brought by underwater currents, algae, or appeared as a result of the degradation of the object surface) which will affect the interaction of the sensor and the UXO, affecting the quality of detection.

3.12 Near-field analysis for multilayer structures

In this section we present a near-field analysis to provide an understanding of the interaction phenomena between a multi-layer metallic object and its surrounding conducting host medium. Figure 3-27 and Figure 3-28 show the real and imaginary parts of the total electric field distributions at frequency 100 kHz inside and outside highly conducting and permeable insulated and solid spheres respectively. The sphere is illuminated by the primary magnetic field of the GEM-3D sensor [2]. Similarly, Figure 3-29 and Figure 3-30 show the real and imaginary parts of the total Hz magnetic field distributions. The results show that when the sphere is insulated the total electric and magnetic field distributions are significantly different than when the sphere is solid and has a perfect electrical connection with its surrounding conducting medium. This is because inside the insulated shell the electric and magnetic fields have different phase distributions and behave like irrotational fields.

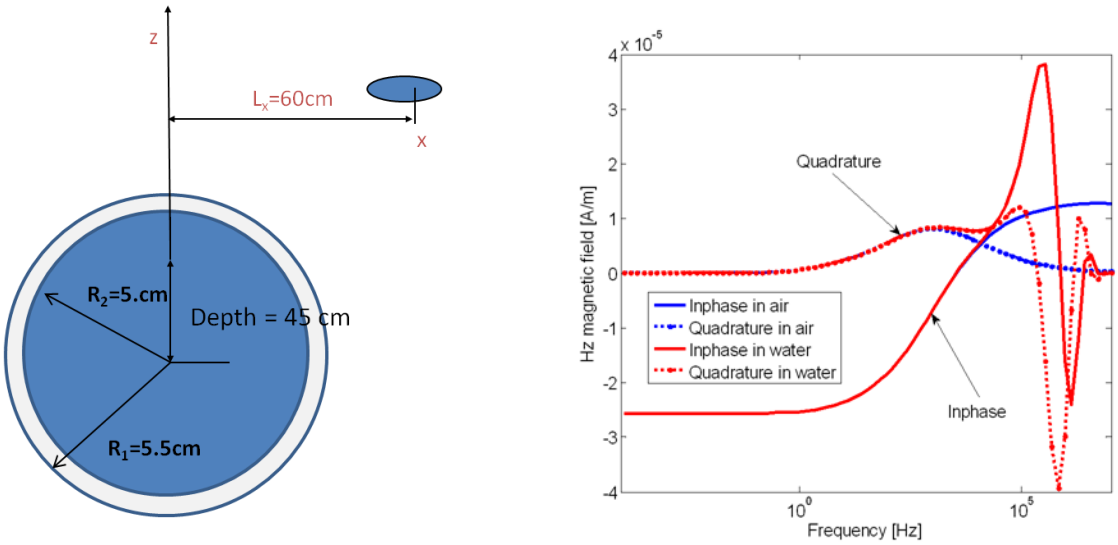

Figure 3-25: Studying the interaction between a conducting object and the surrounding conductive medium. *(A) Geometry of the system; (B) Magnetic field measured by the sensor as a function of source frequency and the surrounding medium, for a solid conducting sphere with the radius R_2 = 5 cm.*

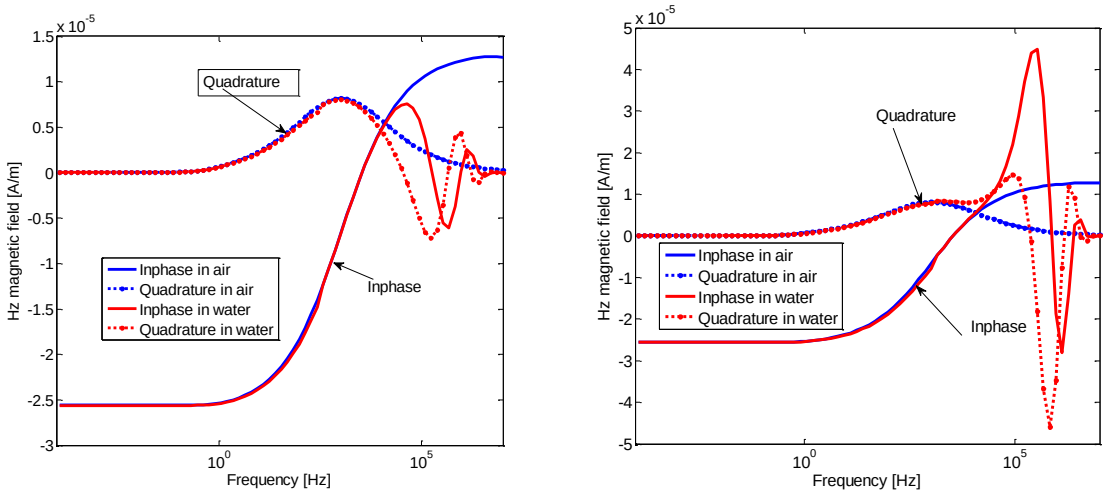

Figure 3-26: (A) Magnetic field in sensor as a function of source frequency and the surrounding medium, for a solid conducting sphere (R_2=5 cm) surrounded by a thin *insulating* shell (total radius R_1=5.5 cm); (B) Magnetic field in sensor as a function of source frequency and the surrounding medium, for a solid conducting sphere (R_2 = 5 cm) surrounded by a thin *conducting* shell (total radius R_1 = 5.5 cm).

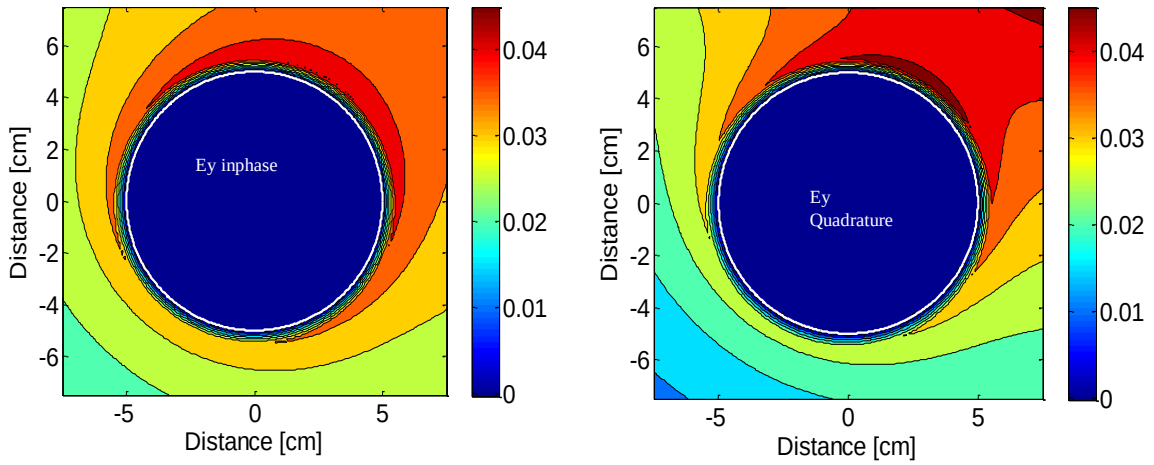

Figure 3-27: Electric field distribution inside and outside of an insulated sphere.

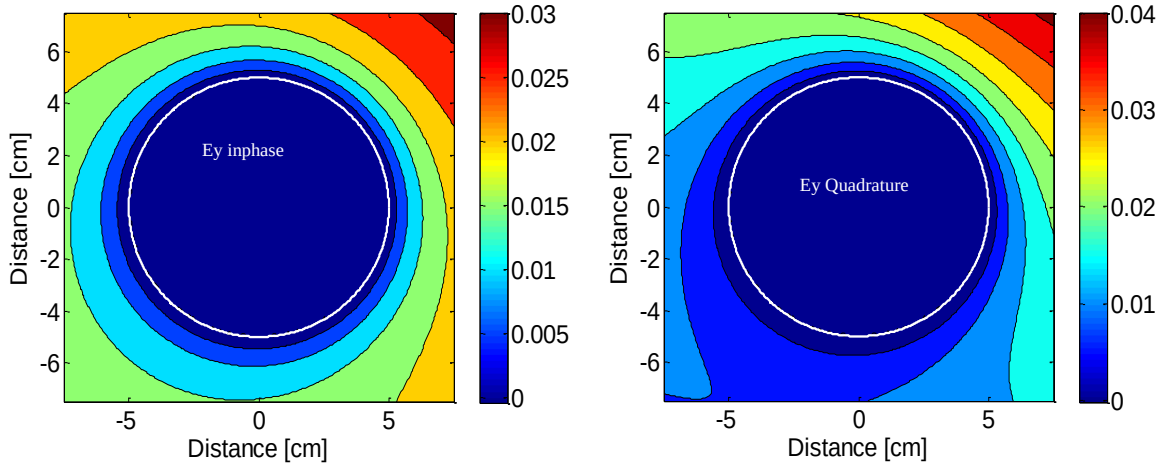

Figure 3-28: Electric field distribution inside and outside of a solid sphere.

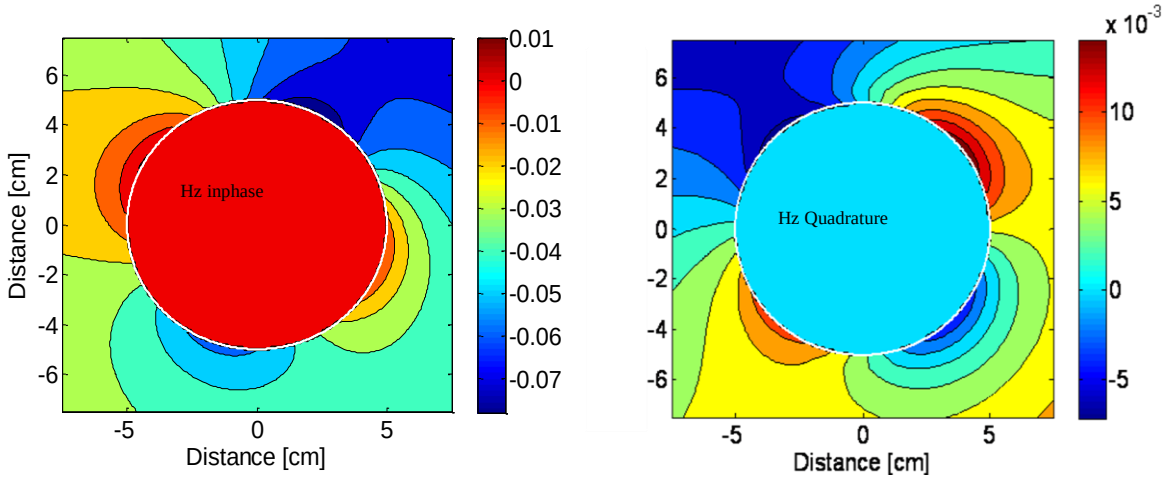

Figure 3-29: Magnetic field distribution inside and outside an insulated sphere (inphase at left, quadrature at right).

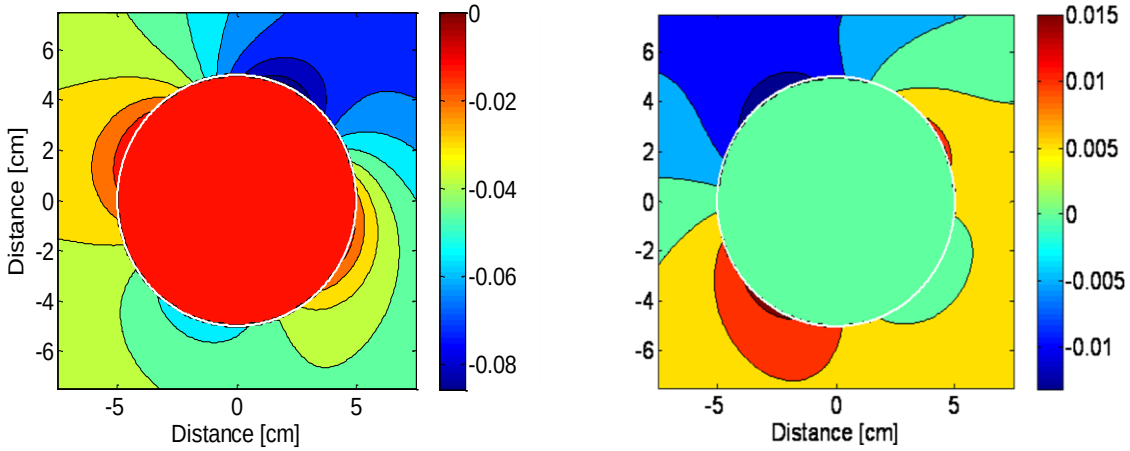

Figure 3-30: Magnetic field distribution inside and outside a solid sphere (inphase at left, quadrature at right).

3.13 The dielectric permittivity and conductivity of seawater

In this part we initially investigated how the dielectric permittivity and conductivity of seawater depend on the temperature and salinity. The results at a frequency of 1 kHz are depicted on Figure 3-31 and Figure 3-32. The results show that as the salinity increases the real part of the dielectric permittivity decreases because ionic currents affect the orientations of the water molecules. On the other hand, the imaginary part of the dielectric permittivity increases with salinity. The temperature is observed to have similar effects. It is also important to notice that the imaginary part of the dielectric permittivity is much higher than the real part, indicating that at this frequency the magnetoquasistatic assumption is valid: i.e., displacement currents are negligible compared to conduction currents. For typical values of salinity (35 g of salt per kilogram of water) and temperature ($T = 15\,^{o}$C) the model predicts a conductivity of approximately 4.2 S/m, which is very close to the actual measured value (4 S/m) for typical seawater. The conductivity as a function of salinity and temperature is depicted on Figure 3-32 and is seen to increase monotonically with both variables.

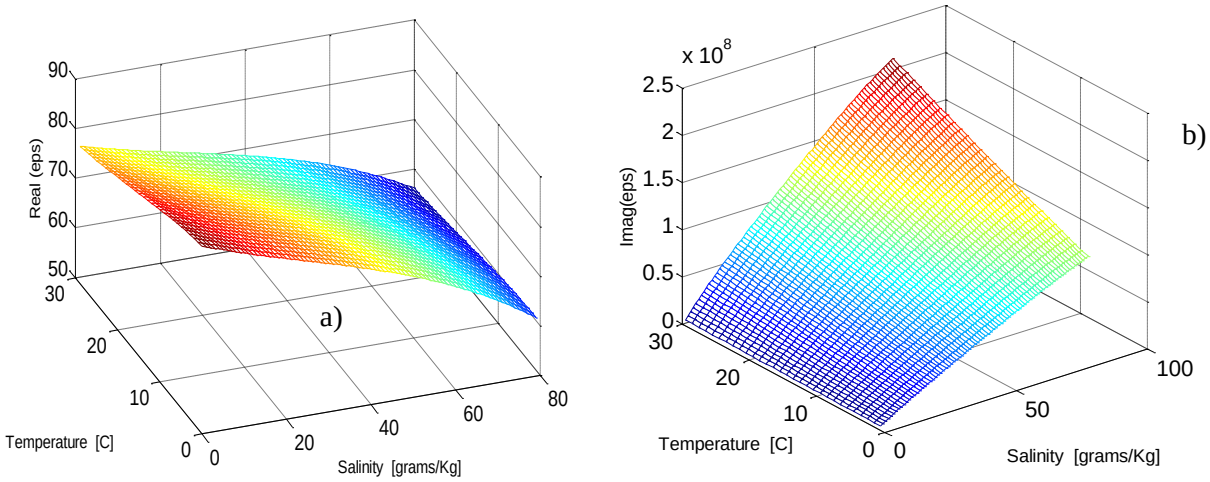

Figure 3-31: Seawater permittivity versus salinity and temperature: (a) Real and (b) Imaginary parts.

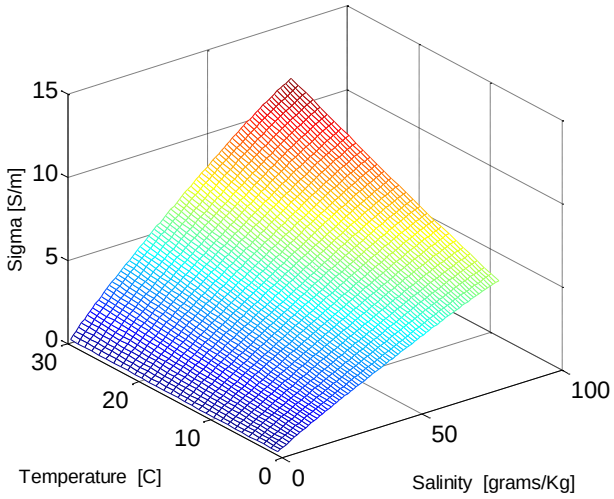

Figure 3-32: Seawater conductivity versus salinity and temperature.

3.14 EMI response for different seawater temperatures

Next we investigate the EMI response of a submerged prolate spheroid for different seawater temperatures. The numerical calculations were done using the combined Method of Auxiliary Sources/Surface Impedance Boundary Condition (MAS/SIBC) method. The spheroid was placed in a conductive medium and illuminated with the GEM-3 sensor. The conductivity of the medium was determined from (73) for S = 35 g/kg and for T_1 = 2 ^{o}C and T_1 = 15 ^{o}C. Figure 3-33 shows the response for a spheroid with major and minor axes b and a, aspect ratio b/a=3, a = 5 cm, conductivity 5×10^6 S/m, and relative permeability 100. The sensor was placed 45 cm above the spheroid and offset L = 75 cm to the side. The figure clearly shows that the EMI response changes, particularly at high frequencies; it is therefore important to take the ambient temperature into account during the discrimination process.

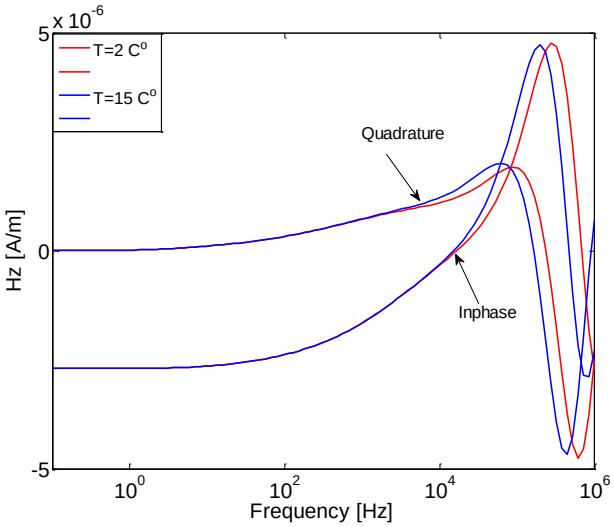

Figure 3-33: EMI response for a spheroid at temperatures T_1 = 2 ^{o}C (red curves) and T_1 = 15 ^{o}C (blue curves) in seawater of salinity S = 35 g/kg. Both inphase and quadrature parts are shown.

3.15 Water-air interface effects

Here we investigate how the multilayer (water/air) interface changes the EMI response for a sphere of radius a = 5 cm, conductivity 5×10^6 S/m, and relative permeability 100. The water and the air are treated as conducting half-spaces. A GEM-3D sensor (whose structure is similar to that of the GEM-3) is placed inside the conducting half-space 75 cm above the interface, as shown in Figure 3-34.

Also, Figure 3-35 shows the resulting electric field distributions. The investigation was done at a frequency of 200 kHz for zero and 30-cm lateral offsets. The field values are in log scale. The results show that the interface has negligible effects. More importantly, there are no surface/evanescent waves at the boundary.

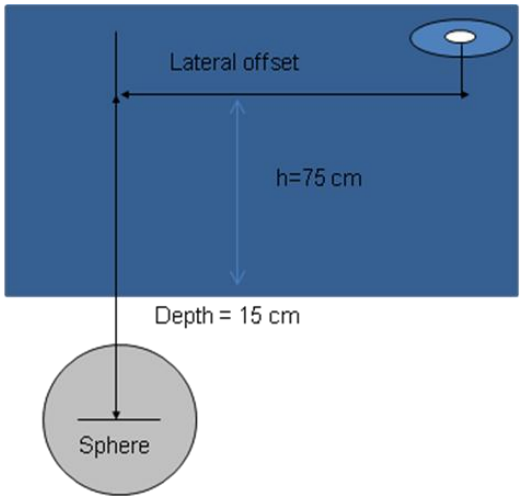

Figure 3-34: A sphere close to a water/air interface.

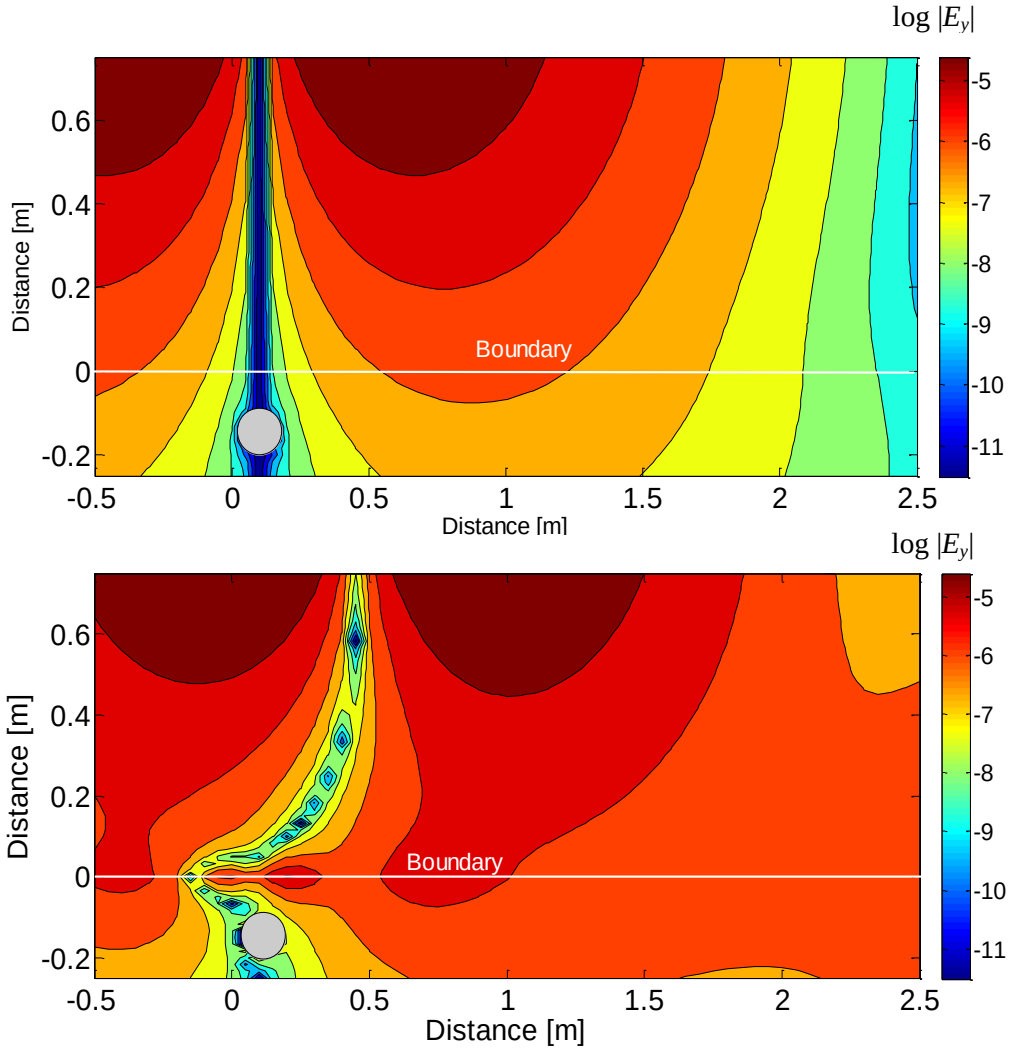

Figure 3-35: Electric field distribution for a sphere placed in a two-layer medium: a) zero lateral offset, b) 30-cm offset.

3.16 Underwater EMI data inversion

3.16.1 The TEMTADS sensor array in underwater environments

Next we assesed the performance of the TEMTADS sensor array in underwater environments. TEMTADS is a new-generation time-domain sensor with mutiple trasmitters and receivers. To investigate the performance of TEMTADS inside salt water the following numerical experiments were performed: a highly conducting and permeable spheroid was placed below center of the TEMTADS. The spheroid was oriented vertically and illuminated with transmitters #12 (center transmitter) and #0 (top left corner). In each case we placed both spheroid and TEMTADS in salt water (with conductivity 4 S/m) and in air (i.e., free space). The distance between the centers of the spheroid and TEMTADS was 45 cm. The results are depicted on Figure 3-36, where the solid lines show the underwater result and the circles show the free-space scenario. These results demonstrate that the conductive environment has negligible effects on the TEMTADS sensor's performances for both Tx #0 and Tx #12. Thus TEMTADS could be deployed for underwater UXO detection and discrimination problems. What is more, the existing discrimination algorithms can also be utilized for UW classification problems without modification.

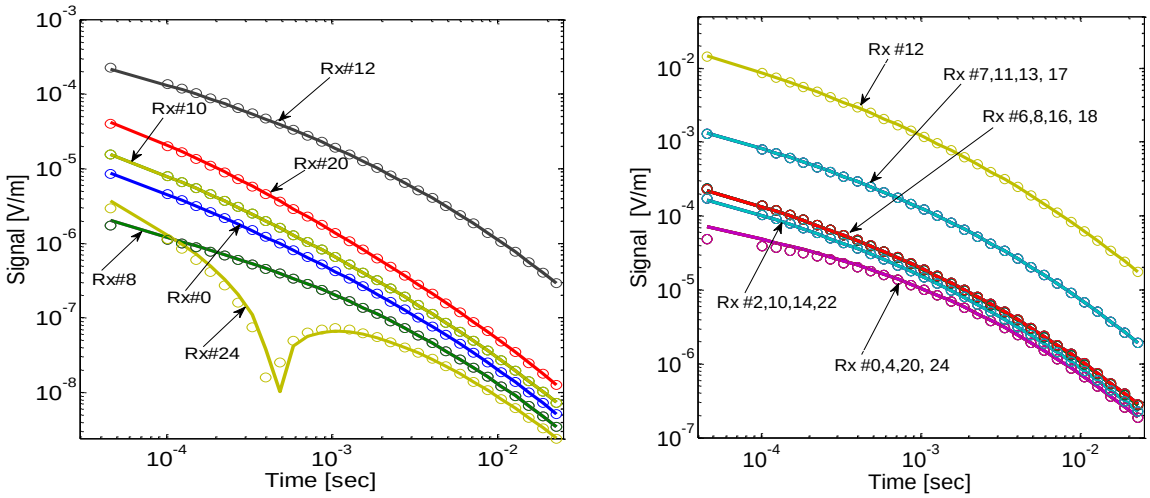

Figure 3-36: Spheroid oriented vertically and placed 45 cm below the center of the TEMTADS system in air (circles) and in conductive water with σ = 4 S/m (solid lines).
The spheroid, with a/b = 3, b = 5cm, $\sigma = 5\times10^6$ S/m, $\mu_r = 100$, is illuminated by transmitters Tx #0 (Left) and Tx #12 (Right).

3.16.2 Determining the location of a submerged object

To demonstrate the applicability of the reduced HAP method for estimating the location of submerged objects we distributed sensors on a planar surface (Figure 3-37). These sensors measure accurately the vector components of the magnetic field simultaneously at several points and allow us to estimate the gradient of the magnetic field along both *x*- and *y*-directions. Using the fact that $\nabla\times\mathbf{H}=0$ and $\nabla\cdot\mathbf{H}=0$ for magnetoquasistatic fields it is straightforward to estimate the other elements of the gradient tensor (namely those along the *z*-axis). Once the gradient of the scattered magnetic field is determined along all directions we can use Eq. (86) to estimate the location of an object without having to solve a traditional ill-posed inverse scattering problem. Knowing a target's location significantly improves the performance of discrimination algorithms and may allow us to conduct real-time discrimination, which is of critical importance for reducing underwater UXO cleanup costs. To illustrate the applicability of the proposed system for location inversion we conducted a numerical experiment. We

placed a spheroid below the center of the TEMTADS sensor array at a depth Z_0 = 50 cm. The vector magnetic field receivers were placed on a planar surface (see Figure 3-37) and separated by either 10 or 20 cm. The spheroid was illuminated by different transmitter coils, and for each primary signal the object's location was estimated using the scattered magnetic field. Figure 3-38 shows the inverted position for the two different spacings of d = 10 cm and d = 20 cm. The figure clearly shows that even with coarse inter-sensor spacing the algorithm is able to estimate the location of the object with acceptable accuracy.

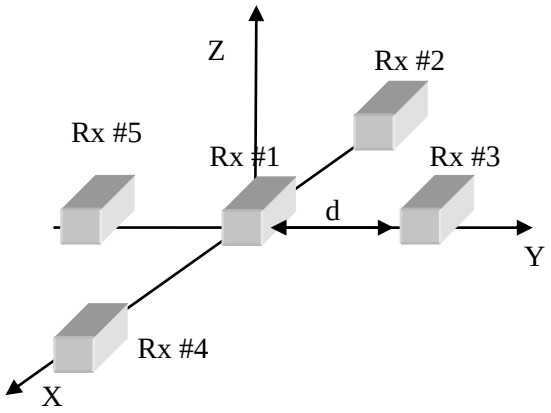

Figure 3-37: Vector magnetic field receivers placed on a planar surface.

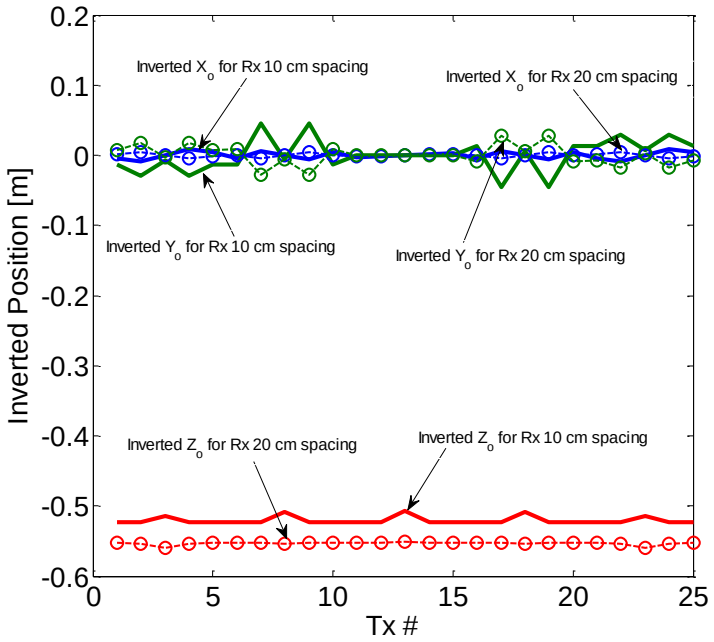

Figure 3-38: Inverted positions for different transmitters.

3.16.3 UW multi-target EMI data pre-processing and inversion

In this section we test the applicability of a data pre-processing scheme based on joint diagonalization (JD) combined with the orthonormalized volume magnetic source (ONVMS) inversion model to perform EMI data analysis and extract classification features in underwater multi-target scenarios. The analysis is performed for synthetic TEMTADS data. JD is a fast and robust technique for quickly estimating the number of potential targets and initially classifying these targets at the data-pre-processing stage *in real time and without invoking a forward model*. JD estimates the eigenvalues and eigenvectors of a square time- or frequency-dependent multistatic response (MSR) matrix; we have found that the number of nonzero eigenvalues (i.e., those above the noise threshold) is related to the number of illuminated targets; moreover, the time-decay patterns of these non-vanishing eigenvalues are intrinsic properties of the targets to which they correspond and can thereby provide robust classification features (see Figure 3-39).

We generated synthetic TEMTADS data sets for a single target (a 60-mm mortar) and for two targets (a 60-mm mortar and a 105-mm HEAT round) using the MAS. In all cases the targets were placed at a depth of 50 cm. For both sets we constructed the 25 × 25 TEMTADS multistatic response data matrix and determined its time-dependent eigenvalues using the Joint Diagonalization algorithm. The eigenvalues, depicted in Figure 3-39, exhibit the targets' specific discrimination features and indicate the number of targets present. In the single-target case, shown at left, there are only three eigenvalues above the noise level; for the two-target case at right there are more than three strong eigenvalues. In addition, we see that the eigenvalues corresponding to the 60-mm mortar have decay characteristics different from those of the 105 mm HEAT, a fact that can be readily exploited when performing target classification. It is worth noticing that JD is a very fast technique that does not involve data inversion and could thus be applied to conduct real-time (or close to real-time) discrimination as the data are being collected.

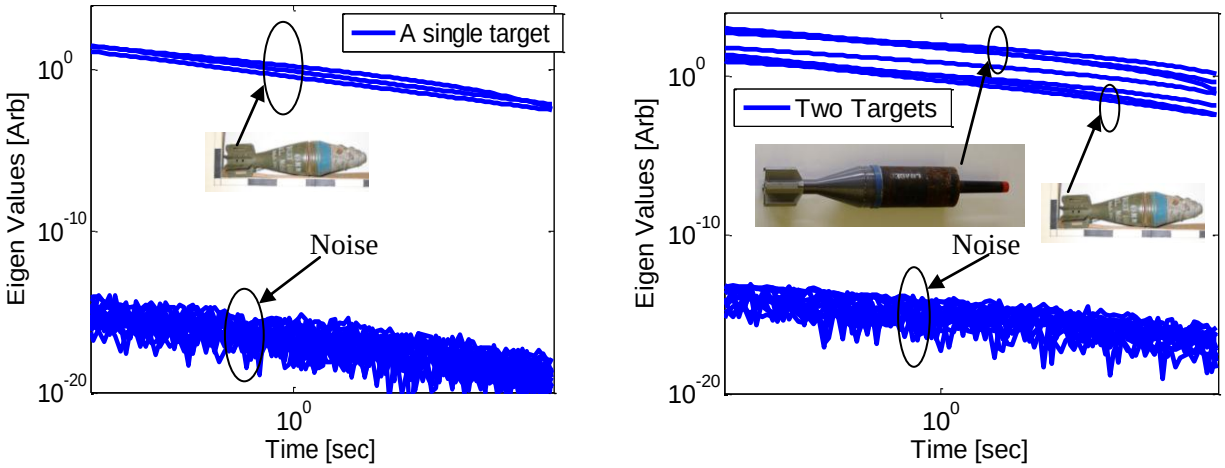

Figure 3-39 Joint-diagonalization eigenvalues vs. time for synthetic TEMTADS data sets with one target (60-mm mortar, left) and two (105-mm HEAT round and 60-mm mortar, right).

The data sets were then inverted using an advanced, physically complete, fast, accurate, and clutter-tolerant forward model, the ortho-normalized volume magnetic source (ONVMS) technique. The ONVMS model is based on the assumption that a collection of scatterers can be replaced with a set of magnetic dipole sources, distributed over a volume, that mimic the eddy currents and magnetic response that are induced on the targets by the sensor and that in turn establish the secondary field. These induced dipoles and currents are distributed inside the objects in question, and thus the spatial distribution of the

responding dipoles (their amplitudes scaled by the primary field) traces a map of "response activity" with a clustering pattern that reveals the locations and orientations of the targets present within. The ONVMS technique is readily applicable to both single- and multi-object data. Among its great advantages are 1) that it takes into account mutual couplings between different parts of a given target and 2) that it avoids matrix singularity problems in multi-object scenarios. Figure 3-40 shows examples of the total magnitude of these ONVMS parameters for a 60-mm mortar and a 105-mm HEAT round inverted from the multi-object TEMATDS synthetic data set of Figure 3-39.

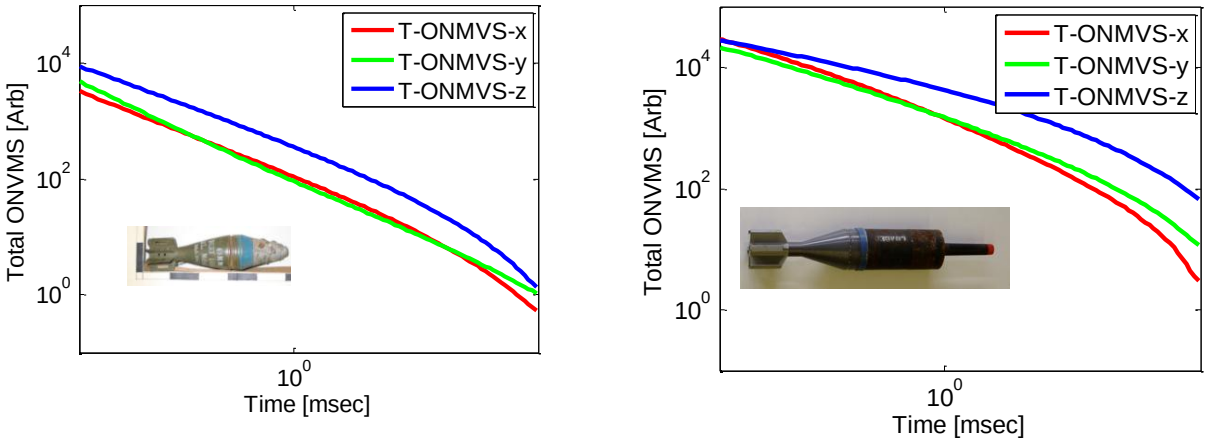

Figure 3-40: Inverted total ONVMS for a multi-target synthetic TEMTADS data set that includes a 60-mm mortar (left) and a 105-mm HEAT round (right).

4 Analytic Studies

4.1 A sphere in a conducting medium

There are approximately one million acres of underwater land at Department of Defense (DoD) and Department of Energy (DOE) sites that are highly contaminated with unexploded ordnance (UXO) and landmines. Detecting and disposing of submerged military munitions is more expensive than excavating the same targets on land, and keeping those enormous costs in check requires the development of innovative detection and discrimination systems that can distinguish quickly between hazardous UXO and innocuous items with false-alarm rates close to nil.

Electromagnetic induction sensing, with working frequencies ranging from tens of Hertz to hundreds of kHz, has been considered as a potential candidate for UXO detection. Several ultrawideband sensors, working in both frequency and time domains, have been developed and proved their worth in the laboratory and in realistic field conditions. They have been accompanied by data processing and analysis algorithms that incorporate the underlying low-frequency electromagnetic physics and have shown reliable and robust performance in a series of blind tests.

The natural next step would be to adapt the apparatus and the modeling to aqueous environments. This task, however, is not trivial. We will not dwell on the hardware aspects of the process, which involve more than merely protecting the coils and electronics from getting wet, but concentrate on the new and difficult physical phenomena that arise when the EMI scattering takes place in a heterogeneous and conducting medium such as water. The finite conductivity and dissipative character of the surrounding medium affect both primary (exciting) and secondary (response) fields; the attenuation depends on distance, so the target sees a primary field with a different spatial structure than it would in vacuum; the detectable secondary field reflects this fact and is itself distorted. These phenomena must be investigated and understood before attempting the design of improved sensors and the implementation of sound discrimination schemes.

Here we look into some of these phenomena by revisiting—and numerically implementing—the analytic solution to the classic problem of a conducting permeable sphere embedded in a conducting permeable medium and responding to a primary (electro)magnetic field established by a sensor [40-44]. The primary field we will take initially to be uniform, and ten that of a point dipole. The problem has a long history. Though preliminary studies had been conducted [40-41], it was Mie [42] and Debye [43] who first solved for the scattering of radiation by a sphere. This was reduced to the EMI regime by Wait [45] and March [46] and further analyzed by Nabighian [47] and Singh [48], who considered the time domain and included the possibility of a conducting exterior medium. We hope that by relaxing simplifying assumptions one by one we can get a grasp of the phenomena and see the different effects that come into play. We also consider the case of a conducting sphere sheathed in a layer of vacuum and then in turn embedded in the conductive medium.

As usual in electromagnetics, the solution of the problem lies in the enforcement of the boundary conditions for the magnetic field and induction at an interface between two media:

$$\begin{aligned} \hat{\mathbf{n}} \cdot (\mathbf{B}_2 - \mathbf{B}_1) &= 0 \\ \hat{\mathbf{n}} \times (\mathbf{H}_2 - \mathbf{H}_1) &= \mathbf{K} \end{aligned} \tag{99}$$

where $\hat{\mathbf{n}}$ is perpendicular to the boundary and points into medium 2. To make the equations more tractable, we concentrate in every case on the EMI regime; in other words, *we always neglect displacement currents.* Thus the results at the high end of the frequency range are to be taken with some skepticism.

4.1.1 Uniform excitation

The classic analysis [45, 49] of the EMI response of a sphere under uniform excitation can be generalized to incorporate the possibility of the surrounding medium being conductive. For this problem we cannot make the usual EMI assumption that the primary and scattered magnetic fields (*i.e.*, the fields outside the target) are irrotational and obey the Laplace equation. On the other hand, the magnetic induction **B** always obeys $\nabla \cdot \mathbf{B} = 0$ and thus $\mathbf{B} = \nabla \times \mathbf{A}$ everywhere, so we can solve the problem by computing the vector potential. We consider a sphere of radius a, conductivity σ_1, and permeability μ_1 embedded in a medium of electromagnetic parameters σ_2 and μ_2 and excited by a uniform field

$$\mathbf{H}^{\text{pr}} = H_0 \hat{\mathbf{z}}$$ (see

Figure 4-1; note that some of the figures use primes for medium 1 and non-primed variables for medium 2). The Helmholtz equation reads

$$\nabla^2 \mathbf{A} - \sigma\mu \frac{\partial \mathbf{A}}{\partial t} = 0, \tag{100}$$

and in the frequency domain adopts the form

$$\nabla^2 \mathbf{A} - j\sigma\omega\mu\mathbf{A} = \nabla^2 \mathbf{A} + k^2 \mathbf{A} = 0, \tag{101}$$

where we have introduced the induction number k and assumed a time dependence $e^{j\omega t}$. In situations with spherical symmetry the solution to the Helmholtz equation can be expressed in terms of spherical Bessel functions; we choose their modified (or hyperbolic) versions. The vector potential within the sphere must be regular at the origin, while the secondary potential must be regular at infinity; we exploit those facts and match the boundary conditions (99) to obtain

$$\begin{aligned}
\mathbf{A}^{\text{pr}} &= \tfrac{1}{2}\mu_2 \mathbf{H}_0 \times \mathbf{r} = \tfrac{1}{2}\mu_2 H_0 a \frac{k_2 r}{k_2 a} \sin\theta \hat{\boldsymbol{\phi}} \qquad \text{(Primary)} \\
\mathbf{A}^{\text{in}} &= \tfrac{1}{2}\mu_2 H_0 a \left(1 + \frac{\beta}{2\pi a^3}\right) \frac{\iota_1(k_1 r)}{\iota_1(k_1 a)} \sin\theta \hat{\boldsymbol{\phi}} \qquad \text{(Interior)} \\
\mathbf{A}^{\text{sc}} &= \tfrac{1}{2}\mu_2 H_0 a \frac{\beta}{2\pi a^3} \frac{\kappa_1(k_2 r)}{\kappa_1(k_2 a)} \sin\theta \hat{\boldsymbol{\phi}} = \frac{\mu_2}{4\pi r^3} e^{-k_2(r-a)} \frac{1 + k_2 r}{1 + k_2 a} (\beta \mathbf{H}_0 \times \mathbf{r}) \qquad \text{(Secondary).}
\end{aligned} \tag{102}$$

The functions $\iota_\nu(z)$ and $\kappa_\nu(z)$ are modified spherical Bessel functions of the first and second kinds [50]. The polarizability of the sphere is

$$\frac{\beta}{2\pi a^3} = \frac{(2\mu_1 + \mu_2)(k_1 a \coth k_1 a - 1) - \mu_2 (k_1 a)^2}{\left(\mu_1 \left(1 + \dfrac{(k_2 a)^2}{1 + k_2 a}\right) - \mu_2\right)(k_1 a \coth k_1 a - 1) + \mu_2 (k_1 a)^2}, \tag{103}$$

which reduces in a nonconducting environment (and is in fact very similar) to the well-known in-vacuum expression [44-45, 49]

$$\frac{\beta}{2\pi a^3} = \frac{(2\mu_1 + \mu_2)(k_1 a \coth k_1 a - 1) - \mu_2 (k_1 a)^2}{(\mu_1 - \mu_2)(k_1 a \coth k_1 a - 1) + \mu_2 (k_1 a)^2}. \tag{104}$$

Figure 4-2 indicates that the correction to the actual response of the scatterer is quite small. The point, however, is that the crucial differences are not to be found in the polarizability of the target but rather in the behavior of the fields within the conducting medium. It is the exponential decay and the bilinear term in the secondary vector potential in (102) that matter. In other words, the fact that the sphere is embedded in a conducting medium does not change the behavior of the sphere much; it is how the primary field

propagates between its emission and its arrival at the scatterer, and how the secondary field propagates between its emission by the scatterer and its arrival at the receiver, that accounts for the measurable differences in response.

The fields are obviously not as transparent as the vector potentials of (102), but their explicit values help highlight the underlying behavior:

$$\begin{aligned}
\mathbf{B}^{\text{pr}} &= \mu H_0 \hat{\mathbf{z}} = \mu H_0 (\hat{\mathbf{r}} \cos\theta - \hat{\boldsymbol{\theta}} \sin\theta) \\
\mathbf{B}^{\text{in}} &= \frac{1}{2} \mu H_0 \left(1 + \frac{\beta}{2\pi a^3} \right) \frac{k_1 a}{k_1 r} \frac{\imath_1(k_1 r)}{\imath_1(k_1 a)} \left(2\hat{\mathbf{r}} \cos\theta + \hat{\boldsymbol{\theta}} \sin\theta \left(1 - k_1 r \frac{i_0(k_1 r)}{i_1(k_1 r)} \right) \right) \\
\mathbf{B}^{\text{sc}} &= \frac{1}{2} \mu H_0 \frac{\beta}{2\pi a^3} \frac{k_2 a}{k_2 r} \frac{\kappa_1(k_2 r)}{\kappa_1(k_2 a)} \left(2\hat{\mathbf{r}} \cos\theta + \hat{\boldsymbol{\theta}} \sin\theta \left(1 + k_2 r \frac{k_0(k_2 r)}{k_1(k_2 r)} \right) \right)
\end{aligned} \tag{105}$$

The electric fields can be found from $\mathbf{E} = -j\omega\mathbf{A}$, and Ohm's law $\mathbf{J} = \sigma\mathbf{E}$ allows us to compute the current densities in the media:

$$\begin{aligned}
\mathbf{J}^{\text{pr}} &= -\frac{1}{2} H_0 k^2 r \sin\theta \hat{\boldsymbol{\phi}} \\
\mathbf{J}^{\text{sc}} &= -\frac{1}{2} H_0 \frac{\beta}{2\pi a^3} k^2 a \frac{\kappa_1(k_2 r)}{\kappa_1(k_2 a)} \sin\theta \hat{\boldsymbol{\phi}} \\
\mathbf{J}^{\text{in}} &= -\frac{1}{2} \frac{\mu_2}{\mu_1} H_0 \left(1 + \frac{\beta}{2\pi a^3} \right) k_1^2 a \frac{\imath_1(k_1 r)}{\imath_1(k_1 a)} \sin\theta \hat{\boldsymbol{\phi}}.
\end{aligned} \tag{106}$$

Figure 8-27 shows that the conductive medium has a non-negligible influence on the measurable secondary fields, mostly at the high end of the frequency range—which, nonetheless, is well within the range of frequencies used by a sensor such as the GEM-3D [2]. In vacuum, the inphase part of the secondary field is seen to grow monotonically and the quadrature part is always positive. In contrast, in a conducting medium both inphase and quadrature parts follow a pattern of damped oscillation. Figure 4-4 and Figure 4-5 show how the effect varies as the sensor-target distance changes, respectively for a nonmagnetic and a ferromagnetic sphere. These effects of the conductive medium are particularly visible in Figure 4-5, in which the fields have been normalized. Again, the conductive embedding medium has a rather modest effect on the response function (103); most of its influence can be traced back to the exponential factor in (102), which prescribes both decay and oscillation and equally affects the inphase and quadrature parts of the secondary field. The factor also depends on the distance from the sphere's center to the sensor, which helps explain why the geometric effects are exacerbated as the sensor recedes from the target.

Finally, in Figure 4-10 we verify that the solution is correct by showing that the boundary conditions (99) are explicitly satisfied. Note that in every case the exterior field is the sum of the primary and secondary fields.

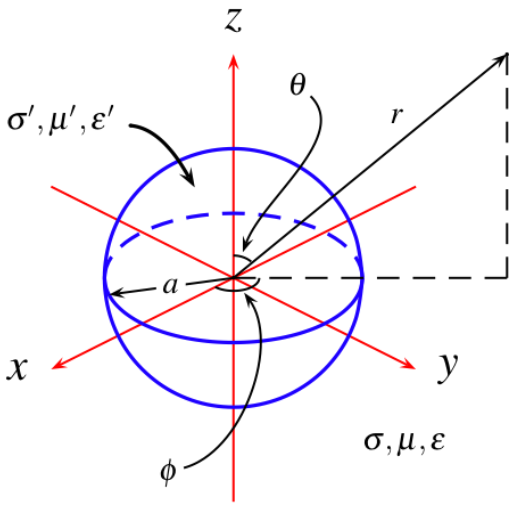

Figure 4-1: Problem geometry for a sphere embedded in a conducting medium.

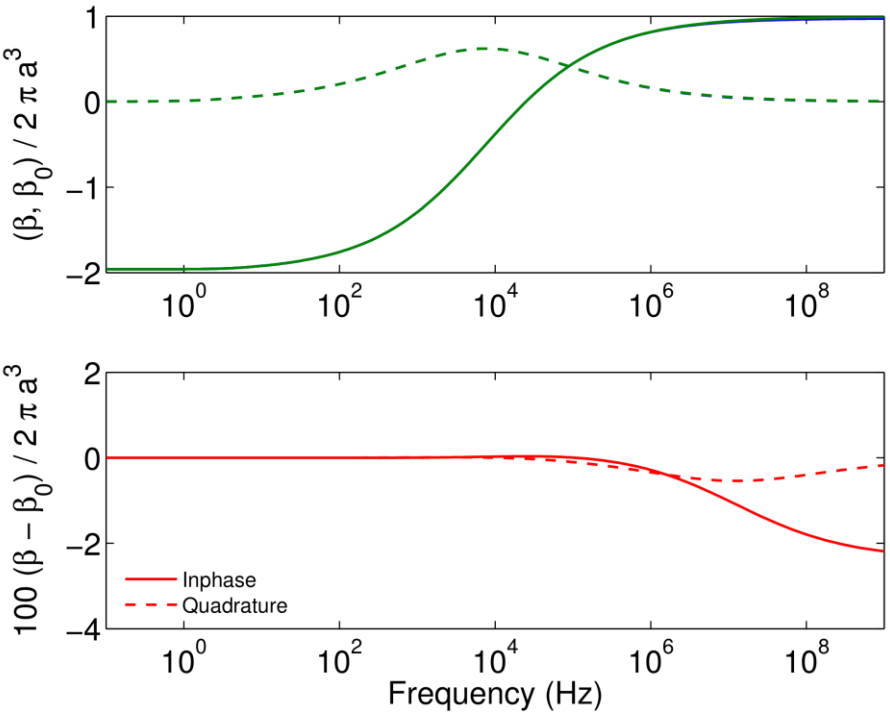

Figure 4-2: The polarizability of the sphere is affected when the surrounding medium has finite conductivity, but not by much.
The top panel shows as a function of frequency the inphase and quadrature parts (solid and dashed lines, respectively) of the polarizability coefficient $\beta / 2\pi a^3$ *of a sphere of radius a = 5 cm,* $\mu_r' = 150$, *and* $\sigma' = 10^6$ *S/m embedded in a medium of conductivity* $\sigma = 4$ *S/m (blue lines) and in vacuum (green lines). The lines coincide except at the very highest frequencies. The bottom panel shows the difference between the two,* multiplied by a factor of one hundred. *The polarizability is seen to decrease with increasing frequency, the effect being noticeable only in the MHz range.*

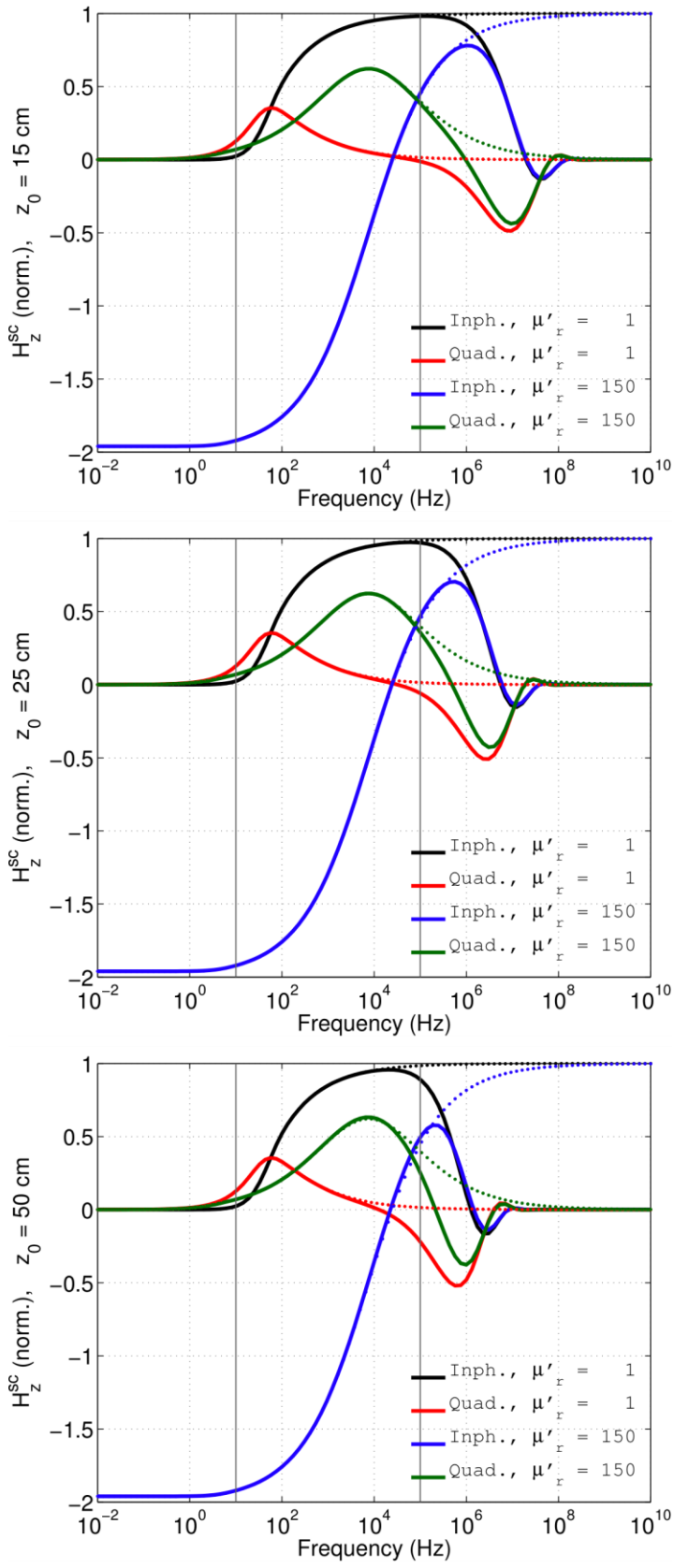

Figure 4-3: Secondary field produced by a sphere subjected to uniform excitation. *The sphere in the figure again has a = 5 cm and is embedded either in vacuum (dots) or in a medium of conductivity $\sigma = 4$ S/m (solid lines). Shown are both a magnetic sphere with $\mu_r' = 150$ and $\sigma' = 10^6$ S/m (inphase: blue; quadrature: green) and a nonpermeable sphere with $\mu_r' = 1$ and $\sigma' = 10^7$ S/m (inphase: black; quadrature: red). The sphere is 15 cm, 25 cm, and 50 cm below the sensor (top to bottom). The solid vertical gray lines give the approximate range of frequencies at which the GEM-3D sensor works. The fields have been normalized so the large-frequency limit of their inphase responses in vacuum is unity. The influence of the medium conductivity is noticeable here and is seen to vary with the target-sensor distance. At large distances the conducting-medium effects are in principle observable by the GEM-3D, even without their additional enhancement due to nonuniform primary fields.*

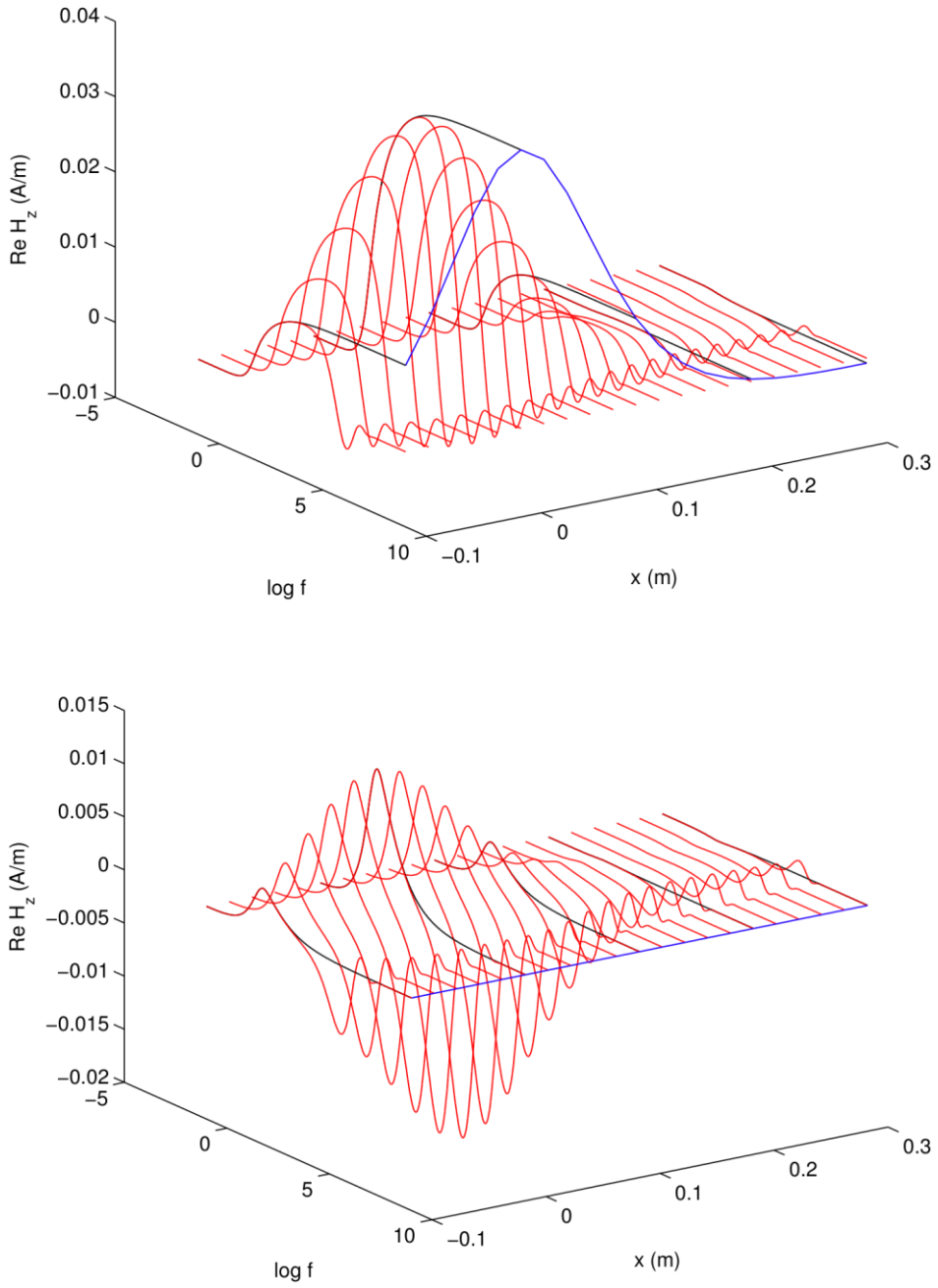

Figure 4-4: Inphase part (top) and quadrature part (bottom) of the secondary field, measured over a transect, of a nonmagnetic sphere under uniform excitation.
The sphere has $\sigma' = 10^7$ S/m, $\mu_r' = 1$ *and* $a = 5$ cm, *and is buried* $z = 15$ cm *below the transect. The black lines show the response in vacuum, which exhibits a* sombrero *profile (blue line) spatially and a monotonically increasing frequency dependence, while the red lines depict the response in a conductive medium with* $\sigma = 40$ S/m. *The frequency profile changes shape at the inflection point where the usual in-vacuum profile becomes negative.*

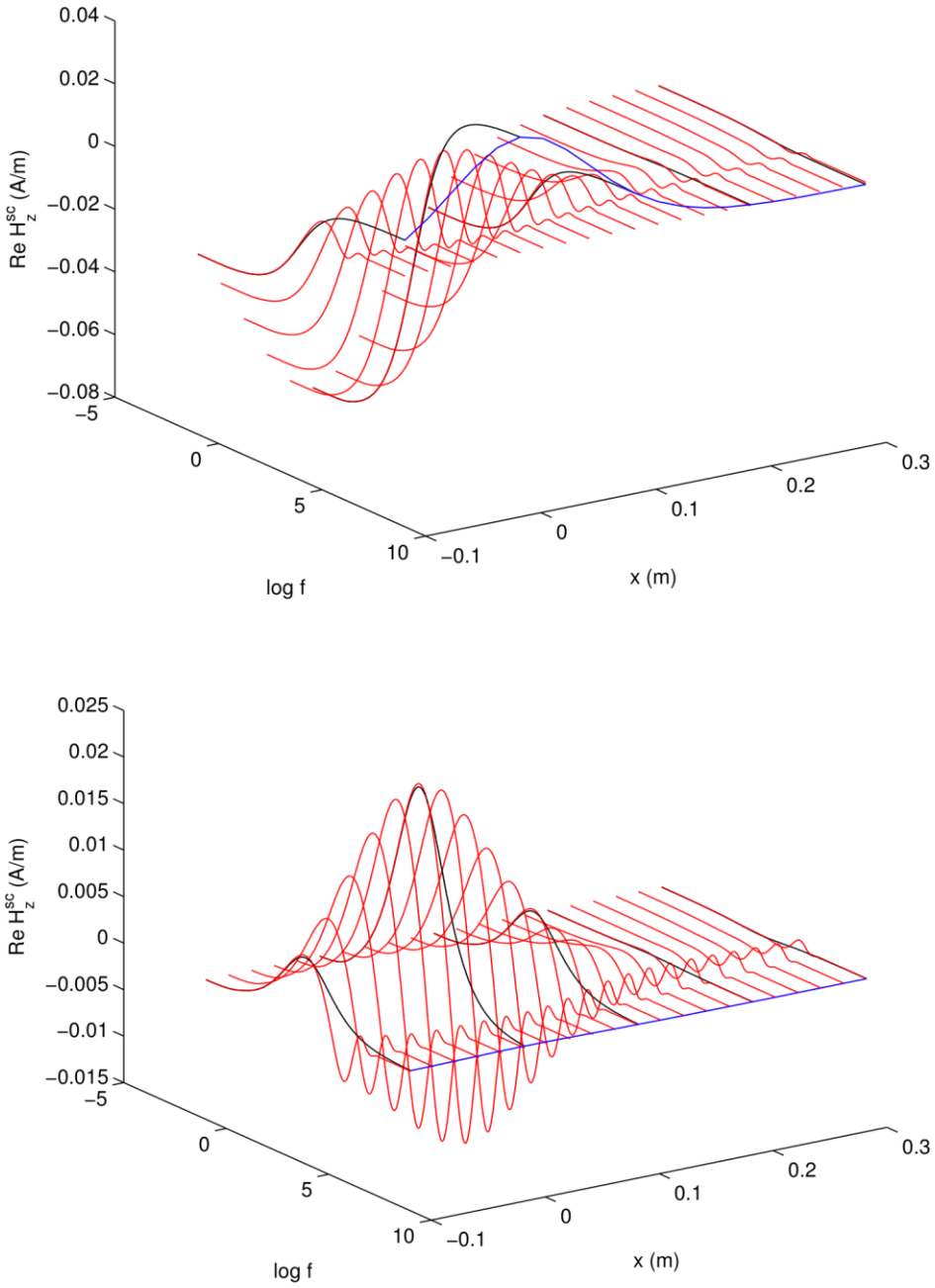

Figure 4-5: Inphase part (top) and quadrature part (bottom) of the secondary field, measured over a transect, of a ferromagnetic sphere under uniform excitation.
The sphere has $\sigma' = 10^6$ S/m, $\mu_r' = 150$, $a = 5$ cm, *and is buried* $z = 15$ cm *below the transect. The black lines show the response in vacuum, which exhibits a sombrero profile (blue line) spatially and a monotonically increasing frequency dependence, while the red lines depict the response in a conductive medium with* $\sigma = 40$ S/m.

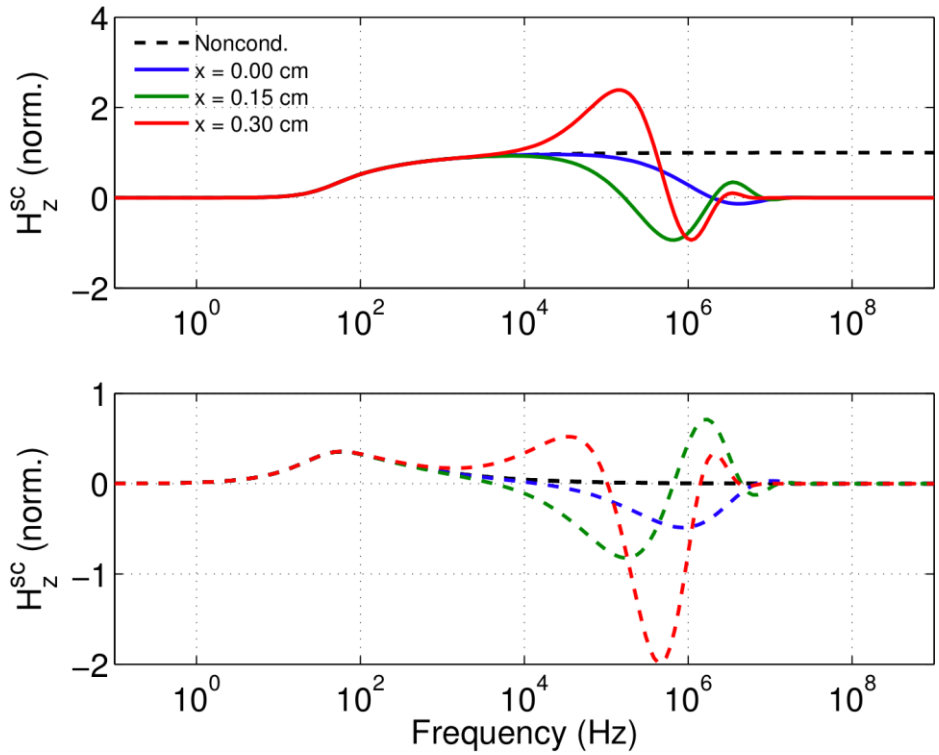

Figure 4-6: Three of the profiles of Figure 8-28 but seen from the side and normalized by the high-frequency limit of the profile in the nonconducting me-dium. *The profile does not just diminish spatially; it also changes with transverse distance in a rather non-intuitive way.*

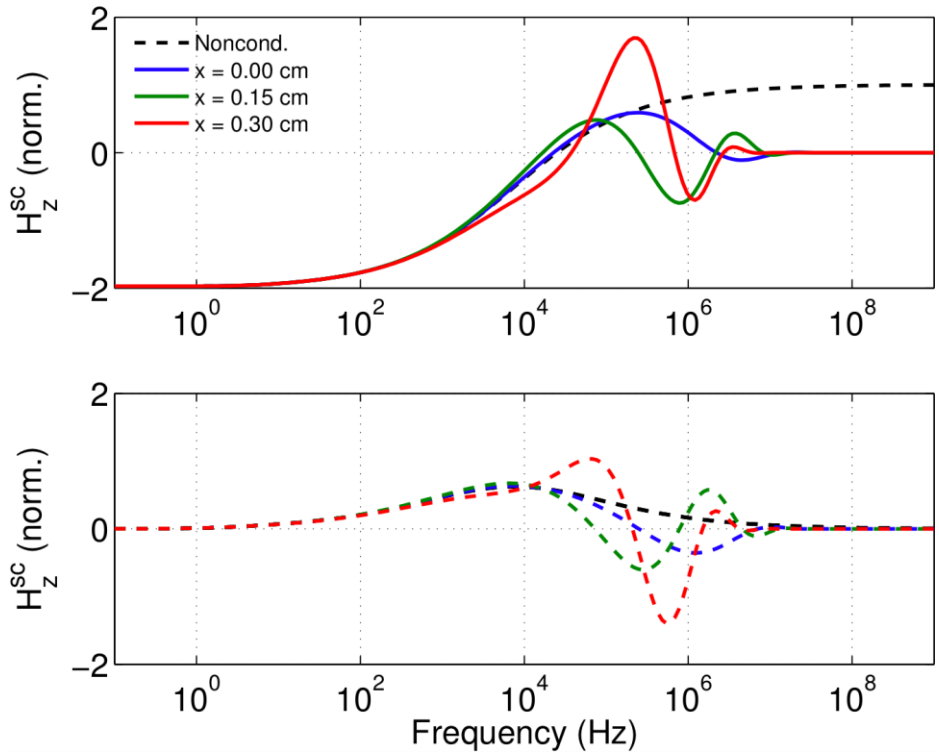

Figure 4-7: Three of the profiles of Figure 8-29; the same as Figure 8-30 but for a ferromagnetic sphere.

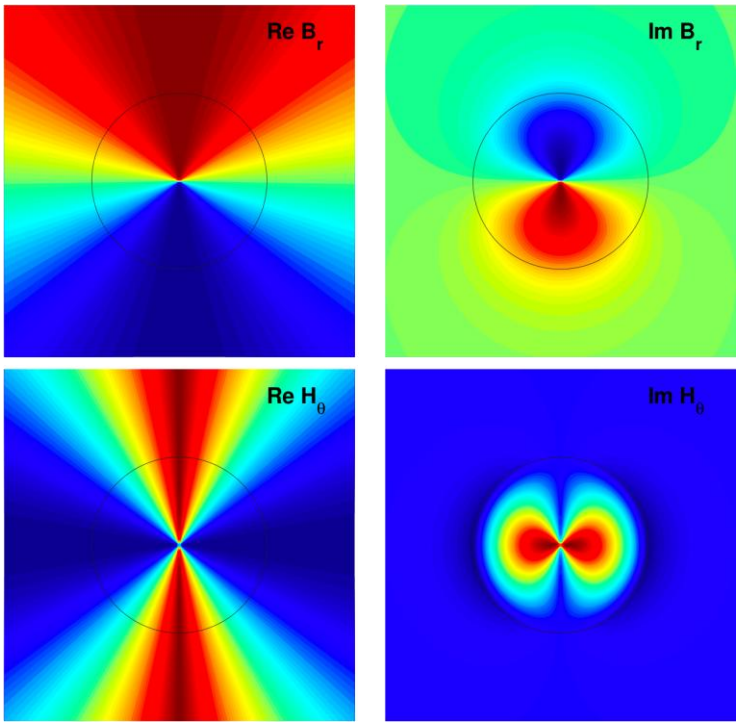

Figure 4-8: That the relevant boundary conditions are obeyed at the sphere surface is not surprising, since they are enforced explicitly in the analytic treatment. *The usual 5-cm sphere with $\mu_r' = 1$ and $\sigma' = 10^7$ S/m embedded in a medium with $\sigma = 4$ S/m is used here as an illustration. To obtain a clearer picture we have used $f = 0.01$ Hz, a very low frequency. Here and in the next plot the fields outside the sphere are not just the secondary fields but include the primary fields.*

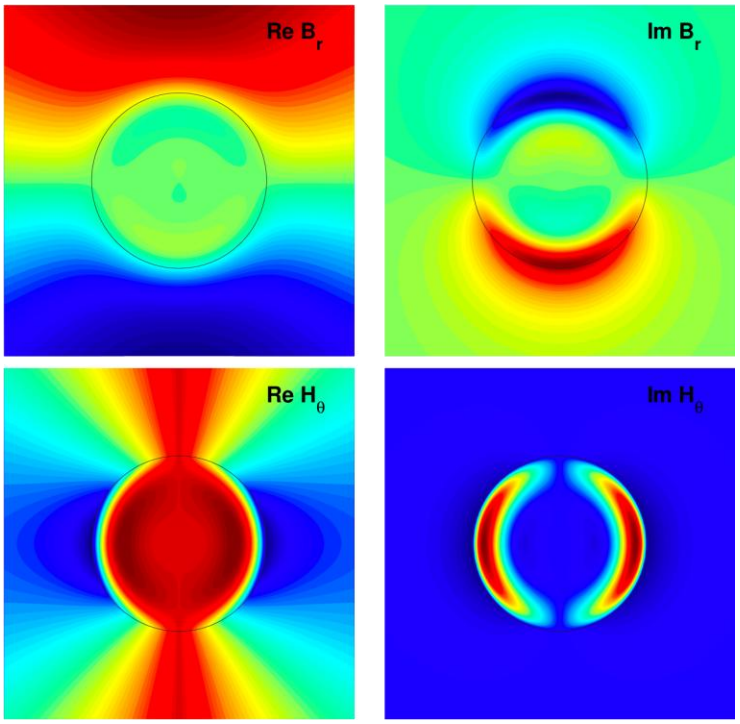

Figure 4-9 Same as Figure 8-32 but at a more realistic frequency, $f = 1000$ Hz.

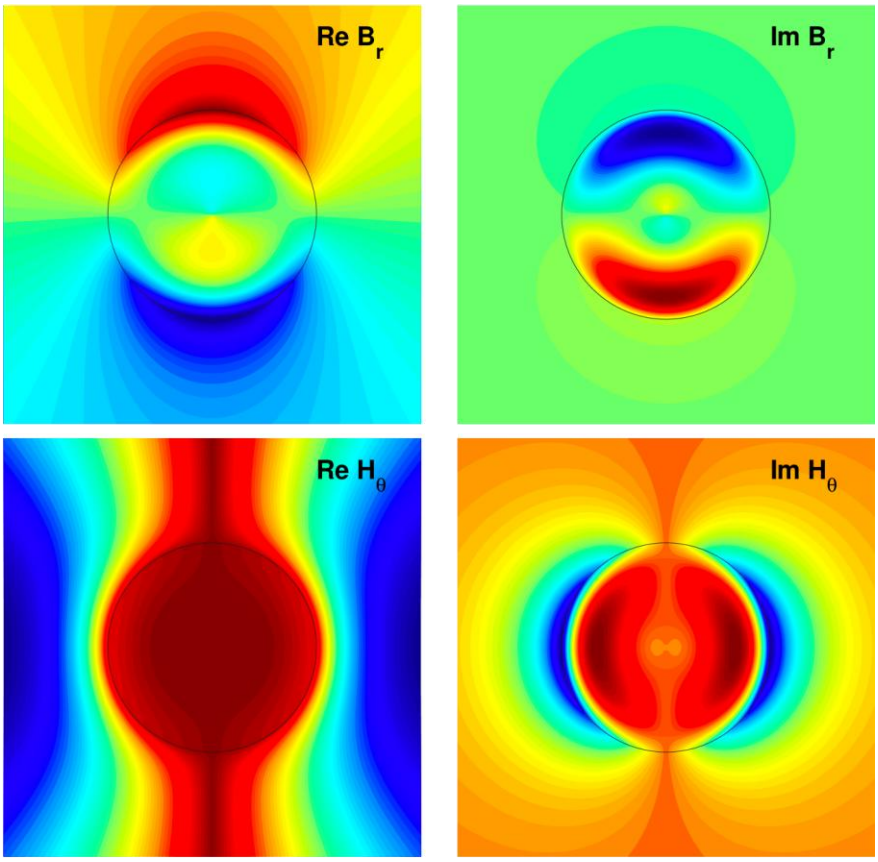

Figure 4-10: Same as the previous figure, but for a permeable sphere with $\mu_r' = 1$ and $\sigma' = 5 \times 10^4$ S/m.
To obtain a clearer figure we have set the conductivity of the sphere to a low value. The medium has $\sigma = 4$ S/m and $f = 500$ Hz.

4.1.2 Dipole excitation

The effects discussed in the previous section become more noticeable when the primary field is not uniform, since both it and the sphere's response are attenuated and distorted. The analysis presented there has been extended by March [46] to a dipolar excitation, with later contributions by Wait [51], Nabighian [47], and Singh [48]. We study it here because it is possible to decompose the primary field of a sensor into a set of transmitting dipoles [52]. The resulting expressions have been called "complex in detail," and they are, both in the mathematical formulation and in the computer implementation [53]. We take the same sphere of

Figure 4-1 but now illuminate it with a point dipole located at $r_0\hat{\mathbf{z}}$ and of moment $\mathbf{m} = m_r\hat{\mathbf{z}} + m_\theta\hat{\mathbf{x}}$, a completely general orientation given the symmetry. We shall display the radial-dipole components (i.e., those proportional to m_r) separately from the transverse ones that involve m_θ. Initially we introduce

$$C = \frac{k_1}{k_2}, \quad K = \frac{\mu_2}{\mu_1}, \quad N = \frac{\sigma_2 + j\varepsilon_2\omega}{\sigma_1 + j\varepsilon_1\omega}, \quad b = \frac{r}{a}, \quad d = \frac{r_0}{a}, \quad \text{and} \quad z = k_2 a, \tag{107}$$

where once more $k_\alpha = -j\sigma_\alpha\mu_\alpha\omega$. The fields are split into radial, polar, and azimuthally components, and further, following Mie and Debye [42-43], into electric (or transverse-magnetic) and magnetic (or transverse-electric) modes:

$$\mathbf{H}^{sc} = \left(H_r^v(\omega) + H_r^u(\omega)\right)\hat{\mathbf{r}} + \left(H_\theta^v(\omega) + H_\theta^u(\omega)\right)\hat{\boldsymbol{\theta}} + \left(H_\phi^v(\omega) + H_\phi^u(\omega)\right)\hat{\boldsymbol{\phi}} \tag{108}$$

where

Radial dipole	*Transverse dipole*
$H_r^v(\omega) = -\dfrac{m_r}{4\pi a r r_0}\sum_{n=1}^{\infty} n(n+1)\,P_n(\cos\theta)\,h_{nrr}^v$	$H_r^v(\omega) = -\dfrac{m_\theta\cos\phi}{4\pi a r r_0}\sum_{n=1}^{\infty} n\,P_n^1(\cos\theta)\,h_{nr\theta}^v$
$H_\theta^v(\omega) = -\dfrac{m_r}{4\pi a r r_0}\sum_{n=1}^{\infty} n\,P_n^1(\cos\theta)\,h_{n\theta r}^v$	$H_\theta^v(\omega) = -\dfrac{m_\theta\cos\phi}{4\pi a r r_0}\sum_{n=1}^{\infty}\dfrac{n}{n+1}\dfrac{\partial}{\partial\theta}P_n^1(\cos\theta)\,h_{n\theta\theta}^v$
$H_\phi^v(\omega) = 0$	$H_\phi^v(\omega) = -\dfrac{m_\theta\sin\phi}{4\pi a r r_0\sin\theta}\sum_{n=1}^{\infty}\dfrac{n}{n+1}P_n^1(\cos\theta)\,h_{n\phi\theta}^v$
$H_r^u(\omega) = 0$	$H_r^u(\omega) = 0$
$H_\theta^u(\omega) = 0$	$H_\theta^u(\omega) = -\dfrac{m_\theta\cos\phi}{4\pi a^3\sin\theta}\sum_{n=1}^{\infty}\dfrac{1}{n(n+1)}P_n^1(\cos\theta)\,h_{n\theta\theta}^u$
$H_\phi^u(\omega) = 0$	$H_\phi^u(\omega) = -\dfrac{m_\theta\sin\phi}{4\pi a^3}\sum_{n=1}^{\infty}\dfrac{1}{n(n+1)}\dfrac{\partial}{\partial\theta}P_n^1(\cos\theta)\,h_{n\phi\theta}^u,$

(109)

$P_l^m(x)$ denote Legendre functions of the zeroth and first orders, the magnetic and electric coefficients are

$$\begin{aligned}
h_{nrr}^v(\omega) &= -(2n+1)\,jCz\,h_n^{(2)}(Cdz)(N_n^v / D_n^v)\,h_n^{(2)}(Cbz)\\
h_{n\theta r}^v(\omega) &= \frac{2n+1}{n}\,jCz\,h_n^{(2)}(Cdz)(N_n^v / D_n^v)(\zeta_n^{(2)})'(Cbz)\\
h_{nr\theta}^v(\omega) &= \frac{2n+1}{n}\,jCz\,(\zeta_n^{(2)})'(Cdz)(N_n^v / D_n^v)\,h_n^{(2)}(Cbz)\\
h_{n\theta\theta}^v(\omega) &= h_{n\phi\theta}^v(\omega) = -\frac{2n+1}{n^2}\,jCz\,(\zeta_n^{(2)})'(Cdz)(N_n^v / D_n^v)(\zeta_n^{(2)})'(Cbz)\\
h_{n\theta\theta}^u(\omega) &= h_{n\phi\theta}^u(\omega) = (2n+1)\,j(Cz)^3 h_n^{(2)}(Cdz)(N_n^v / D_n^v)\,h_n^{(2)}(Cbz),
\end{aligned} \tag{110}$$

primes stand for differentiation with respect to *z*, and the spherical Bessel and Hankel functions and their Riccati-Bessel counterparts are defined by [50, 54]

$$j_n(z) = \sqrt{\frac{\pi}{2z}}J_{n+1/2}(z),\ \psi_n(z) = z\,j_n(z) \quad \text{and} \quad h_n^{(2)}(z) = \sqrt{\frac{\pi}{2z}}H_{n+1/2}^{(2)}(z),\ \zeta_n^{(2)}(z) = z\,h_n^{(2)}(z). \tag{111}$$

Most of the difficulty in implementing this solution lies in the evaluation of the common factor $N_n^{v,u} / D_n^{v,u}$, where

$$N_n^v = j_n(Cz)\,\psi_n'(z) - K\,\psi_n'(Cz)\,j_n(z) \quad \text{and} \quad D_n^v = h_n^{(2)}(Cz)\,\psi_n'(z) - K(\zeta_n^{(2)})'(Cz)\,j_n(z) \tag{112}$$

and N_n^u and D_n^u have *N* instead of *K*. Careful application of Hankel's Bessel-function asymptotic expansions [50] is needed to prevent overflows in the region of interest. Rearranging (112) as

$$\frac{N_n^v}{D_n^v} = \frac{(K-1)n + z\left[\dfrac{J_{n-1/2}(z)}{J_{n+1/2}(z)} - KC\dfrac{J_{n-1/2}(Cz)}{J_{n+1/2}(Cz)}\right]}{(K-1)n + z\left[\dfrac{J_{n-1/2}(z)}{J_{n+1/2}(z)} - KC\dfrac{H^{(2)}_{n-1/2}(Cz)}{H^{(2)}_{n+1/2}(Cz)}\right]}\frac{J_{n+1/2}(Cz)}{H^{(2)}_{n+1/2}(Cz)} \tag{113}$$

we find that the problematic term is the ratio of functions of *z*, since *C* keeps the arguments of the other functions small and tempers their behavior. That ratio is found asymptotically to approach

$$\frac{J_{n-1/2}(z)}{J_{n+1/2}(z)} : \frac{\sin n\frac{\pi}{2} + \cot z \cos n\frac{\pi}{2}}{\cos n\frac{\pi}{2} - \cot z \sin n\frac{\pi}{2}} \quad \frac{P_- \cot\left(z - n\frac{\pi}{2}\right) - Q_-}{P_+ \cot\left(z - (n+1)\frac{\pi}{2}\right) - Q_+}, \tag{114}$$

where

$$\begin{aligned} P_\pm &\approx 1 - \frac{n(n^2-1)(n\pm 2)}{2!(2z)^2} + \frac{n(n^2-1)(n^2-4)(n^2-9)(n\pm 4)}{4!(2z)^4}, \\ Q_\pm &\approx \frac{n(n\pm 1)}{1!(2z)^1} - \frac{n(n^2-1)(n^2-4)(n\pm 3)}{3!(2z)^3}. \end{aligned} \tag{115}$$

Figure 4-11 and Figure 4-12 show the inphase and quadrature parts of the secondary field in a familiar geophysical situation: a GEM-3-like sensor, modeled with a vertical dipole, is set to measure the *z*-component of the secondary field and swept along a transect that passes above the center of a sphere, either nonmagnetic (Figure 4-11) or ferromagnetic (Figure 4-12). The finite-conductivity effects are enhanced in the vicinity of the target and start to occur at lower frequencies. There is less oscillation in the quadrature part as the frequency increases, and the oscillations are suppressed faster as the sensor recedes.

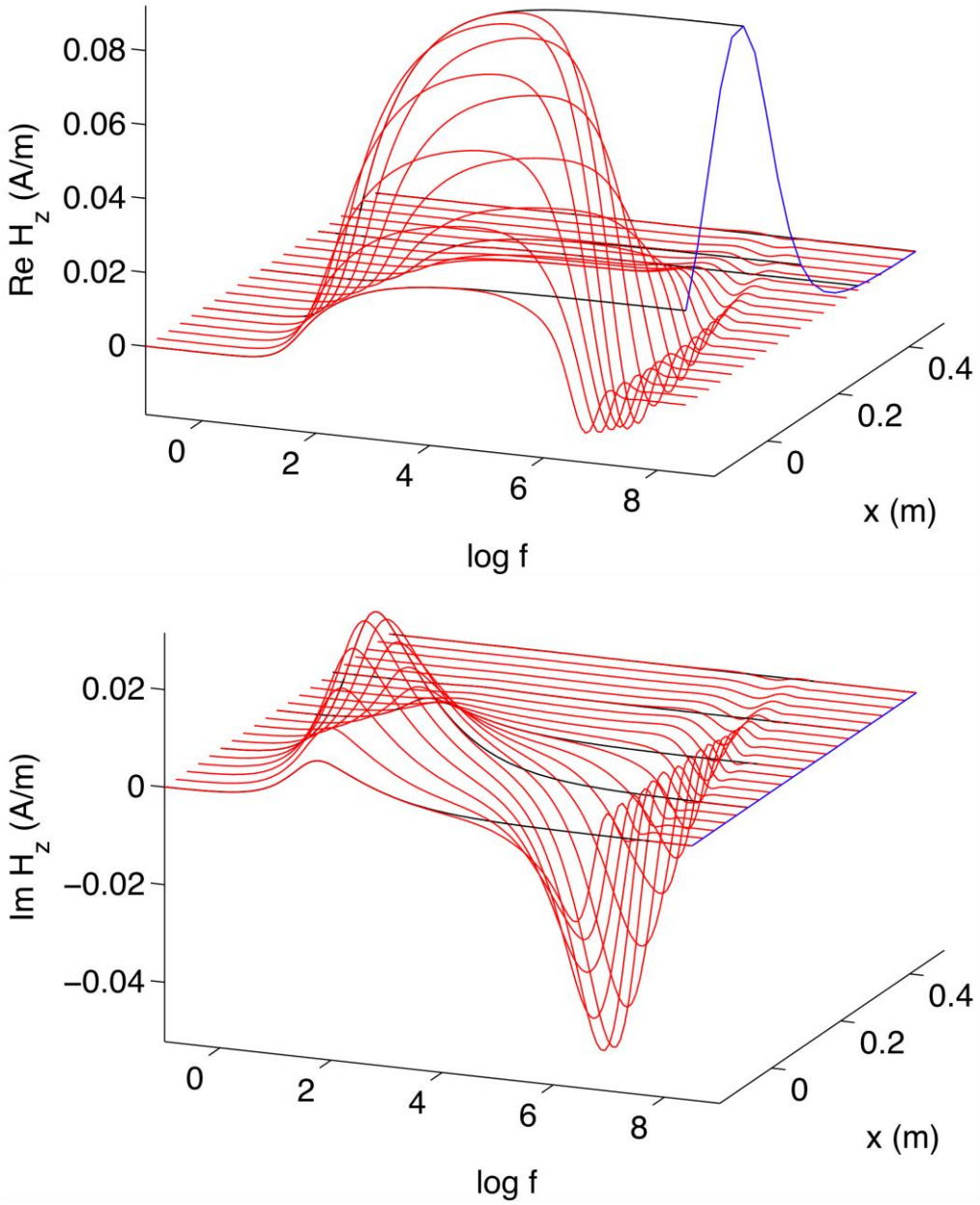

Figure 4-11: Inphase (top) and quadrature (bottom) parts of the secondary field, measured over a transect, of a non-magnetic sphere of radius a = 5 cm under dipolar excitation and embedded in a medium of conductivity σ_2 = 4 S/m, a value typical for seawater.
The sphere has $\sigma_1 = 10^7$ S/m and is buried 25 cm below the transect. Again we show the vacuum response for comparison, along with the high-frequency vacuum spatial profile; the latter in this case is positive over the whole transect, as expected for a monostatic measurement. The finite-conductivity effects are enhanced in the vicinity of the target, and start to occur at lower frequencies, but are more quickly attenuated with distance.

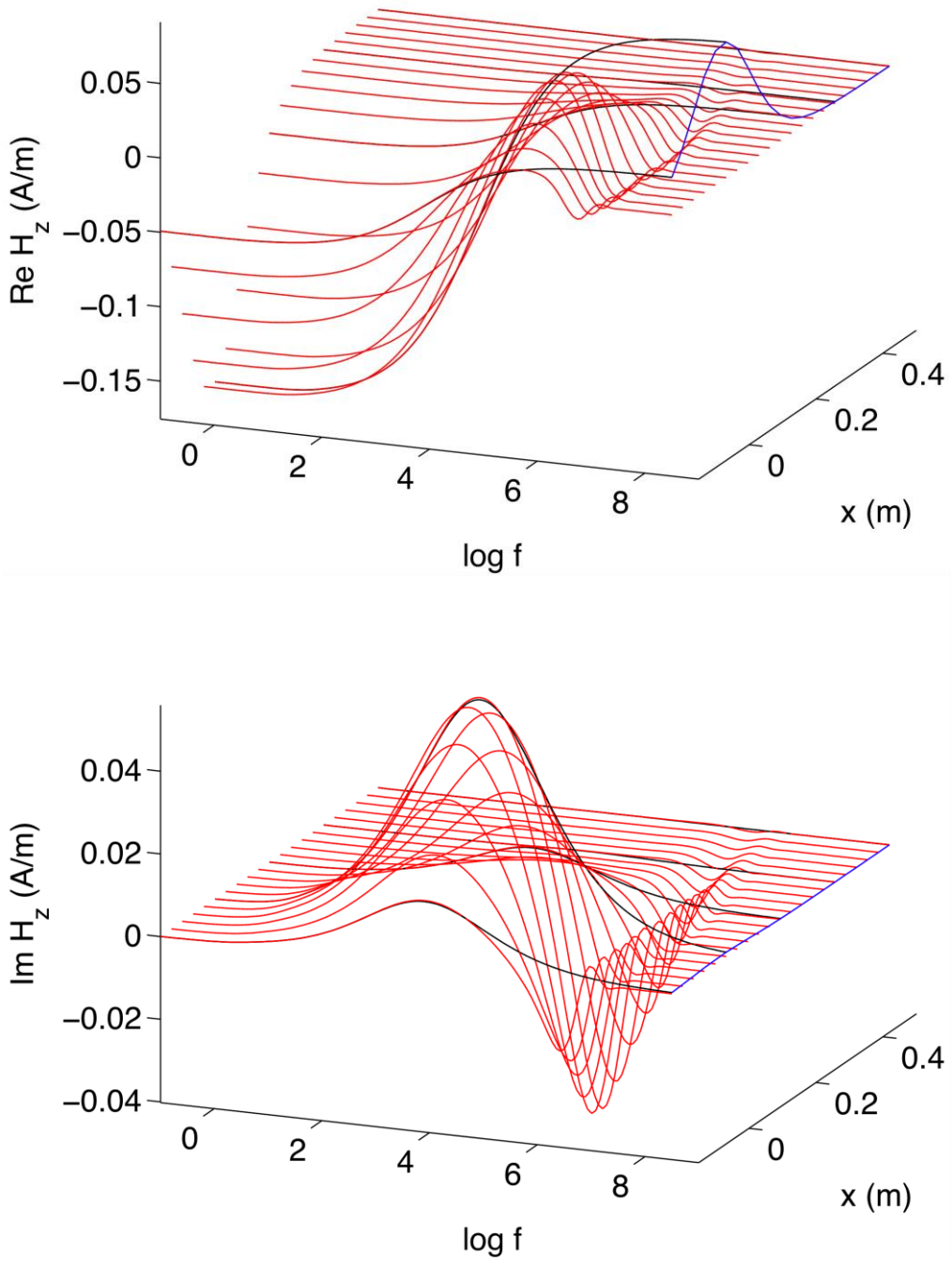

Figure 4-12: Inphase (top) and quadrature (bottom) parts of the secondary field, measured over a transect, of a ferromagnetic sphere of radius a = 5 cm under dipolar excitation and embedded in a medium of conductivity σ_2 = 4 S/m.
The sphere has $\sigma_1 = 10^7$ S/m and is buried 25 cm below the transect. We show the vacuum response for comparison, along with the high-frequency vacuum spatial profile.

4.1.3 A sphere in a vacuum sheath

In some cases of interest (e.g. if the sphere has acquired an insulating "skin" through corrosion [16]) it may be relevant to analyze the response of a sphere surrounded by an empty shell. We take the usual sphere of radius *a* and surround it with an empty shell of thickness $b-a$ (such that the sphere-shell system has radius *b*) and the electromagnetic properties of the vacuum, $\mu=\mu_0$ and $\sigma=0$. The solution of the problem for uniform primary field proceeds as before, except that now we have to match the boundary conditions at $r=a$ and $r=b$, which demands considerably more algebra. For the primary and secondary vector potentials we find

$$\begin{aligned}\mathbf{A}^{\text{pr}} &= \tfrac{1}{2}\mu_2 H_0 b\frac{k_2 r}{k_2 b}\sin\theta\hat{\boldsymbol{\phi}},\\ \mathbf{A}^{\text{sc}} &= \tfrac{1}{2}\mu_2 H_0 b\frac{\tilde{\beta}}{2\pi b^3}\frac{\kappa_1(k_2 r)}{\kappa_1(k_2 b)}\sin\theta\hat{\boldsymbol{\phi}}\\ &= \frac{\mu_2}{4\pi r^3}e^{-k_2(r-b)}\frac{1+k_2 r}{1+k_2 b}(\tilde{\beta}\mathbf{H}_0\times\mathbf{r})\end{aligned} \tag{116}$$

just like in (102), except that the polarizability is more involved:

$$\frac{\tilde{\beta}}{2\pi b^3}\equiv\frac{(\mu_2+2\mu_0)a^3\mathfrak{N}'-2(\mu_2-\mu_0)b^3\mathfrak{D}'}{(2\mu_2+(1+\rho)\mu_0)b^3\mathfrak{D}'-(\mu_2-(1+\rho)\mu_0)a^3\mathfrak{N}'}, \tag{117}$$

where $\mathfrak{N}'$ and $\mathfrak{D}'$ are respectively the numerator and the denominator of(104),

$$\begin{aligned}\mathfrak{N}' &= (2\mu_1+\mu_0)(k_1 a\coth k_1 a-1)-\mu_0(k_1 a)^2,\\ \mathfrak{D}' &= (\mu_1-\mu_0)(k_1 a\coth k_1 a-1)+\mu_0(k_1 a)^2,\end{aligned} \tag{118}$$

with the only difference that in this case the immediate surroundings of the sphere are vacuum, and

$$\rho=\frac{(k_2 b)^2}{k_2 b+1} \tag{119}$$

is the "in a conducting medium" correction factor introduced in (103). For completeness we include the vector potentials within the sphere and in the vacuum layer:

$$\begin{aligned}\mathbf{A}^{\text{in}} &= \frac{1}{2}\mu_2 H_0 a\frac{\mu_0 b^3(3+\rho)(\mathfrak{D}'+\mathfrak{N}')}{(2\mu_2+(1+\rho)\mu_0)b^3\mathfrak{D}'-(\mu_2-(1+\rho)\mu_0)a^3\mathfrak{N}'}\frac{\imath_1(k_1 r)}{\imath_1(k_1 a)}\sin\theta\hat{\boldsymbol{\phi}},\\ \mathbf{A}^{\text{ly}} &= \frac{1}{2}\mu_2 H_0 a\frac{\mu_0 b^3(3+\rho)}{(2\mu_2+(1+\rho)\mu_0)b^3\mathfrak{D}'-(\mu_2-(1+\rho)\mu_0)a^3\mathfrak{N}'}\left(\mathfrak{D}'\frac{r}{a}+\mathfrak{N}'\frac{a^2}{r^2}\right)\sin\theta\hat{\boldsymbol{\phi}}.\end{aligned} \tag{120}$$

We can verify the correctness of expression (117) for the polarizability by considering a few different limiting cases:

1) First, it reduces to (103) when $a\to b$.

2) If we make $k\to 0$, $\mu\to\mu_0$ we get $\tilde{\beta}/2\pi b^3\to a^3\mathfrak{N}'/b^3\mathfrak{D}'$, which recovers the vacuum expression (6) and shows that the sheath explicitly disappears in that limit.

3) In the limit as $a\to 0$ we obtain

$$\frac{\tilde{\beta}}{2\pi b^3}\to\frac{2(\mu_0-\mu_2)}{2\mu_2+(1+\rho)\mu_0} \tag{121}$$

which coincides with the "polarizability" of a spherical vacuum cavity embedded in a conducting medium, as can be verified by solving that problem directly.

4) Most interesting is the limit when $b \to \infty$. The vector potential in the vacuum layer becomes

$$\mathbf{A}^{\text{ly}} = \frac{1}{2}\mu_2 H_0 a\left(\frac{r}{a} + \frac{\mathfrak{N}'}{\mathfrak{D}'}\frac{a^2}{r^2}\right)\sin\theta\hat{\boldsymbol{\phi}}, \tag{122}$$

which includes both a primary component (as in the first line of (116)) and a secondary "sphere in vacuum" term. Note, that at first sight (122) does not appear to be occurring in the vacuum, since it has μ_2 rather than μ_0. The apparent discrepancy is removed once we realize that what excites the target in the original problem (leading to (116)) is a primary *field* of magnitude H_0, to which corresponds a magnetic *induction* $\mu_2 H_0$ and a vector potential proportional to the latter.

There are large differences in β when the shell thickness is comparable to the sphere radius. The changes also tend to take place at the high end of the frequency range. The effects may not be very noticeable for thin shells and at the usual EMI frequencies. Figure 4-13 highlights the effects for underwater-like conditions, and Figure 4-14 exaggerates the properties of sheath and medium (making the former comparable in size to the sphere and the latter one order of magnitude more conductive) so the resulting modifications in β are more easily seen.

4.1.4 Remarks

We have solved analytically for the EMI response by a sphere embedded in a medium of arbitrary finite conductivity, both under uniform and dipolar excitation (with the exciting dipole pointing in any orientation). We wrote code to analyze and display the analytic solutions, concentrating on measurements that mimic the monostatic situations common in UXO sensing; for the first type of primary field we also considered the case in which the sphere is surrounded by a thin nonconducting shell.

In general we find that geometric effects (*i.e.*, the e^{jkR} factor introduced by the conductive medium) dominate over intrinsic ones (those involving the polarizability). The finite conductivity of the medium both distorts and attenuates the measurable secondary field. This is quite noticeable with dipolar excitation, given that the geometric phenomenon occurs both ways: the excitation strength changes with frequency. In the time domain we should expect further changes, since the shape of the excitation is also distorted.

The case of dipolar illumination is particularly relevant because it is possible to decompose the primary field of a sensor into a set of transmitting dipoles [52]. Open problems include the analysis of time-domain instruments and the study of less regular shapes; these have already been studied numerically [55-57], and for perfectly conducting targets [24], but could benefit from a physics-based analysis.

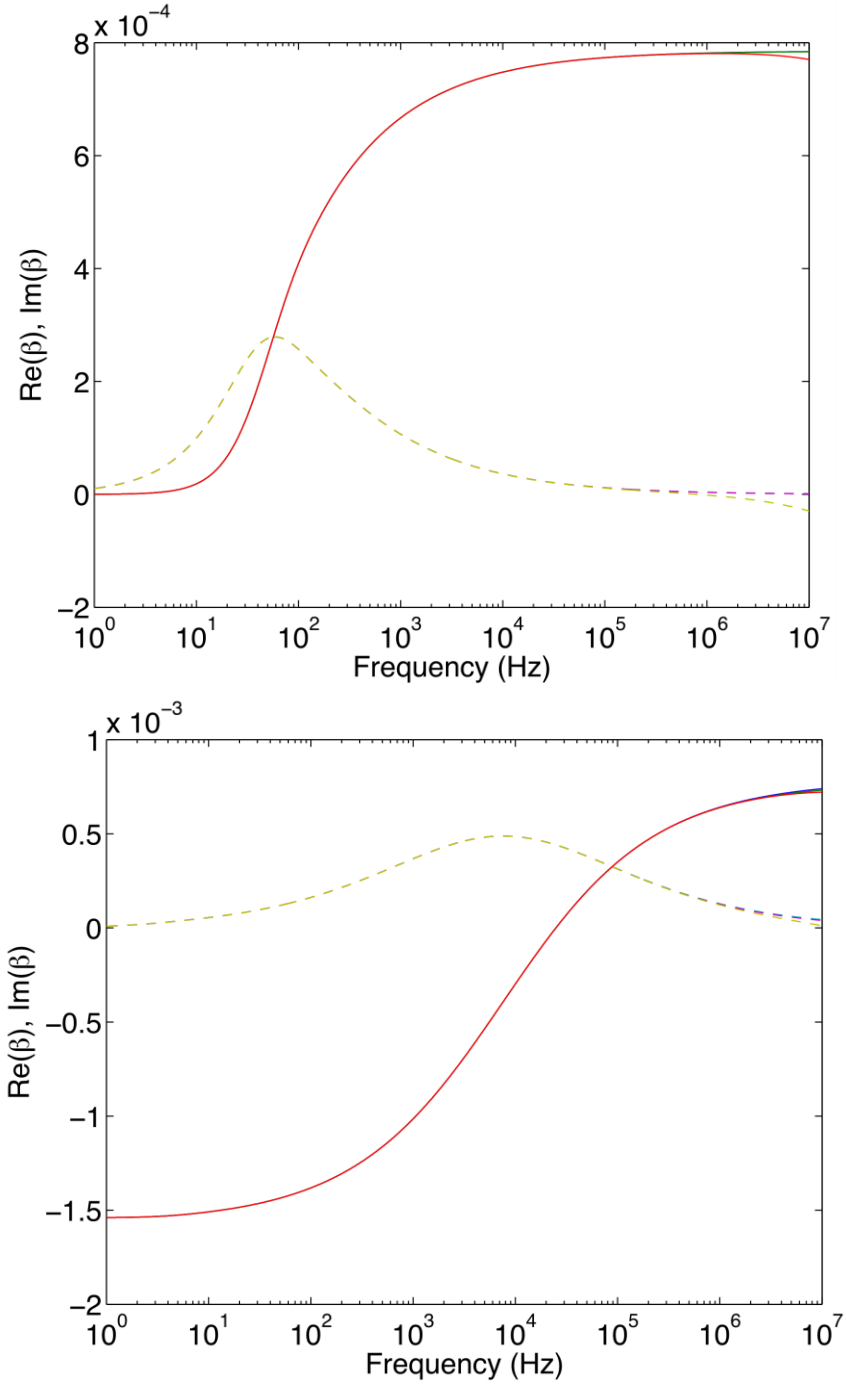

Figure 4-13: Real (solid) and imaginary (dashed) parts of the polarizability element β for a 5-cm-radius sphere in vacuum (blue and cyan), in a conducting medium (green and magenta), and in a conducting medium but surrounded by a relatively thin layer of vacuum (5 mm in this case, shown in red and yellow).
The medium has conductivity $\sigma = 4$ *S/m. The top panel shows a nonmagnetic sphere with* $\sigma = 10^7$ *S/m and* $\mu = 0$ *and the bottom panel shows the response of a ferromagnetic sphere with* $\sigma = 10^6$ *S/m and* $\mu = 150\mu_0$. *The effects are noticeable only at very high frequencies, and are even smaller for thinner shells.*

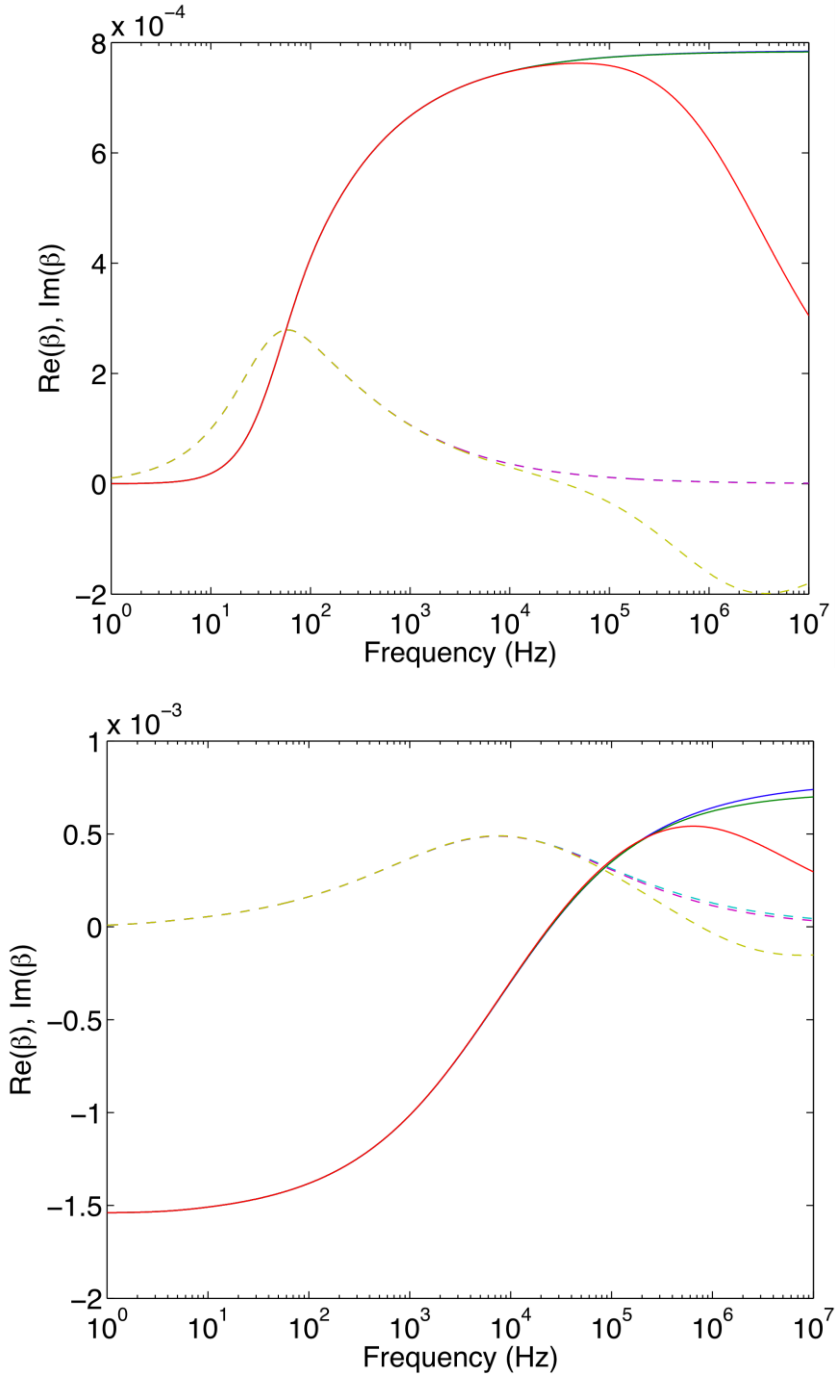

Figure 4-14: Real (solid) and imaginary (dashed) parts of the polarizability element β for a 5-cm-radius sphere in vacuum (blue and cyan), in a conducting medium (green and magenta), and in a conducting medium but surrounded by a thick layer of vacuum (5 cm in this case, shown in red and yellow).
The medium has conductivity $\sigma = 40$ S/m. The top panel shows a nonmagnetic sphere with $\sigma = 10^7$ S/m and $\mu = 0$ and the bottom panel shows the response of a ferromagnetic sphere with $\sigma = 10^6$ S/m and $\mu = 150\mu_0$. With these fairly exaggerated numbers we can see how the polarizability of the sphere-sheath composite deviates from that of the plain sphere (note that this is the polarizability, not the field).

4.2 EMI responses for a spheroid

In this section we use a hybrid model, including asymptotic expressions of the spheroidal wave functions (SWFs), to obtain a reliable, broadband solution for the electromagnetic induction (EMI) response from a conducting and permeable spheroid. We obtain this broadband response, valid in the magnetoquasistatic regime from 0 Hz to 100's of kHz, by combining three different techniques, each applicable over a different frequency range. Validation of this combined technique is accomplished through the comparison of the induced magnetic field predicted by our model to both a finite element/boundary integral (FE-BI) numerical solution and experimental data from various spheroids taken by an ultra-wideband EMI instrument. We also adapt this technique to accommodate conducting host media using two methods. The first involves merely adjusting the primary and secondary potentials in the host medium by an exponential factor using the host medium wavenumber. The second involves reformulating the problem to include the vector wave equation in the surrounding medium. While results for the first simple method break down compared to numerical solutions, the second, complete method has not been rigorously validated.

Electromagnetic induction (EMI) techniques have long been important in geophysical surveying [58-59]. In the past ten years or so, intense interest has focused on small ultra-wideband (UWB) electromagnetic induction (EMI) (10's of Hz up to 100's of kHz) sensors used for shallow surveying to detect and discriminate metallic objects, with one principal application being the detection and discrimination of unexploded ordnance (UXO) [2, 60-61]. UXO contaminate wide regions of the globe and render those regions dangerous at best and uninhabitable at worst. Typical UXO are non-spherical, however, thus complicating the detection and discrimination process.

The solution for the induced magnetic field and potential within and around a conducting and permeable sphere under time harmonic excitation was first proposed by Wait [45, 62] over fifty years ago. Since that time, however, the lack of an analytical magnetoquasistatic solution for nonspherical geometries has hampered development of appropriate signal processing, inversion, and even instrument calibration. Recently some important progress has been made in formulating and evaluating spheroidal EMI solutions [63-64]. Although special approximations resolved evaluation problems at high EMI frequencies, and the exact analytical formulation worked well at low EMI frequencies, stability problems persisted in the mid-frequency range, depending on the geometric and material properties of the spheroid. To remedy this, we construct a combined solution for the induced magnetic field from metallic spheroids that is applicable over the entire EMI band, for both oblate and prolate spheroidal shapes.

Our combined system incorporates asymptotic approximations of the angular and radial spheroidal wave functions [39] (ASWFs and RSFWs) into these existing low- and high-frequency solutions [64] for the induced magnetic field. This extends the frequency range over which the induced magnetic field external to the spheroid may be obtained to cover the problematical mid-frequency range. To be more specific, "low" frequency generally refers to frequencies ranging from static to frequencies below the resonant peak of the phase quadrature response of the induced magnetic field. "High" EMI frequencies are those at which the skin depth of the metallic object is very small relative to its dimensions. As frequency increases further into this "high" frequency range, the EMI response asymptotically approaches the high-frequency limit of vanishing internal magnetic field and the object acts as a perfect (EMI) reflector.

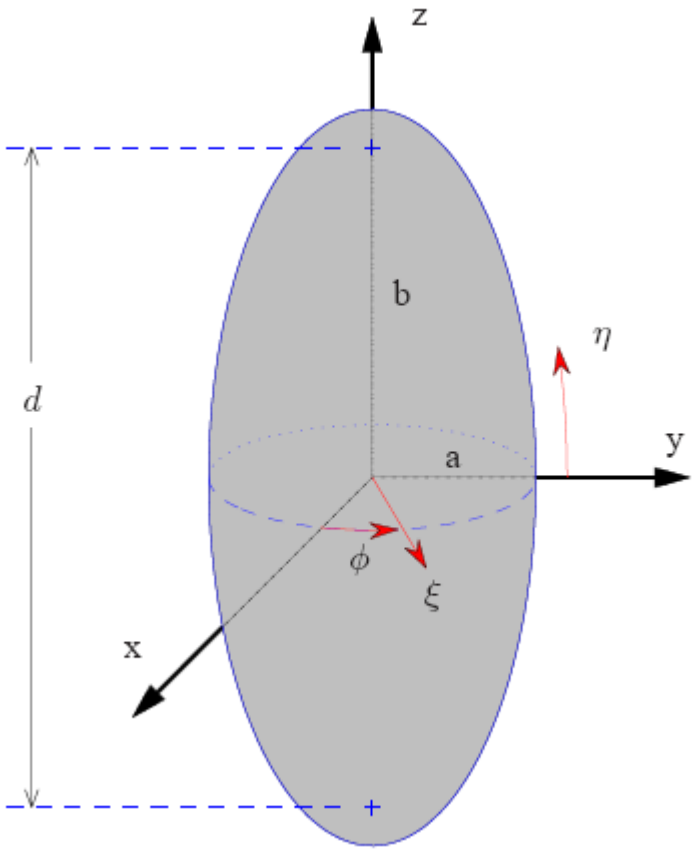

Figure 4-15: Spheroidal geometry.
The coordinates span the following ranges: $1 \le \xi < \infty$ *(Oblate case:* $0 \le \xi < \infty$*),* $-1 \le \eta \le 1$, $0 \le \phi \le 2\pi$, $x = \frac{d}{2}[(1 \mp \eta^2)(\xi^2 \mp 1)]^{\frac{1}{2}} \cos(\phi)$, $y = \frac{d}{2}[(1 \mp \eta^2)(\xi^2 \mp 1)]^{\frac{1}{2}} \sin(\phi)$, $z = \frac{d}{2}\eta\xi$, $e = \frac{b}{a}$, $\xi = \left(\pm(1 - e^{-2})\right)^{-\frac{1}{2}}$, $d = 2\left(\pm(b^2 - a^2)\right)^{\frac{1}{2}}$. *Upper sign* $\rightarrow$ *prolate, lower sign* $\rightarrow$ *oblate.*

Section 4.2.1 contains a brief review of the formulation for the exact solution for the magnetic field within and around a conducting and permeable spheroid (Figure 4-15) under time-harmonic excitation, valid at small size parameters (or frequencies). The predictions of the model in vacuum have been found to agree well with Wait's solution for the sphere and with finite-element/boundary integral (FE-BI) numerical solutions [65] for spheroids. The predictions have also been compared to ultrawideband (UWB) data obtained with the Geophex GEM-3 [66] instrument, for prolate and oblate, permeable (magnetic) and non-permeable machined spheroids. Model and data are found it to be in excellent agreement if the permeability and conductivity of the spheroids are allowed to vary within acceptable physical ranges. Results illustrate that solutions are distinct based on spheroid characteristics and orientation. On this basis, our method could become the forward problem component on which inversion schemes may be based.

Lastly, we investigate two methods in an attempt to adapt this technique to situation where the host medium is conducting, for example when spheroidal targets are located underwater. In the first approach (Section 1), the complex wavenumber in the host medium is used to propagate the primary field from a dipole representation of the GEM-3 [52] to the surface of the spheroid. Subsequently, we use the same exponential factor to account for the effects of the water on the secondary field. This approach

appears to break down at higher frequencies, though we are still investigating its usefulness. The second approach (Section 2) is more exact in that it adopts the use of the full vector wave equation in the surrounding medium instead of using potentials as in the first approach.

4.2.1 Exact formulation

The formulation for the exact analytical solution for the induced magnetic field from a conducting and permeable spheroid under time harmonic excitation in the magnetoquasistatic regime is given in [64] and will only be summarized here.

Let a spheroid with high conductivity σ and relative permeability μ_r (as compared to the background medium) be excited by a time-harmonic primary field $\bar{H}_0(\bar{r})e^{-j\omega t}$ (the time dependence $e^{-j\omega t}$ is suppressed below). We assume the background medium is homogeneous, only weakly magnetic, and poorly conducting so that the wavenumber, k_0, of the host medium may be approximated by $k_0 \approx 0$. As a result of this magnetoquasistatic approximation, the primary magnetic field, $\bar{H}_0(\bar{r})$, and the induced (or secondary) external magnetic field, $\bar{H}_s(\bar{r})$, are irrotational and can be described by scalar potentials, $U_0(\bar{r})$ and $U_s(\bar{r})$, respectively. $U_0(\bar{r})$ and $U_s(\bar{r})$, therefore, both satisfy the Laplace equation in spheroidal coordinates. The known primary field potential can be expanded in terms of solutions of the first kind of the Laplace equation in spheroidal coordinates:

$$U_\circ(\bar{r}) = H_\circ \frac{d}{2} \sum_{m=0}^{\infty} \sum_{n=m}^{\infty} \sum_{p=0}^{1} b_{pmn} P_n^m(\eta) P_n^m(\xi) T_{pm}(\phi), \tag{123}$$

where $P_n^m(\beta)$ represents the associated Legendre function of the first kind of degree n and order m [50]. $T_{pm}(\phi)$ is defined below in (131). Similarly, the secondary field potential can be expanded in terms of Laplace solutions of the second kind as

$$U_s(\bar{r}) = H_\circ \frac{d}{2} \sum_{m=0}^{\infty} \sum_{n=m}^{\infty} \sum_{p=0}^{1} B_{pmn} P_n^m(\eta) Q_n^m(\xi) T_{pm}(\phi), \tag{124}$$

where $Q_n^m(\beta)$ represents the associated Legendre function of the second kind [50] and B_{pmn} are unknown secondary induced field expansion coefficients. The total external magnetic field is the sum of the primary and secondary fields

$$\overline{H}_2 = \overline{H}_\circ + \overline{H}_s = -\nabla U_\circ - \nabla U_s. \tag{125}$$

Within the highly conducting object, the internal magnetic field of the spheroid, $\bar{H}_1(\bar{r})$, can be found by solving the vector wave equation in spheroidal coordinates

$$\nabla \times \nabla \times \overline{H}_1(\bar{r}) - k_1^2 \overline{H}_1(\bar{r}) = 0. \tag{126}$$

Because the displacement current, $\partial \bar{D} / \partial t$, in Faraday's law is neglected, the wavenumber, k_1, is defined by

$$k_1^2 = j\omega\sigma_1\mu_1, \tag{127}$$

and the Helmholtz equation (126) is more appropriately described as the diffusion equation. $\bar{H}_1(\bar{r})$ can be expressed as an infinite series of vector spheroidal wave functions (VSWFs) $\overline{M}$ and $\overline{N}$ as

$$\overline{H}_1 = H_o \sum_{m=0}^{\infty} \sum_{n=m}^{\infty} \sum_{p=0}^{1} \left[A_{pmn}^{(M)} \overline{M}_{pmn}^{r(1)}(c_1;\eta,\xi,\phi) + A_{pmn}^{(N)} \overline{N}_{pmn}^{r(1)}(c_1;\eta,\xi,\phi) \right] \tag{128}$$

$$\begin{aligned} \overline{H}_1 = H_o & \sum_{m=0}^{\infty} \sum_{n=m}^{\infty} \sum_{p=0}^{1} \\ & \left[A_{pmn}^{(M)} \overline{M}_{pmn}^{r(1)}(c_1;\eta,\xi,\phi) + A_{pmn}^{(N)} \overline{N}_{pmn}^{r(1)}(c_1;\eta,\xi,\phi) \right] \end{aligned} \tag{129}$$

where the size parameter, c, of a spheroid is defined as

$$c = k_1 d / 2, \tag{130}$$

and d is the interfocal distance. This size parameter for the spheroid is analogous to the electromagnetic size parameter for the sphere, ka, found in scattering theory.

The functions $\bar{M}_{pmn}^{r(1)}(c_1;\eta,\xi,\phi)$ and $\bar{N}_{pmn}^{r(1)}(c_1;\eta,\xi,\phi)$ are in turn composed of the angular and radial SWFs, $S_{mn}(c,\eta)$ and $R_{mn}(c,\xi)$, as well as the harmonic functions $T_{pm}(\phi)$ defined as

$$T_{pm}(\phi) = \begin{cases} \cos(m\phi) & \text{for} \quad p = 0 \\ \sin(m\phi) & \text{for} \quad p = 1 \end{cases} \tag{131}$$

The exact solution for $\bar{H}_s$ can be obtained by matching the tangential magnetic fields, H_η and H_ϕ, and the normal component of the magnetic flux density, B_ξ, at the surface of the spheroid, i.e.

$$H_{1\eta} = H_{2\eta}, \tag{132}$$

$$\mu_r H_{1\xi} = H_{2\xi}, \tag{133}$$

$$H_{1\phi} = H_{2\phi}. \tag{134}$$

Note that $\mu_r = \mu_{r1} / \mu_{r0}$ refers to the relative permeability of the spheroid with respect to the surrounding medium. Substituting (123)–(130) into (131) results in an infinite set of equations which must be manipulated, truncated, and then cast into matrix form in order to be solved [64].

Even though this solution for the induced magnetic field from a conducting and permeable spheroid is theoretically applicable for any frequency satisfying the magnetoquasistatic assumptions, two problems limit the practical applicability of this solution. The first is that the basis functions used to express the magnetic field internal to the spheroid, in this case the angular (ASWF) and radial (RSWF) spheroidal wave functions, $S_{mn}(c,\eta)$ and $R_{mn}(c,\xi)$ respectively, are in general not orthogonal to each other for different *m*, *n*, and *c* as are the spherical wave functions. Because of this, the complexity of the solution is increased due to the infinite sets of equations that arise when matching the boundary conditions at the spheroidal surface.

The second, more challenging difficulty is that the angular and radial SWFs, which must be evaluated as part of $\bar{M}_{pmn}^{r(1)}(c_1;\eta,\xi,\phi)$ and $\bar{N}_{pmn}^{r(1)}(c_1;\eta,\xi,\phi)$, become unstable and tend to diverge at moderate size parameters (or frequencies) on the order of $|c| \approx 30$ [39, 64]. This numerical difficulty is typically encountered at frequencies lower than those where the resonant peak of the response is fully developed. Some other method is therefore desirable to extend the range of frequencies over which the solutions for the induced magnetic field is tractable. In the next section, we implement asymptotic

expansions of the SWFs in order to extend the exact solution's range of stability to higher frequencies. One difficulty that immediately arises is that the size parameter c for the diffusion equation is complex and asymptotic expansions of the SWFs for the case of complex size parameter have not been treated extensively in the literature (for a summary, see [67]). The analytic model just described was validated against finite-element numerical solutions and experimental data for a spheroid placed in free space [86]. As part of this project we extended the model to incorporate UW environments using the full wave formulation.

4.2.2 Spheroid in a conducting medium

If the spheroid is placed in a conducting medium, the approximation $k_\circ \approx 0$ is no longer valid. In this case, some method must be used to account for the wave and attenuating effects of the conducting medium on the primary and secondary fields. In Section 1, $k_\circ$ is used to propagate the primary field from a dipole representation of the GEM-3 [52] to the surface of the spheroid. Similarly, $k_\circ$ is also used to account for the effects of the water on the secondary field. While this approach appears to break down at higher frequencies, we are still investigating its usefulness. We use the full vector wave equation in the surrounding medium for the second approach (Section 2) instead of using potentials as in the first approach. This approach has the ability to account for high conductivities and permeabilities of the surrounding medium..

4.2.3 Straightforward wavenumber approach

As a first approach to finding the secondary fields from a prolate or oblate spheroid in a conducting medium under time harmonic excitation, we add in the effects of a nonzero wavenumber in the host medium. In the magnetoquasistatic limit, the wavenumber of the surrounding medium is

$$k_\circ^2 = j\omega\sigma_\circ\mu_\circ. \tag{135}$$

The real and imaginary parts of $k_\circ$ are then equal:

$$\Re\{k_\circ\} = \Im\{k_\circ\} = \sqrt{\frac{\omega\sigma_\circ\mu_\circ}{2}}. \tag{136}$$

Because the sources of the GEM-3 model [52] are dipoles, the influence on the primary magnetic field from these dipoles due to this nonzero wavenumber can be included by multiplying the dipolar magnetic field by the exponential $e^{ik_\circ \bar{r}}$. The secondary field can be also be adjusted to incorporate the effects of the nonzero wavenumber of the surrounding medium, but an approximation must be made to maintain the simplicity of the method. If we assume that the secondary fields all originate from the center of the spheroid, then the $\bar{r}$ above can be easily achievable without an integration. To further increase the accuracy of the approximation, the additional terms of the dipole representation can be included

$$\overline{H}_s = \frac{(3+3jk_\circ r - k_\circ^2 r^2)\bar{\bar{r}}\bar{r} - (\bar{\bar{I}} + jk_\circ r - k_\circ^2 r^2)}{4\pi r^3}\cdot \overline{m}, \tag{137}$$

where $\bar{m}$ is the dipole moment obtained from the hybrid method outlined earlier.

This method has been implemented and the results are shown in Figure 4-16 for a prototypical spheroid. At higher frequencies, some undulation and attenuation can be observed in the analytical solution presented above. However, the results are different than those from the numerical solution [57]. The observed discrepancies are due to our approximations and assumptions and could be improved by using the more rigorous and exact approach based on the full vector wave equation.

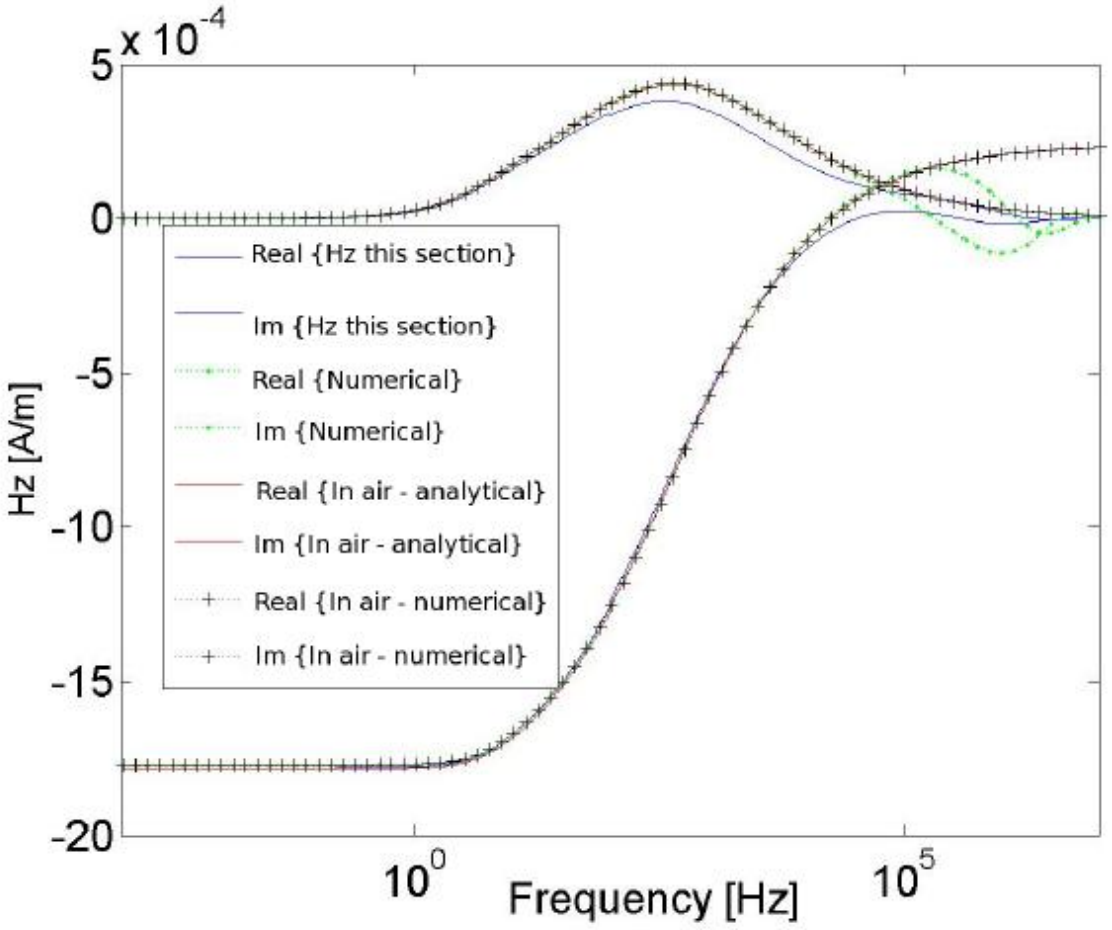

Figure 4-16. Comparison of analytical method outlined above to a numerical calculation of H_z for a prolate spheroid, $2a = 3cm$, $2b = 9cm$, depth=25 cm, under axial excitation from the GEM-3 sensor dipole model. Conductivity of the water is 4 S/m and the frequency is 1 MHz.

5 Conclusions

The Method of Auxiliary Sources was adapted for the case of highly conducting metallic objects placed in a conducting medium resembling seawater. For fast and accurate calculation of EM responses at high frequencies, the MAS was combined with a surface impedance boundary condition (SIBC) appropriate for underwater environments. The combined MAS/SIBC model is originally based on the thin-skin-depth approximation; when conductive embedding media are involved, however, the approximation must be generalized: the boundary conditions must involve tangential components of both electric and magnetic fields. The combined MAS/SIBC algorithm was extended to conducting and permeable multi-layer metallic objects placed in a conducting medium with properties similar to those of seawater. The accuracy of the technique was tested against actual EMI data for a conducting sphere that was placed in salt water and excited by the GEM-3D sensor. The combined code was also tested against analytic solutions. The comparisons show excellent agreement with both analytic and experimental data.

To fully understand the underlying physics of EMI scattering phenomena in realistic aqueous environments we adapted the Debye dielectric relaxation model and built it into our MAS/SIBC numerical code. Debye's theory models the electromagnetic properties of a briny medium as functions of frequency, temperature and salinity; it provides realistic estimates of the properties and of the way they change at different oceanic locations and depths.

The Method of Auxiliary Sources was used to study the effects of water surface roughness on the propagation of low-frequency electromagnetic waves through marine environments. The rough surface was generated as a superposition of a variable number of oscillating surface waves with different amplitudes, wavelengths, propagation directions, and phases. The three-dimensional scattering problem was then solved to determine the distribution of magnetic fields above and below the water level. Although the perturbation in magnetic fields depends on the shape of the air-water interface, it is low compared to the strength of the signals, and decays with the distance from the interface.

Numerical experiments were conducted for homogeneous as well as heterogeneous UXO-like objects subject to frequency- or time-domain illumination. The near and far EMI fields and induced eddy-current distributions were calculated to illustrate the physics of EMI scattering phenomena from highly conducting and permeable metallic objects placed in UW environments. In particular, we analyzed the coupling effects between an object and its surrounding conductive medium, especially at high frequencies (or early times for time-domain sensors). We conducted simulations of spheres (for code validation), of spheroidal, cylindrical, and hollow targets, and of a 105-mm HEAT-round UXO. In addition we studied ultra-wideband EMI field scattering from multi layered targets and rough surfaces. At all points we used realistic models of the current, state-of-the-art sensors that will be expected to perform actual littoral UXO remediation.

We found that marine environments have negligible effects on the performance of advanced EMI sensors, which operate between 40 Hz and 10 kHz (or, in the TD, from 100 μs to 25 ms). We also found that at high frequencies (>10 kHz) or very early times (<100 μs) there are strong interactions between an object and the medium surrounding it. These coupling effects depend on the distance between the object and the sensor and on the geometry and electromagnetic properties of the object. These new distinct features, which provide new perspectives for UW target classification using both electric and magnetic fields, are the main subjects of investigation of SERDP Project MR-1714.

The numerical results were cross-validated using analytical models for conducting and permeable spherical and spheroidal objects. Under this project we developed closed-form solutions for UW EMI problems involving spheres and spheroids and implemented them numerically. We wrote programs that treat EMI scattering by a sphere, under both uniform and dipolar excitation. The exciting dipole can be anywhere and at any orientation. We found that "geometric" (e^{jkR}) effects dominate over "dynamic" ones.

This is more noticeable with dipolar excitation, since the geometric phenomenon occurs both ways, and both the excitation and the response attenuate as a function of frequency as they propagate. These effects appear at high frequencies, however—the measurable EMI response in the time window accessible to currently available sensors remains essentially unchanged. That is also the case when a two-layer system is considered—a sphere wrapped in a vacuum sheath and embedded in a conducting medium.

Similar effects have been observed for other advanced forward EMI models, such as the GSEA, the ONVMS, and the JD-based data preprocessing scheme. This means that next-generation EMI sensors and advanced signal processing approaches developed to tackle the land-based UXO problem could be used to detect and discriminate highly conducting and permeable metallic objects embedded underwater.

6 Publications

1. F. Shubitidze, B. Barrowes, I. Shamatava, J. P. Fernández, and K. O'Neill, "Underwater UXO discrimination studies: adapting EMI forward models to marine environments," *Proceedings of SPIE* **7303**, 7303-13 (2009).

2. F. Shubitidze, B. Barrowes, I. Shamatava, J. P. Fernández, and K. O'Neill, "Near and far EMI-field analyses in a conducting environment to enhance underwater UXO detection," *Proceedings of SPIE* **7303**, 7303-12 (2009).

3. F. Shubitidze, G. Schultz, I. Shamatava, " Method of auxiliary sources for marine EMI scattering problems", MARELEC, 2009, 7-9 July 2009 Stockholm, Sweden.

4. A. Bijamov, F. Shubitidze, J. P. Fernández, I. Shamatava, B. E. Barrowes, K. A. O'Neill, "Assessing EMI noise due to the marine environment to enhance underwater UXO detection and discrimination", *Proceedings of SPIE* **7664**, 7664-11 (2010).

5. F. Shubitidze, J. P. Fernández, I. Shamatava, "3D Numerical Modeling of Underwater Electromagnetic Induction Phenomena: Assessing EMI Noise Due to the Marine Environment", Partners in Environmental Technology Technical Symposium and Workshop, December 1-3, 2009

6. F. Shubitidze, B. Barrowes, I. Shamatava, K. O'Neill, "Assessing EMI Sensors' Detection and Discrimination performances in underwater environments ", UXO/Countermine/Range Forum 2009, Orlando Florida, August 24-27, 2009.

7. J. P. Fernández, B. E. Barrowes, A. Bijamov, T. M. Grzegorczyk, K. A., O'Neill, I. Shamatava, and F. Shubitidze, "Low-frequency response of a sphere embedded in water" in Applied Computational Electromagnetics Symposium, ACES-2011 (Williamsburg, VA, March 27-31), 2011.

8. F. Shubitidze, B. E. Barrowes, J. P. Fernández, I. Shamatava, and K. A. O'Neill, "The method of auxiliary sources for solving low-frequency electromagnetic induction problems in underwater environments" in Applied Computational Electromagnetics Symposium, ACES-2011 (Williamsburg, VA, March 27-31), 2011.

7 References

1. E. Gasperikova, J.T. Smith, H.F. Morrison, and A. Becker, "Berkeley UXO Discriminator (BUD)," 2007.

2. I. J. Won, D. A. Keiswetter, and T. H. Bell, "Electromagnetic induction spectroscopy for clearing landmines," *IEEE Transactions on Geoscience and Remote Sensing,* vol. 39, pp. 703-709, Apr 2001.

3. JD McNeill and M. Bosnar, "Application of time domain electromagnetic techniques to UXO detection," 1996, pp. 34-42.

4. D. M. Cargile, D. M. Bennett, H. H. Goodson, R. A. DeMoss, and E. R. Cespedes, "Advanced UXO detection / discrimination technology demonstration," Kahoolawe, HI2004.

5. Benjamin Barrowes, "Handheld Frequency Domain Vector EMI Sensing for UXO Discrimination," 2006.

6. Leonard R. Pasion and Douglas W. Oldenburg, "A Discrimination Algorithm for UXO Using Time Domain Electromagnetics," *Journal of Environmental and Engineering Geophysics*, vol. 6, pp. 91-102, 2001.

7. S. V. Chilaka, D. L. Faircloth, L. S. Riggs, and H. H. Nelson, "Enhanced discrimination among UXO-like targets using extremely low-frequency magnetic fields," *IEEE Transactions on Geoscience and Remote Sensing,* vol. 44, pp. 10-21, Jan 2006.

8. S. Billings, "Practical Discrimination Strategies for Application to Live Sites," presented at the SERDP and ESTCP Partners in Environmental Technology Technical Symposium & Workshop, Washington, DC, 2006.

9. P. Gao, L. Collins, P. M. Garber, N. Geng, and L. Carin, "Classification of landmine-like metal targets using wideband electromagnetic induction," *IEEE Transactions on Geoscience and Remote Sensing,* vol. 38, pp. 1352-1361, May 2000.

10. N. Geng, C. E. Baum, and L. Carin, "On the low-frequency natural response of conducting and permeable targets," *IEEE Transactions on Geoscience and Remote Sensing,* vol. 37, pp. 347-359, Jan 1999.

11. Y. Zhang, L. Collins, H. Yu, C.E. Baum, and L. Carin, "Sensing of unexploded ordnance with magnetometer and induction data: Theory and signal processing," *Geoscience and Remote Sensing, IEEE Transactions on,* vol. 41, pp. 1005-1015, 2003.

12. T.H. Bell, B.J. Barrow, and J.T. Miller, "Subsurface discrimination using electromagnetic induction sensors," *Geoscience and Remote Sensing, IEEE Transactions on,* vol. 39, pp. 1286-1293, 2001.

13. J.T. Miller, T.H. Bell, J. Soukup, and D. Keiswetter, "Simple phenomenological models for wideband frequency-domain electromagnetic induction," *Geoscience and Remote Sensing, IEEE Transactions on,* vol. 39, pp. 1294-1298, 2001.

14. L. Carin, H. T. Yu, Y. Dalichaouch, A. R. Perry, P. V. Czipott, and C. E. Baum, "On the wideband EMI response of a rotationally symmetric permeable and conducting target," *IEEE Transactions on Geoscience and Remote Sensing*, vol. 39, pp. 1206-1213, Jun 2001.

15. F. Shubitidze, K. O'Neill, BE Barrowes, I. Shamatava, JP Fernandez, K. Sun, and KD Paulsen, "Application of the normalized surface magnetic charge model to UXO discrimination in cases with overlapping signals," *Journal of Applied Geophysics*, vol. 61, pp. 292-303, 2007.

16. X. D. Chen, K. O'Neill, B. E. Barrowes, T. M. Grzegorczyk, and J. A. Kong, "Application of a spheroidal-mode approach and a differential evolution algorithm for inversion of magneto-quasistatic data in UXO discrimination," *Inverse Problems*, vol. 20, pp. S27-S40, Dec 2004.

17. F. Shubitidze, K. O'Neill, I. Shamatava, K. Sun, and K.D. Paulsen, "Analysis of EMI scattering to support UXO discrimination: heterogeneous and multiple objects," 2003, p. 928.

18. Fridon Shubitidze, Eugene Demidenko, Benjamin E. Barrowes, Irma Shamatava, Juan P. Fernández, and Kevin O'Neill, "Combining dipole and mixed model approaches for UXO discrimination," in *SPIE*, 2008.

19. F. Shubitidze, BE Barrowes, I. Shamatava, JP Fernández, and K. O'Neill, "Data-derived generalized SEA applied to MPV TD data."

20. F. Shubitidze, K. O'Neill, I. Shamatava, K. Sun, and K.D. Paulsen, "Fast and accurate calculation of physically complete EMI response by a heterogeneous metallic object," *Geoscience and Remote Sensing, IEEE Transactions on*, vol. 43, pp. 1736-1750, 2005.

21. K. Sun, K. O'Neill, F. Shubitidze, I. Shamatava, and K.D. Paulsen, "Fast data-derived fundamental spheroidal excitation models with application to UXO discrimination," *Geoscience and Remote Sensing, IEEE Transactions on*, vol. 43, pp. 2573-2583, 2005.

22. Steven Arcone, "Ground-Penetrating Radar Survey of Sub-bottom Munitions in a small New England Lake," in *Partners in Environmental Technology Technical Symposium and Workshop*, Washington, DC, 2006.

23. J. R. McDonald, "UXO Detection and Characterization in the Marine Environment," in *Partners in Environmental Technology Technical Symposium & Workshop*, Washington, DC, 2006.

24. S. J. Norton, W. A. SanFilipo, and I. J. Won, "Eddy-current and current-channeling response to spheroidal anomalies," *IEEE Transactions on Geoscience and Remote Sensing*, vol. 43, pp. 2200-2209, Oct 2005.

25. J. L. Stalnaker, M. E. Everett, A. Benavides, and C. J. Pierce, "Mutual induction and the effect of host conductivity on the EM induction response of buried plate targets using 3-D finite-element analysis," *IEEE Transactions on Geoscience and Remote Sensing*, vol. 44, pp. 251-259, Feb 2006.

26. F. Shubitidze, K. O'Neill, S. A. Haider, K. Sun, and K. D. Paulsen, "Application of the method of auxiliary sources to the wide-band electromagnetic induction problem," *IEEE Transactions on Geoscience and Remote Sensing*, vol. 40, pp. 928-942, Apr 2002.

27. K. L. Sun, K. O'Neill, F. Shubitidze, I. Shamatava, and K. D. Paulsen, "Theoretical analysis and range of validity of TSA formulation for application to UXO discrimination," *IEEE Transactions on Geoscience and Remote Sensing*, vol. 42, pp. 1871-1881, Sep 2004.

28. I. Shamatava, F. Shubitidze, K. O. O'Neill, K. Sun, and K.D. Paulsen, "An Efficent User-Friendly Program for Computing Electromagnetic Induction (EMI) Responses from Heterogeneous Objects Subject to State-of-the-Art Sensors," in *UXO/COuntermine Forum*, St. Louis, MI, 2004.

29. F. Shubitidze, K. O'Neill, K. Sun, I. Shamatava, and K. D. Paulsen, "A hybrid full MAS and combined MAS/TSA algorithm for electromagnetic induction sensing," *Applied Computational Electromagnetics Society Journal*, vol. 19, pp. 112-126, Mar 2004.

30. Andrease.Mg, "Correction to Scattering from Bodies of Revolution," *IEEE Transactions on Antennas and Propagation*, vol. Ap14, pp. 659-&, 1966.

31. J. R. Mautz and R. F. Harrington, "Electromagnetic Scattering from a Homogeneous Material Body of Revolution," *Aeu-International Journal of Electronics and Communications*, vol. 33, pp. 71-80, 1979.

32. J. R. Mautz and Harringt.Rf, "Radiation and Scattering from Bodies of Revolution," *Applied Scientific Research*, vol. 20, pp. 405-&, 1969.

33. T. K. Wu and L. L. Tsai, "Scattering from Arbitrarily-Shaped Lossy Dielectric Bodies of Revolution," *Radio Science*, vol. 12, pp. 709-718, 1977.

34. Andrease.Mg, "Scattering from Bodies of Revolution," *IEEE Transactions on Antennas and Propagation*, vol. Ap13, pp. 303-&, 1965.

35. D. Kakulia, G. Ghvedashvili, and F. Shubitidze, "Extending MAS/TSA Technique for Conducting Environments to Enhance Underwater UXO Discrimination," presented at the PIERS, Cambridge, MA, 2008.

36. Julius Adams Stratton, *Electromagnetic theory*, 1st ed. New York, London,: McGraw-Hill book company, inc., 1941.

37. L. A. Klein and C. T. Swift, "Improved Model for Dielectric-Constant of Sea-Water at Microwave-Frequencies," *IEEE Transactions on Antennas and Propagation*, vol. 25, pp. 104-111, 1977.

38. W. Ellison, A. Balana, G. Delbos, K. Lamkaouchi, L. Eymard, C. Guillou, and C. Prigent, "New permittivity measurements of seawater," *Radio Science*, vol. 33, pp. 639-648, May-Jun 1998.

39. Carson Flammer, *Spheroidal wave functions*. Stanford, Calif.,: Stanford University Press, 1957.

40. J. J. Thomson and James Clerk Maxwell, *Notes on recent researches in electricity and magnetism, intended as a sequel to Professor Clerk-Maxwell's Treatise on electricity and magnetism*. Oxford,: The Clarendon press, 1893.

41. A. E. H. Love, "The Scattering of Electric Waves by a Dielectric Sphere," in *Proc. London Math Soc*, 1899, pp. 308-321.

42. G. Mie, "Beitraege zur Optik trueber Medien, speziell kolloidaler Metalloesungen," *Ann. Physik*, vol. 330, pp. 377-445, 1908.

43. P. Debye, "Der Lichtdruck auf Kugeln von beliebigem Material," *Ann. Physik,* vol. 335, pp. 57-136, 1909.

44. S. H. Ward and G. W. Hohmann, "Electromagnetic Theory for Geophysical Applications," in *Investigations in Geophysics* vol. 3, Nabighian. M. N., Ed., ed Society of Exploration Geophysicists, Tulsa, OK, 1997.

45. J. R. Wait, "A conducting sphere in a time varying magnetic field," *Geophysics,* vol. 16, pp. 666-672, 1951.

46. H. W. March, "The field of a magnetic dipole in the presence of a conducting sphere," *Geophysics,* vol. 18, pp. 671-684, 1953.

47. M. N. Nabighian, "Quasi-static transient response of a conducting permeable sphere in a dipolar field," *Geophysics,* vol. 35, pp. 303-309, 1970.

48. S. K. Singh, "Electromagnetic transient responce of a conducting sphere embedded in a conductive medium," *Geophysics,* vol. 38, pp. 864-893, 1973.

49. F. S. Grant and Gordon Fox West, *Interpretation theory in applied geophysics*. New York,: McGraw-Hill, 1965.

50. Milton Abramowitz and Irene A. Stegun, *Handbook of mathematical functions with formulas, graphs, and mathematical tables*. Washington,: U.S. Govt. Print. Off., 1964.

51. J. R. Wait, "On the electromagnetic responce of a conducting sphere to a dipole field," *Geohpysics,* vol. 25, pp. 649-658, 1960.

52. K. Sun, K. O'Neill, I. Shamatava, and F. Shubitidze, "Application of prolate spheroid solutions in simulation of EMI scattering with realistic sensors and objects," in *ACES*, 2003, pp. 531-537.

53. Geophex. Ltd (Bill San Filipo and I. J. Won), "Broadband Electromagnetic Detection and Discrimination of Underwater UXO," 2005.

54. D. E. Amos, "Algorithm 644: A portable package for Bessel functions of a complex argument and nonnegative order," *ACM Trans. Math. Softw.*, vol. 12(3), pp. 265-273, 1986.

55. F. Shubitidze, J. P. Fernández, B. E. Barrowes, I. Shamatava, and K. O. O'Neill, "The Method of Auxiliary Sources for Solving Low-Frequency Electromagnetic Induction Problems in Underwater Environments," in *Applied Computational Electromagnetics Symposium*, Williamsburg, VA, 2011.

56. F. Shubitidze, B. E. Barrowes, I. Shamatava, J. P. Fernández, and K. O. O'Neill, "Near and far EMI-field analysis in a conducting environment to enhance underwater UXO detection," in *Proceedings of SPIE*, Bellingham, WA, 2009, 2009.

57. F. Shubitidze, B. Barrowes, I. Shamatava, J. P. Fernandez, and K. O. O'Neill, "Underwater UXO discrimination studies: adapting EMI forward models to marine environments," in *SPIE*, Orlando, FL, 2009.

58. B. Johnson, "A research and development strategy for unexploded ordnance sensing," DTIC Document1996.

59. P Wiseman. (2003, December 12, 2003) 30-year-old bombs still very deadly in Laos. *USA Today*. 10A.

60. D. Keiswetter, B. SanFilipo, I. J. Won, J.T. Miller, T. H. Bell, E. R. Cespedes, and K. O'Neill, "Discriminating Capabilities of Multifrequency EMI data," in *SPIE*, 2000, pp. 130-40.

61. K. Sun, K. O'Neill, F. Shubitidze, S. A. Haider, and K. D. Paulsen, "Simulation of electromagnetic induction scattering from targets with negligible to moderate, penetration by primary fields," *IEEE Transactions on Geoscience and Remote Sensing*, vol. 40, pp. 910-927, Apr 2002.

62. J. R. Wait, "A Conducting Permeable Sphere in the Presence of a Coil Carrying an Oscillating Current," *Canadian Journal of Physics*, vol. 31, pp. 670-678, 1953.

63. H. Braunisch, C.O. Ao, K. O'Neill, and J.A. Kong, "Magnetoquasistatic response of conducting and permeable prolate spheroid under axial excitation," *Geoscience and Remote Sensing, IEEE Transactions on*, vol. 39, pp. 2689-2701, 2001.

64. C.O. Ao, H. Braunisch, K. O'Neill, and J.A. Kong, "Quasi-magnetostatic solution for a conducting and permeable spheroid with arbitrary excitation," *Geoscience and Remote Sensing, IEEE Transactions on*, vol. 40, pp. 887-897, 2002.

65. C. D. Moss, T. M. Grzegorczyk, K. O'Neill, and J. A. Kong, "A hybrid time-domain model of electromagnetic induction from conducting, permeable targets," *IEEE Transactions on Geoscience and Remote Sensing*, vol. 44, pp. 2916-2926, Oct 2006.

66. I. J. Won, D. Keiswetter, D. Hansen, E. Novikova, and T. M. Hall, "GEM-3: A Monostatic Broadband Electromagnetic Induction Sensor," *Journal of Environmental Engineering and Geophysics*, vol. 2, pp. 53-64, 1997.

67. B. E. Barrowes, K. O. O'Neill, T. M. Grzegorczyk, and J. A. Kong, "Asymptotic expansions of the prolate angular spheroidal wave function for complex size parameter," *Studies in Applied Mathematics*, vol. 113, pp. 271-301, 2004.